TECHNISCHE UNIVERSITÄT MÜNCHEN

FAKULTÄT FÜR CHEMIE

Nanoscale NMR spectroscopy of surfaces and interfaces using quantum sensors in diamond

Kristina S. Liu

Vollständiger Abdruck der von der Fakultät für Chemie der Technischen Universität München zur Erlangung des akademischen Grades einer

Doktorin der Naturwissenschaften (Dr. rer. nat.)

genehmigten Dissertation.

Vorsitz: Priv. Doz. Dr. Aras Kartouzian

Prüfer der Dissertation:

TUM Junior Fellow Dr. Dominik B. Bucher

Prof. Dr. Ian D. Sharp

Die Dissertation wurde am 02.09.2022 bei der Technischen Universität München eingereicht und durch die Fakultät für Chemie am 13.09.2022 angenommen

Acknowledgments

I am grateful for the clarity of vision and emphasis of academic integrity my supervisor Dominik Bucher had for my research projects. With heroic patience, he continually encouraged me to grow my knowledge. As busy as he was, he always had time for me to help troubleshoot even the smallest issues.

I am thankful to my collaborators Alex Henning and Johannes Bartl for teaching me how to operate devices they have been fittingly deemed "superusers" at and inspiring me to be more detail oriented. I am thankful for Xiaoxin Ma, Anna Lisa Semrau, Stefanie Pritzl, Theobald Lohmüller and Ian Sharp for partnering with me in the different projects. Their expertise and dedication to the projects have been the keys to their success. Special thanks to Ian for editing my writing!

I am thankful to lab mates Fleming Bruckmaier, Markus Heindl, Robin Allert, Fabian Freire-Moschovitis, Joachim Leibold, Karl Briegel, Julia Draeger and Nick Neuling for making the work day enjoyable and pleasant with conversation and encouragement as well as giving me practical assistance in innumerable ways. They inspire me with their humor and distinctive ways they see the world.

I owe many months of salary to Roberto Rizzato for finding too many diamond chips that have been victims of my clumsiness.

I am grateful to my partner Moxi Liang for his love and presence through the joys and the frustrations of this journey.

And finally, my parents Zimin Liu whose work ethic deeply influenced me and Mary Liu whose curiosity about the world gave me the courage to move to a foreign country to continue to explore and learn.

1. Abstract

Numerous processes ranging from solar energy to transport of drugs and molecules occur at surfaces and interfaces. Current technology to study them are often lacking in spatial resolution or require ultra-high vacuum (UHV). UHV is problematic for liquids and powders, and hinder the understanding of these processes under ambient conditions at which they function. These limitations do not constrain nanoscale nuclear magnetic resonance (NMR) spectroscopy using quantum sensors such as nitrogen vacancy (NV) centers in diamond. On the nanoscale, these sensors are brought in close contact to nuclear spins, allowing for high sensitivity detection of samples from a few zeptoliters to single molecules or even single nuclear spins on the surface of the diamond. The motivation for using quantum sensing for performing nanoscale NMR spectroscopy of surfaces and interfaces is described in chapter 3. In chapters 4 and 5, we integrate the diamond surface with aluminum oxide (Al_2O_3). To illustrate the capabilities of the NV quantum sensors, in chapter 4 the Al_2O_3 is functionalized by phosphonate chemistry to form self-assembled monolayers. The NV quantum sensors detect NMR signals from the monolayer with high spatial resolution and femtomole sensitivity. They can quantify the molecular coverage of the molecules and indicates their binding to the Al_2O_3 surface. In particular, NV-NMR can monitor in real-time the formation kinetics at the solid-liquid interface. These results show that in-situ NMR analysis using NV quantum sensors are applicable to surface science, from catalysis to biology.

However, currently this technology is limited to such "tethered" molecules, and solid or highly viscous samples. Molecular diffusion of liquid-state molecules in and out of nanoscale detection volumes occur extremely quickly. Therefore, a large portion of surface science,

remains challenging for nanoscale NMR. In chapter 5, we use surface-anchored metal-organic frameworks with angstrom-sized pores grown on the Al_2O_3 adhesion layer to trap liquid-state molecules near the NV-centers. This enables the detection of NMR signals from a liquid sample, and therefore these results are an important step towards nanoscale liquid-phase NMR with high spectral resolution.

NV-centers are suitable for label-free direct probing diffusion under ambient conditions, which is an essential process to understand within biological surface systems such as cell membranes. NV-NMR can detect nuclei unique to biological samples such as ^{31}P and can provide nanoscale localization. In chapter 6, supported phospholipid bilayers of the phospholipid dipalmitoylphosphatidylcholine are used as a membrane model and nanoscale NMR spectroscopy of ^{31}P nuclei in the gel phase and the fluid phase is performed. We observe a clear diffusional broadening of the ^{31}P signal from the gel phase to the fluid phase, indicating faster molecular diffusion.

2. Zusammenfassung

Zahlreiche Prozesse, von der Solarenergie bis zum Stofftransport von Medikamenten und Molekülen, finden an Oberflächen und Grenzflächen statt. Die derzeitige Technologie zur Untersuchung dieser Vorgänge weist häufig eine unzureichende räumliche Auflösung auf oder erfordert ein Ultrahochvakuum (UHV). UHV ist für Flüssigkeiten und Pulver problematisch und behindert das Verständnis dieser Prozesse unter Umgebungsbedingungen, bei denen sie ablaufen. Diese Einschränkungen gelten nicht für die magnetische Kernresonanzspektroskopie (*Nuclear Magnetic Resonance Spectroscopy*, oder NMR) im Nanomaßstab unter Verwendung von Quantensensoren wie Stickstoff-Fehlstellen-Zentren (*Nitrogen Vacancy*, oder NV) in Diamanten. Diese Sensoren werden in engen Kontakt (Nanometer) mit den Kernspins gebracht, was eine hochempfindliche Detektion von Proben mit Volumina von einigen Zeprolitern bis hin zu einzelnen Molekülen oder sogar einzelnen Kernspins auf der Oberfläche des Diamanten ermöglicht. Die Motivation für die nanoskalige NMR-Spektroskopie von grenz- und oberflächen mit quantensensoren in diamant wird in Kapitel 3 beschrieben. In Kapitel 4 und 5 integrieren wir die Diamantoberfläche mit Aluminiumoxid (Al_2O_3). Zur Demonstration der Fähigkeiten der NV-Quantensensoren wird Al_2O_3 in Kapitel 4 durch Phosphonatchemie funktionalisiert, um selbsorganisierende Einzelschichten zu bilden. Die NV-Quantensensoren detektieren NMR-Signale von der Einzelschicht mit hoher räumlicher Auflösung und Femtomol-Sensitivität. NV-NMR kann die molekulare Bedeckung der Al_2O_3-Oberfläche quantifizieren und zeigt die Formation der Einzelschicht an. Insbesondere kann NV-NMR die Formationskinetik an der Fest-Flüssig-Grenzfläche in Echtzeit auflösen. Diese Ergebnisse zeigen, dass die *In-situ*-NMR-Analyse mit NV-Quantensensoren in der Ober-

flächenforschung von der Katalyse bis zur Biologie eingesetzt werden kann.
Derzeit ist diese Technologie jedoch auf solche chemisch gebundenden Moleküle und feste oder hochviskose Proben beschränkt. Molekulare Diffusion von Molekülen im flüssigen Zustand in und aus nanoskaligen Nachweisvolumina erfolgt extrem schnell. Daher bleibt ein großer Teil der Oberflächenforschung eine Herausforderung für die NMR im Nanomaßstab. In Kapitel 5 verwenden wir oberflächenverankerte metallorganische Gerüste (engl. *metal-organic frameworks*) mit angströmgroßen Poren, die auf der Al_2O_3-Adhäsionsschicht gewachsen wurden, um flüssigphasige Moleküle in der Nähe der NV-Zentren verankern. Dies ermöglicht den Nachweis von NMR-Signalen aus einer flüssigen Probe, daher sind diese Ergebnisse ein wichtiger Schritt hin zur Flüssigphasen-NMR im Nanomaßstab mit hoher spektraler Auflösung.
Diffusion ist ein essenzieller Prozess, den man in biologischen Oberflächensystemen wie zum Beispiel in Zellmembranen analysieren muss. NV-Zentren eignen sich für die markierungsfreie direkte Untersuchung der Diffusion unter Umgebungsbedingungen, was ein wesentlicher Prozess zum Verständnis biologischer Oberflächensysteme wie Zellmembranen ist. NV-NMR kann Kerne nachweisen, die charakteristisch für biologische Proben sind, wie zum Beispiel ^{31}P, und kann dren Lokalisierung im Nanobereich ermöglichen. In Kapitel 6 werden unterstützte Phospholipiddoppelschichten (engl. *supported lipid bilayers*) des Phospholipids Dipalmitoylphosphatidylcholin als Membranmodell verwendet und NMR-Spektroskopie im Nanobereich von ^{31}P-Kernen in der Gelphase um in der flüssigen Phase anzuwenden. Wir beobachten eine deutliche diffusionsbedingte Linienverbreiterung des ^{31}P-Signals von der Gelphase zur flüssigen Phase, was mit schnellerer Moleküldiffusion begründet werden kann.

Contents

3. Motivation and application of quantum sensing to surface science

This work is an exploration of nanoscale nuclear magnetic resonance (NMR) spectroscopy using a defect in diamond known as the nitrogen vacancy center (NV-center). The underlying motivation for this work is to demonstrate the impact NV-centers can have as quantum sensors for magnetic resonance technology in understanding processes at surfaces and interfaces. NMR spectroscopy is a powerful chemical characterization tool widely used in disciplines ranging from materials to biomedical sciences [1]. It would be an ideal tool to use to study processes at surfaces and interfaces. However, it is limited by low sensitivity, typically requiring a substantial amount of material for analysis [2–4]. One promising way to overcome this limitation is the reduction of the sensor size down to the nanoscale [5]. NV-centers as quantum sensors near the diamond surface have demonstrated the detection of NMR signals from a few zeptoliters of material, to single molecules or even nuclear spins under ambient conditions [6, 7]. This chapter will provide a description of the quantum sensor, its application to surface science in this work, as well as the current challenges of the technology.

3.1. Surface Science

In the 1960s to the 1980s, modern surface science emerged and matured as ultra high vacuum (UHV) systems enabled the development of analytical tools such as X-ray photoelectron spectroscopy (XPS), secondary ion mass spectrometry (SIMS) and others. By allowing better understanding of chemical processes at surfaces/interfaces, these techniques supported

progress in solid state and eletronic materials ranging from lithium ion batteries to electro- and photocatalysis.[8, 9]

However, a major challenge within surface science is studying surfaces under realistic conditions of pressure and temperature close to those in human environments and in industrial catalytic processes. In catalysis, it is known as the "pressure gap" [9, 10]. Surface science also extends to understanding biological systems such as cell membranes. For these applications, UHV impedes both *in vitro* and *in vivo* studies in aqueous environments. These studies would be important for understanding the particulars of protein interactions with lipid surfaces and lipid lipid interactions as well as the roles of water and ions in relation to their structure and dynamics in these interactions. This would be critical for the development of many applications, such as nanodrug encapsulations or stem cell and tissue engineering.[8] Therefore, investigative tools working at near ambient conditions are still under development [10].

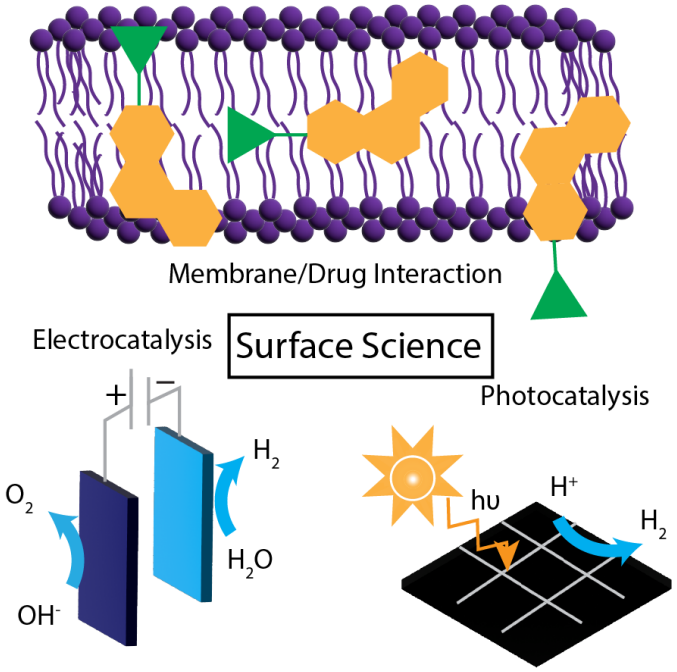

Figure 3.1.: Representative topics of investigation in surface science

3.2. Nuclear magnetic resonance spectroscopy: sensitivity problem, quantum sensing solution

NMR spectroscopy is an investigative tool that has been widely adopted for its ability to quantitatively give molecular information on the structure, dynamics and chemical identity. All atoms have nuclei consisting of elementary protons and neutrons. When a nuclei has

an uneven number of protons, it has a property called spin which makes it NMR active. When placed within a magnetic field, these NMR active nuclei with spin begin to precess and different nuclei within a molecule resonate at different frequencies (known as Larmor frequency) f = γB_0, where the frequency of precession is dependent on the gyromagnetic ratio of the NMR active nuclei γ and the strength of the magnetic field B_0 (Fig. 3.2 b). Not only can the chemical composition of a material be determined by its precession frequency, the frequency is also altered by the environment of the nuclei which is the so-called chemical shift. The number of chemical shifts and their values allows for a detailed analysis of the structure of a molecule. NMR relies on expensive superconducting magnets to generate a "magnetic" energy in competition with the thermal energy (Fig. 3.2 a). This energy difference results in a population difference between the energy levels which can be inductively probed. For a two-level system, this population difference or polarization of molecules is dependent on the Boltzmann distribution (where k_B is the Boltzmann constant and T is temperature), where p = $\exp(-E_{mag}/k_BT)$. For a ^{1}H nuclear spin at 1.5 T, that magnetic energy E_{mag} is 2.6 x 10^{-7} eV, which in comparison to thermal energy of k_BT at room temperature (T = 300 K) $\sim$ 2.6 x 10^{-2} eV comes to a difference of only $\approx 10^{-5}$. This is known as the sensitivity problem in NMR, which has motivated the development of hyperpolarization technology such as the Overhauser effect even back in the 1950s [11]. The information that could be gained by NMR is then limited to samples with a sufficient number of spins, and a number of studies such as of surfaces, thin films, and low-γ nuclei have been precluded [3]. Bringing NMR down to the nanoscale greatly increases its sensitivity as we will see later in chapter 4. Quantum technology has revolutionized industries, from sensing to information. Diamond is a particularly attractive material for quantum technologies due to its physical properties and atomic scale color centers in the solid state that hold promise as quantum controllable sensors with high sensitivity and spatial resolution. One area of application of these sensors is in the detection of magnetic fields from the precession of nuclei.[12] Therefore in this work, we apply quantum sensors in diamond to perform NMR spectroscopy at the nanoscale with high sensitivity and spatial resolution.

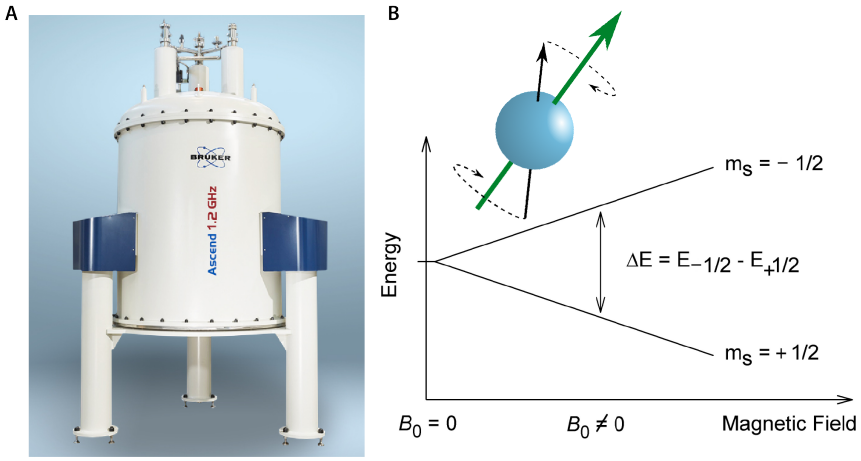

Figure 3.2.: a) Bruker Ascend NMR magnet at 1.2 GHz proton frequency (21 T). Superconducting magnets of stronger magnetic field are being developed (and at greater expense) due to the inherent lack of sensitivity of NMR. b) Energy splitting of a two-level spin-1/2 system increases with magnetic strength. Inset: nuclear spin precessing (at the nuclei and field specific Larmor frequency).

3.3. Quantum sensing of surfaces and its challenges

3.3.1. The quantum sensor

The diamond is a host to various defect and color centers. The one with the most promising properties is the NV-center. A thorough review of the NV-center has been written by Doherty et al. [13]. This dissertation will only provide information most important for context of experimentation and results. The NV-center can either exist in a neutral charge state or negatively charged (which will be subsequently referred to as NV-center). The negatively charged NV-center is a system of trapped electrons in the diamond lattice. It exists in a tetrahedral symmetry with 4 different orientations (Fig. 3.3 A). At room temperature, the NV-center is capable of being optically polarized in one spin-state, and the spin-state can also be optically read out. The NV-center also has uniquely long relaxation properties (on the order of milliseconds) at room temperature. These optical and relaxation properties support a wide range of applications from quantum information and quantum sensing, to fluorescence microscopy [5, 13, 14]. The NV-center has a zero-phonon line (ZPL) of 637 nm. Above the

ZPL, the NV-center has photoluminescence (PL) with red wavelengths in the phonon side band. Excitation of the NV-center is typically done off resonance using 532 nm green laser that is affordable and widely available (Fig. 3.3 B). The NV-center is a spin-1 system with a triplet ground state. At zero-field (a magnetic field of 0 T), the m_s = 0 and the degenerate m_s = $\pm$1 have a splitting of 2.87 GHz. Due to biased relaxation, optical excitation pushes the NV-center population (indicated by black circles) into the m_s= 0 state (Fig. 3.3 C). Upon application of an external magnetic field B_0, the previously degenerate m_s = $\pm$1 are now seperated. Microwave (MW) frequencies at 2.87 GHz - γB_0 can drive the transition between either m_s= 0 to m_s = -1 or m_s = +1. The Nv-center PL is spin-dependent, the m_s = 0 state is known as the "bright" state, indicated by the sun.

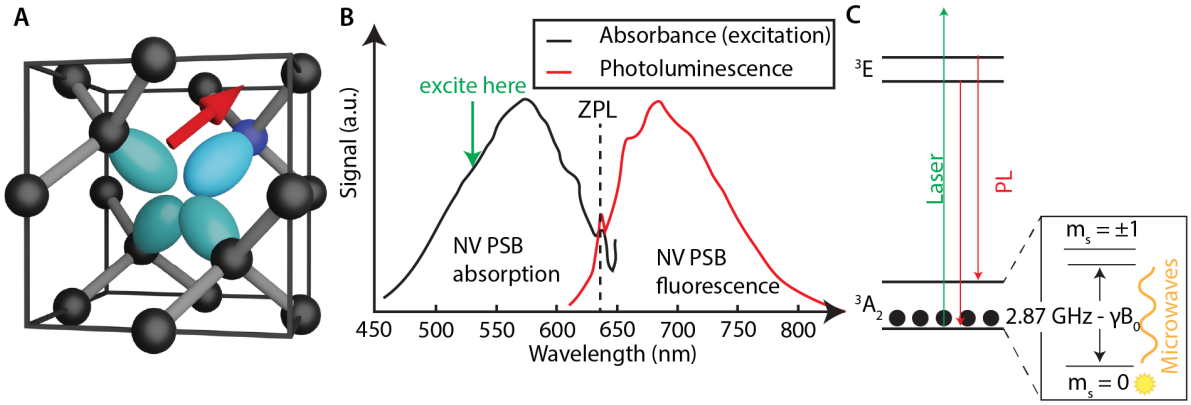

Figure 3.3.: a) Scheme of the nitrogen vacancy (NV) center within the diamond lattice. The carbon atoms are shown in black, the nitrogen atom in blue, the vacancy in the middle, and potential orientations with the active spin shown with a red arrow. b) Absorbance and photoluminescence spectra of the NV-center at 300 K. The zero-phonon line of 637 is depicted with a dotted black line. The non-resonant 532 nm excitation is indicated in green. Adapted from [15]. c) Energy level diagram of the electronic structure of the NV-center. The NV-center can be optically excited with preferential relaxation into the m_s = 0 state. Upon application of an external magnetic field B_0, microwaves can drive the transition from the m_s = 0 to either the m_s = -1 or +1 state.

3.3.2. The quantum environment in diamond

Diamond, in which NV-centers are embedded, is one of the allotrope forms of carbon. The crystal structure is characterized by each carbon atom being connected to the closest four

neighbouring atoms (1.44 Å) via covalent bonds, in a rigid lattice formation with tetrahedrally coordinated orbitals (sp^3-hybridization). This structure gives rise to the hardest naturally occurring material known to man, serving as the definition of 10 on the Mohs scale. At room temperature and atmospheric pressure, diamond has a density of 3.52 g/cm^3. It can withstand high temperature and pressures. Tensile strength is direction dependent, being strongest in the [100] direction (normal to the cubic face), smaller for the [110] and the smallest for the [111] axis (along the cubic diagonal). Diamond has been observed to be able to withstand pressures of up to 60 GPa, however it is estimated to be able to withstand more [16]. Diamond is thermally stable up to 700 °C in the presence of oxygen before it oxidizes [17]. In an inert atmosphere, it can go up to higher temperatures although it graphitizes [18]. Optically, it has a refractive index of n = 2.4. This high refractive index later means that light tends to be trapped within the diamond. Transparent from deep-ultraviolet to the infrared, isotropic, diamonds are commonly used for optical purposes [19]. The pure diamond is an electrical insulator with resistivity of 10^{16} $\Omega \cdot$ cm [20]. Furthermore, the chemical vapor deposition (CVD) method of growing synthetic diamond can use isotopicaly enriched ^{12}C carbon sources that can produce diamonds that are nuclear-spin-free[21]. These properties make diamond a magnetically, electrically, and mechanically "quiet" environment ideal for quantum applications, in our case quantum sensing [22].

3.3.3. Electronic grade diamond from chemical vapor deposition

Diamonds naturally form under intense pressures and temperatures (T > 1000 °C and P > 5 GPa). These conditions naturally occur within the earth's mantle (150 or more kilometres below the surface) [23]. Synthetic diamond creation has allowed for diamonds to be more readily available for a wide variety of applications. Microwave plasma assisted CVD has become a revolutionary technology with producing tailor-made diamonds with desired doping, isotopic purity and dimensions [24, 25]. So far, it has been mostly limited to research, since diamonds for which requirements for purity and quality are moderate can be produced more cheaply using high pressure and high temperature (HPHT) growth in apparatuses that

mimic the conditions of diamond formation which occur naturally in the earth [26]. Because the fabrication of high-quality thick crystals layer by layer is challenging and quite costly, HPHT still remains the primary method for producing bulk synthetic diamonds, while CVD is mostly focused on thin layers. [25]

The CVD technique works at low pressures (10–300 mbar) to thermodynamically stablilize graphite. Hydrogen plasma is used to preferentially etch away weak sp^2 bonds, thereby kinetically stabilizing the dangling bonds at the diamond surface and allowing carbon to be added to the diamond lattice of the substrate (Fig. 3.4 a) [27]. H_2 and CH_4 are used in a typical proportion of 95%–99% to 5%–1%, respectively.

O_2 in small amounts (<2%) is sometimes used in addition in order to increase the etching effect and limit impurity incorporation or defect formation.[21] To produce H_2, CH_4, or O_2 plasma, activation of the gas is performed through applying a 2.45 GHz MW field with a resonant cavity reactor [28]. High pressures (>100 mbar) and MW powers (>2 kW) lead to the formation of a localized plasma region within the core where temperatures may reach up to 3000 K, to produce the precursors for diamond growth. The temperature of the substrate holder is controlled from 700 – 1100 ° C, and growth proceeds on a diamond seed (Fig. 3.4 b-c). The preparation and selection of substrates is critical for optimal epitaxial overgrowth. Further polishing or etching of the surface prior to growth

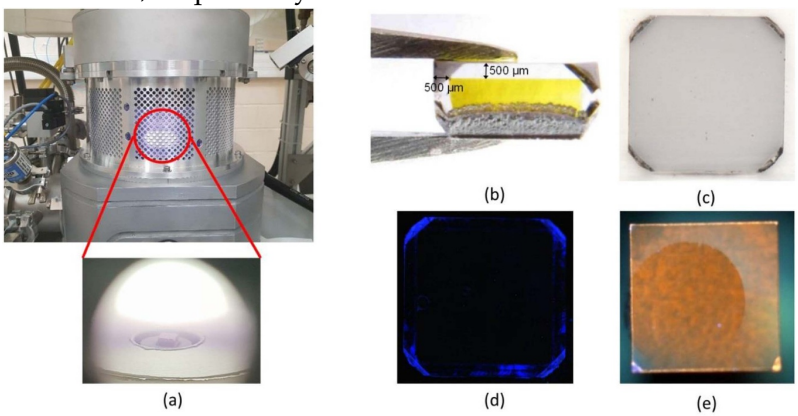

Figure 3.4.: (a) An MW plasma assisted CVD system. The inset shows a zoom into the plasma region in which a diamond is positioned for growth. (b) A high purity thick CVD diamond layer grown on a yellow HPHT diamond substrate and (c) CVD diamond obtained after removing the HPHT substrate (d) PL image of a high purity CVD diamond film showing weak blue luminescence in the corners corresponding to the presence of stress. (e) PL image of a N_2 doped CVD diamond film showing orange luminescence corresponding to the presence of both NV^0 and NV^- colour centres. Reprinted from [25] with permission.

helps to limit the proliferation of defects [29]. Maintaining consistent growth conditions, in particular temperature, for an extended period of time is also a limiting factor in the creation of thicker layers.[25] The culmination of years of research has produced pristine electronic grade diamonds with low nitrogen concentrations (a few ppb) ideal for hosting NV-centers (Fig. 3.4 d-e) [22].

3.3.4. Ion implantation and thermal annealing

Nitrogen is implanted into pristine CVD grown diamonds to produce shallow NV-centers used in this work for quantum sensing. As mentioned in the beginning of this introduction, sensing external spins on the diamond surface with high sensitivity relies on the fact that NV-centers are only a few nanometers aways from the surface, and yet still keep optical and spin properties at ambient conditions [30].

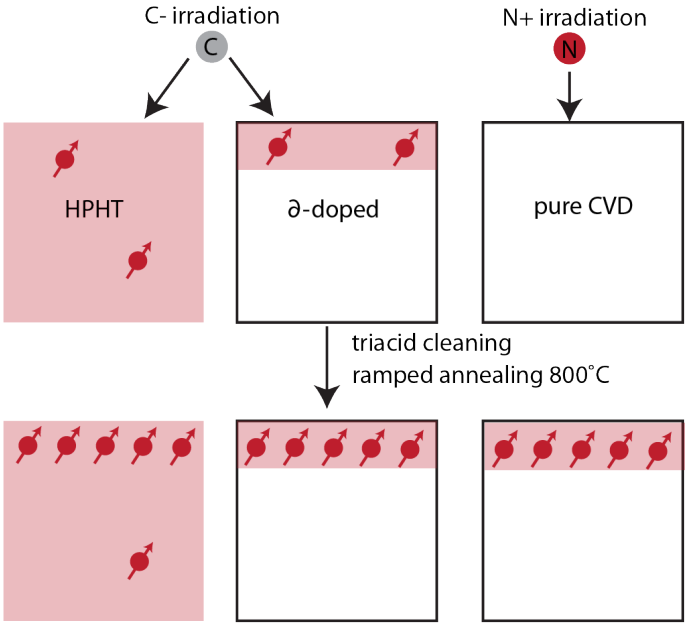

Figure 3.5.: Overview of the methods of NV layer formation

The NV-centers' magnetic sensitivity relies on having relatively long electronic T_2 coherence and T_1 spin relaxation times. Therefore, their precise positioning with nanometer accuracy beneath the diamond surface while preserving the coherence properties is essential. For this purpose, low-energy nitrogen implantation produces NV-centers with nanoscale depth. Implanted ions generate substitutional nitrogen impurities and vacancies simultaneously. To create NV-centers, the vacancies must diffuse to the substitutional nitrogen. This occurs with thermal annealing at 800 °C or above activates into NV-centers. [31–33] Although such a technique has been demonstrated for high implantation energies (MeV) a high conversion efficiency from im-

planted nitrogen to NV-centers (referred to as yield) approaching 50 %, this yield decreases rapidly for lower implantation energies (keV) along with having degraded spin coherence properties. [34] The resulting creation efficiency from ion implantation is well characterized and can be simulated using Stopping and Range of Ions in Matter software (see appendix A.5) [35–37]. Various methods have been investigated to improve properties. These include (but not limited to) doping with other nuclei, helium and electron irradiation, or irradiating diamond with existing nitrogen concentration, with a few methods more relevant for shallow NV-centers summarized in Figure 3.5 [34, 37–39].

3.3.5. Diamond surface and charge stability of NV-center

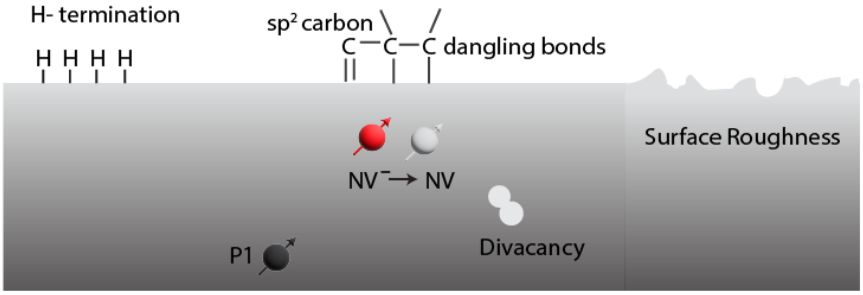

Figure 3.6.: (a) Cartoon summary of surface-related effects on NV-center properties such as H-termination, polishing, presence of P1 centers and divacancies as well as sp^2 carbon and dangling bonds.

As outlined in Figure 3.6, the diamond surface greatly affects the properties of shallow NV-centers. Mechanical polishing allows for flat surfaces with sub-nanometer roughness [40], which is highly beneficial for reducing magnetic or electric noise as well as improving charge stability. Damage from implantation may result in divacancies near the surface which may also be a source of charge instability. Charge state stability and photoluminescence, both crucial to quantum sensing using NV-centers, are known to be degraded near the surface of the diamond [41]. This is due to the fact that an abrupt end to the periodic crystal act as electronic traps, being a source of magnetic and electronic noise (such as the dangling bonds mentioned earlier). This results in less efficient conversion of nitrogen defects in the diamond

to vacancies [36, 37, 42]. Less conversion efficiency also leads to increased paramagnetic "P1 centers" or substitutional nitrogen. Therefore the extent to which NV properties are affected depend on level of impurities, structural defects and surface chemistry. Typically after the CVD growth process, the diamond is H-terminated. This contributes to diamond's unique properties such as its high chemical inertness and negative electron affinity (NEA).[22] The inertness of diamond has made surface alteration challenging, yet has not prevented the development of strategies to do so, especially in regards to nanodiamonds which have the benefit of large surface areas which makes chemical treatments more readily achievable [43]. NEA however, is destabilizing for negative charge properties, which is caused by surface band bending. Fortunately, the H-terminated diamond can be oxidized to form a oxygen-terminated surfaces consisting of a mixture of hydroxyl (C-OH), ether(C-O-C), carbonyl (C=O) or carboxylic acid (COOH) functional groups which reduces the band bending and allow for negatively charged NV-centers.[44]. Techniques to do so include but are not limited to - boiling in strongly oxidizing acids (sulfuric, nitric, and perchloric acid), oxygen annealing, piranha cleaning, or UV-ozone treatment [27, 45, 46]. Nitrogen or fluorine termination are also pertinent for having shallow NV-centers with decent properties [44]. It has also been shown that annealing at higher temperatures of 1100-1200 °C can remove paramagnetic defects from ion implantation [33].

3.4. Optically Detected Magnetic Resonance Spectroscopy

Due to its spin-dependent PL, which is weaker for the $m_s = \pm 1$ states compared to the $m_s = 0$ state, shallow NV-centers can be used as quantum sensors for optically detected NMR, commonly referred to as ODMR. We will refer to this as the NV-NMR experiment in the rest of this work. The fluorescence of NV-centers can be sensitive to magnetic fields from the Larmor precession of nuclei from samples near the surface of the diamond. NV-NMR translates these spin-state dependent changes in fluorescence intensity of the NV-centers to an oscillating signal (at the nuclear Larmor frequency). This involves incorporation of several

key experimental components: magnetic field, microwave excitation, optical excitation, data acquisition, and timing control.

3.4.1. Optical excitation

As shown in Figure 3.7, a 532 nm laser beam is commonly used for optical excitation of the NV-centers. After optical excitation, nearly all the NV-centers are in the $m_s = 0$ state (Fig. 3.3 B and C). For an experimental setup, the laser beam is focused with lenses at a distance of 40 cm before and after an Acoustic-Optic Modulator (AOM), which is employed to provide laser pulses with a timing of microseconds. After the AOM the controlled beam is guided through a $\lambda/2$-wave plate which polarizes the laser beam in the direction of the active quantum sensors.

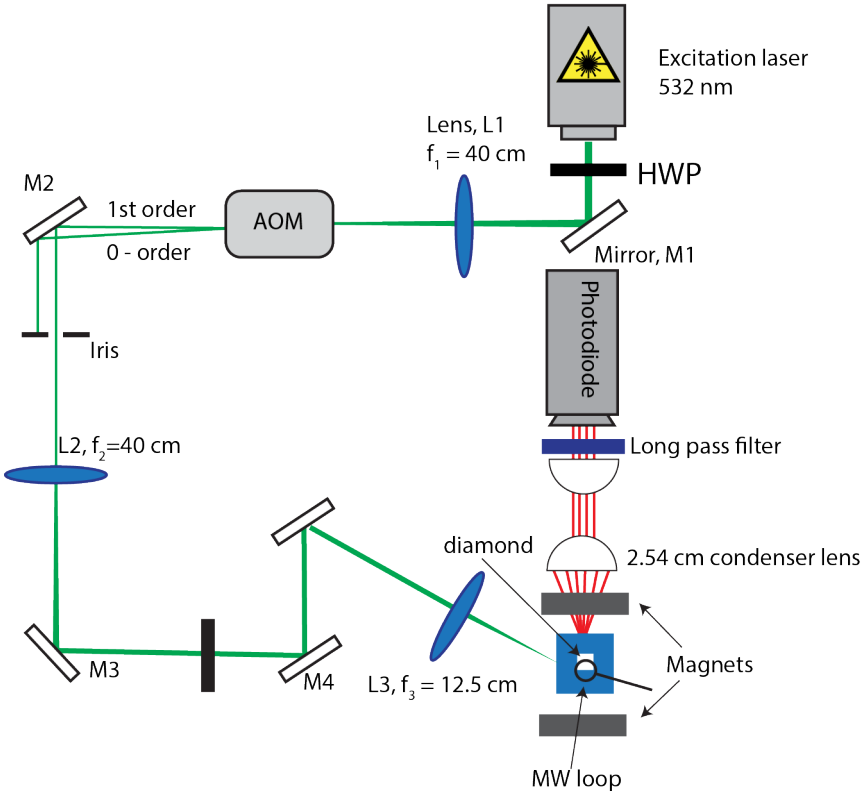

Figure 3.7.: Scheme of the NV-NMR experiment optical components.

3.4.2. Magnetic field and alignment

The degenerate $m_s = \pm 1$ states can be split by a static external magnetic field B_0. These defects can have four different orientations within the tetrahedral diamond lattice. The measurement volume of each NV-center [47, 48] can be described by a hemisphere whose radius is roughly their depth within the diamond (e.g., 5 to 10 nm). These nanoscale volumes correspond to a small number of spins, such that spin noise is much larger than thermal polarization [49, 50]. Therefore in nanoscale NV-NMR, the NMR signal strength does not require strong magnetic fields for generating thermal polarization, greatly reducing experimental complexity. NV-NMR spectroscopy can therefore be performed without strong magnets due to the detection of spin noise [51]. There is also no need to excite the nuclear spins with radiofrequency pulses or to wait for nuclear spin–lattice relaxation during signal acquisition as in conventional NMR.

For an NV-NMR experiment, the diamond can be positioned in the middle of two neodymium permanent magnets set on a rotation stage with a smaller rotation axis to control the tilt. This allow for alignment of the B_0 field with one of the four possible NV center orientations. These "ensemble" of NV-centers randomly sample the diamond surface within the laser spot (see Appendix A.6). Aligning the NV-centers can be done with knowledge of the [100] crystal face axis, where the NV is oriented at 54.74° angle from the surface normal. This alignment can be done by observing NV-ESR transitions (either $m_s = 0$ and $m_s = -1$ or $m_s = 0$ and $m_s = +1$). Each orientation has its unique transition frequency. Bringing three together in frequency ensures that the B_0 is in the direction of the fourth (Fig. 3.3 A) when the field has equal projection on the other three.

3.4.3. Quantum control using microwaves

Transitions between the $m_s = 0$ and $m_s = -1$ or $m_s = 0$ and $m_s = +1$ can be readily controlled with MW pulses. The full transition from one state to another is known as a Rabi π pulse. The competing optical pumping and MW excitation processes generate a contrast, or normalized

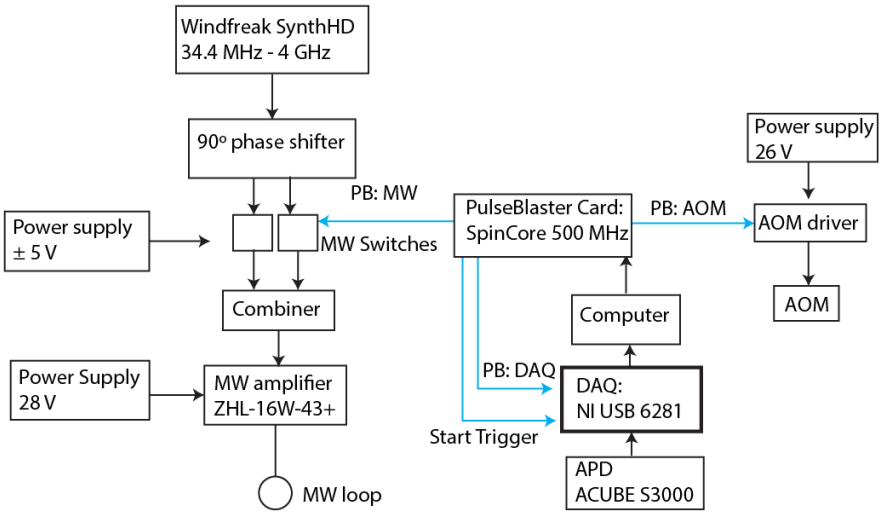

Figure 3.8.: Scheme of NV-NMR experiment electronic components.

difference in fluorescence or photoluminescence (PL). As shown in Figure 3.8, the MW pulses from a signal generator can be fed into a phase shifter to generate X and Y pulses which are 90 degrees phase shifted relative to each other. Each branch can be controlled using MW switches to produce nanosecond MW pulses. From the switches the MWs can then be combined and amplified by a MW amplifier to magnify the MW strength. The MWs are delivered by a home-build loop to the diamond [30].

3.4.4. Data collection

Finally the fluorescence from the diamond is collected on an Avalanche Photodiode (APD) detector as voltage. These can be logged using a counter in a data acquisition device (DAQ). For more details about equipment and methods, see Chapter 4.

3.4.5. Pulse Sequences

The timing of the laser excitation, MW quantum control, and data acquisition can be controlled by various methods, we have chosen to use a PulseBlaster (PB) card with 2 ns timing resolution. The pulse sequences and exemplary data are shown in Figure 3.10.

NV ESR

Electron spin resonance (ESR) experiments drive systems with electron spin such as NV-centers using MWs. For NV-centers, an on resonance MW causes population transfer from m_s = 0 to the less bright m_s = 1 or m_s = -1 state (depending on the frequency driven). This causes a fluorescence dip. As stated earlier, in the absence of a magnetic field, there are two resonances with a separation of $\sim$ 2.87 GHz at room temperature between them known as the zero-field splitting (Fig. 3.10 A). Upon application of a magnetic field, the ESR sequence can determine the NV resonance as well as the strength of the applied magnetic field using the equation:

$$B_0 = \frac{2.87GHz - f_{NV}}{28GHz/T} \quad (1)$$

Where f_{NV} is the transition frequency of the aligned NV-center. ESR requires PulseBlaster channels for the AOM, for the MW, and for the DAQ. For noise cancellation, the sequences is repeated without MWs. The MW frequencies are swept in the MHz or GHz range to find the NV driving frequency and to perform alignment.

Rabi

After finding the appropriate frequency for driving the NV-centers, the nutation behavior of the NV-center's spin states can be observed to determine the exact amount of power that needs to drive the NV-centers which is known as the Rabi oscillation. This Rabi oscillation specifies what is known as the $\frac{\pi}{2}$ and π pulses for quantum sensing experiments, where a π pulse fully drives the NV-centers from m_s = 0 to m_s = -1 or m_s = +1 (Fig. 3.9). Usually, the laser light polarization is adjusted by a $\lambda/2$ waveplate to maximize the Rabi contrast, which is defined by the fractional difference between difference between the minimum and maximum fluorescence intensity.

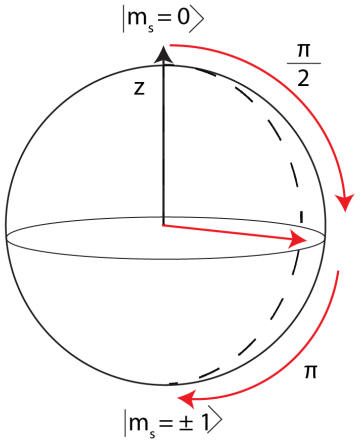

Figure 3.9.: Bloch sphere visualization of NV spin-state and Rabi pulses

This contrast is dependent on the laser power applied, NV coherence properties, and the

optical properties of materials above and below the NV layer (which may produce background light or absorb light). The amount of laser power is in our case 400 mW/ 4000 μm^2, which comes to approximately 10 kW/cm^2. The Rabi pulse sequence has the same channels as for ESR, and again the sequences are repeated without MWs for noise cancellation. The MW frequency is kept constant, but the time for which in our case with our applied MW power it is swept from 2 $-$ to 200 ns, which usually allows us to see more than one oscillation (Fig. 3.10 B).

NV-T_1

To measure NV-T1 (longitudinal) relaxation, the time t between AOM laser pulses is swept (Fig. 3.10 C). By sweeping the total sequence duration t, the fluorescence grows exponentially according to the longitudinal relaxation of the NVs from the m_s = -1 (or m_s = 1) state back into thermal equilibrium. In our case, the relaxation from m_s = -1 to the thermal state is measured by applying a π pulse on the NV after optical polarization. The pulse sequence requires the same PB channels as for ESR and Rabi. Typical NV-T1 relaxation times for shallow NV-centers at room temperature are from a few hundred μs to ms (see Appendix A.1.4).

NV-T_2

The spin echo or Hahn echo pulse sequence consists of $\frac{\pi}{2}_x - \tau - \pi_y - \tau - \frac{\pi}{2}_x$ where the time between MW pulses τ is swept (Fig. 3.10 D). In addition to the standard PB channels (AOM, MW, DAQ), an additional channel is needed for a different phase of the MW pulses (shifted 90 °). In the second sequence, the last $\frac{\pi}{2}$ pulse of the spin-echo is 180° relative to the first $\frac{\pi}{2}_x$ pulse for noise cancellation. This spin-echo sequence measures the transverse relaxation of the NV (along the XY plane of the Bloch sphere). The transverse relaxation is sensitive to slight variations in the Larmor precession due to inhomogeneously experienced magnetic fields by each NV-center due to contributions from nearby nuclear spins such as ^{13}C within the diamond. These differences in Larmor precession are observed as differences in orientation known as phase (the Bloch vector starting to rotate), which accumulates over time. Therefore, dips appear at the period of their Larmor frequency. For shallow NV ensembles, the T_2 coherence time is usually on the order of a few μs (see Appendix A.1.4).

3.4.6. Correlation Experiment and Filter Window

Precessing nuclear spins generate NMR signals as oscillating alternating current (AC) magnetic fields (B_{AC}). An appropriate AC magnetometry pulse sequence can be used to measure the fluctuations of the statistical polarization, or spin noise, mentioned earlier due to nanoscale volumes. Figure 3.11 shows sensing of the NMR signal. As shown by the Bloch spheres in Figure 3.11 B, the AC magnetometry pulse sequence begins with a $\frac{\pi}{2}$ pulse, with the quantum states in a superposition between the m_s = 0 and m_s = -1 states. This coherent superposition is then allowed to evolve for a specified free precession time τ, during which it accumulates phase in a manner that depends on the magnetic field being sensed.

A train of π pulses with defined phases is applied. The purpose of this sequence is both to extend the NV-center coherence time and to create a filter for magnetic signals. The correlation spectroscopy pulse sequence consists of two XY8-N MW "blocks" separated by a time spacing of t_{corr}. The time t_{corr} is swept and the spacing between the π pulses, τ, within the XY8-N sequences is set to detect the frequency f_{AC} where $\tau = \frac{1}{2f_{AC}}$. This is because if the time t_{corr} is this multiple of the AC signal period p_{AC}, the phase of the AC signal between the two dynamical decoupling sequences is the same and accumulates to a maximum, which is observed in the correlation signal. In contrast, a minimum is observed when the time t_{corr} is a

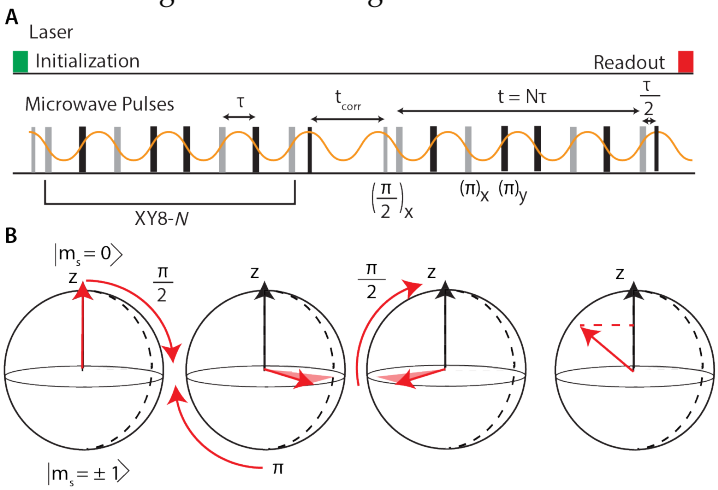

Figure 3.11.: a) Scheme of pulse sequence. The correlation spectroscopy pulse sequence consists of two XY8-N sequences. The timing t_{corr} is swept, which correlates the phases of nearby spin noise as oscillations in the readout data at the AC frequency. b) The corresponding Bloch sphere diagrams.

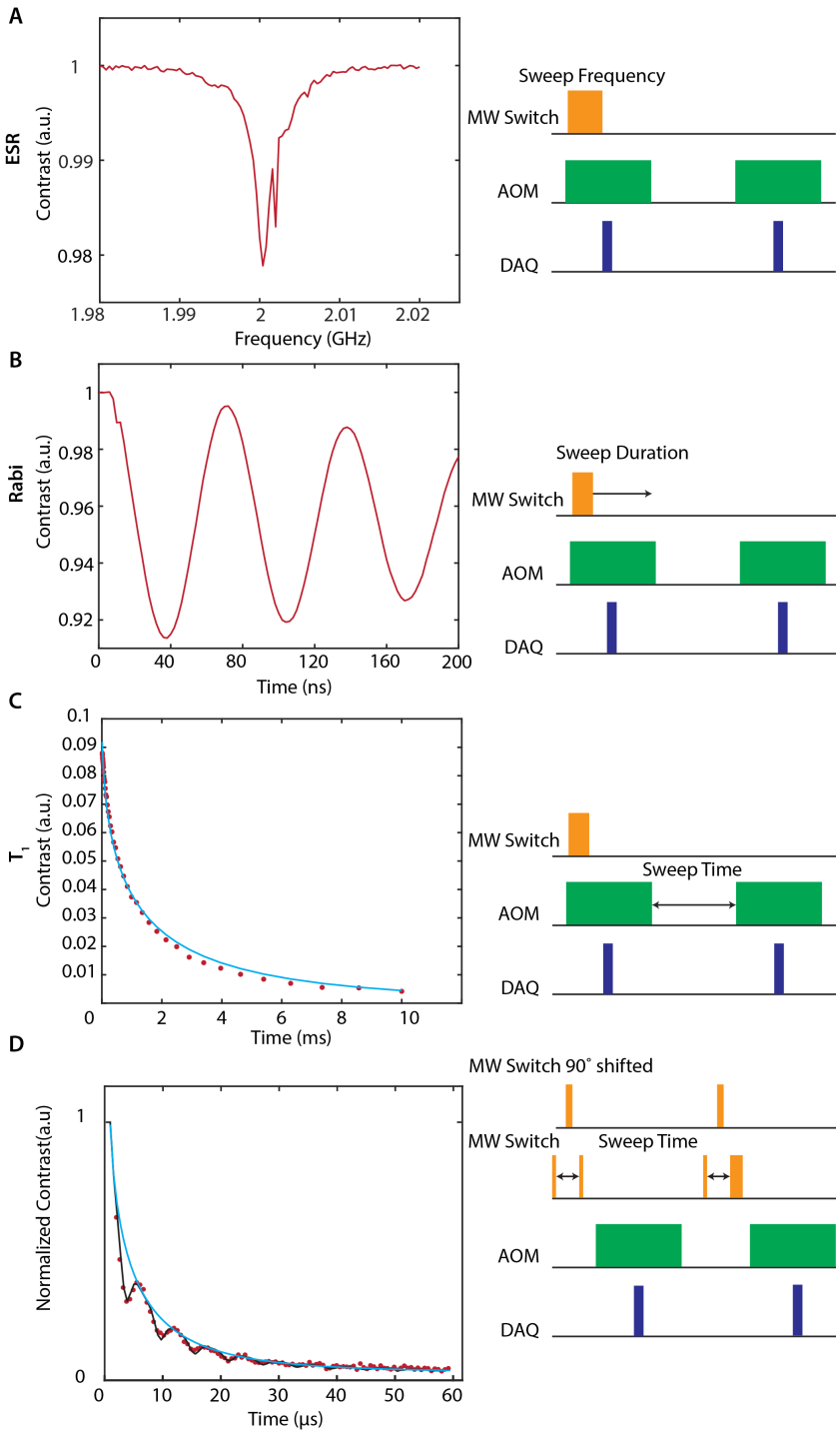

Figure 3.10.: Overview of pulse sequences. Left side: experimental data. Right side: Pulse-Blaster channels. A) ESR experiment at $\sim$ 174 mT. B) Rabi experiment C) T_1 experiment. D) Spin echo experiment.

multiple of $p_{AC}/2$ because the phase accumulation is opposite between the two dynamical sequences and cancels out. The correlation signal therefore oscillates at the frequency f_{AC}. The time that t_{corr} can be extended to is limited by the NV-T1 relaxation time. With an increase of N in XY8-N more signal can be detected, however at a cost of longer experimental times. The length of this train of π pulses is limited by the T_2 coherence properties of the NV-center. A final $\frac{\pi}{2}$ pulse translates the accumulated phase into a population difference between the two states and into a change in the NV-center fluorescence. When this $\frac{\pi}{2}$ pulse is around the same axis as the first, the signal responds quadratically with the strength of B_{AC}. This is known as cosine magnetometry. When the $\frac{\pi}{2}$ pulse is around the y-axis (or 90 $^\circ$ shifted), the signal responds linearly with the strength of B_{AC}, which is known as sine magnetometry.[52] In this work, we perform cosine magnetometry. For correlation spectroscopy, it is important to keep the π pulse shorter than the $\frac{\tau}{2}$ of the nuclei Larmor frequency to avoid overlapping pulses. Therefore we have a tunable magnetic field, using 174 mT ($\sim$ 3 MHz) for nuclei with low gyromagnetic ratios such as ^{31}P and 31 mT for nuclei with high gyromagnetic ratios such as ^{19}F ($\sim$ 1.2 MHz). That is because the correlation spectroscopy sequence used for quantum sensing is optimized for frequencies between 1 - 4 MHz. The spectral linewidths obtained for solid-state samples are on the order of kHz due to dipolar coupling.

The sensitivity of the decoupling sequence decreases with distance from the optimized frequency f_{AC}. This forms a "filter" with a sinc like appearance. Correlation spectroscopy performed with blocks of XY8-4 has much higher sensitivity and a much narrower sensitivity window in comparison to blocks of XY8-1. This filter window changes with the number of π pulses by $\Delta\nu = 1/N\tau$ [48], as we show here experimentally. We sweep the frequency of an AC signal source signal produced from a coil (f_{AC}) from 0.8 to 1.2 MHz. We detect the coil signal with a $\tau/2$ spacing of a period p_{AC} corresponding to 1 MHz frequency using 64 π pulses. Keeping the detection frequency constant, we see minimal suppression of less than 6 % of the signal 12 kHz above or below the 1 MHz detection frequency. This indicates that for linewidths of only a few kHz (the majority of our signal) the filter window does not majorly influence the lineshape. With less π pulses there would be an even broader “window” with

less suppression. However, we obtain more signal using more π pulses (i.e. 64 π pulses) with confidence that the linewidths are not majorly affected. We obtain a sinc like profile with the signal becoming being suppressed to about 10 percent of the 1 MHz optimum at or beyond 48 kHz away from the detection frequency.

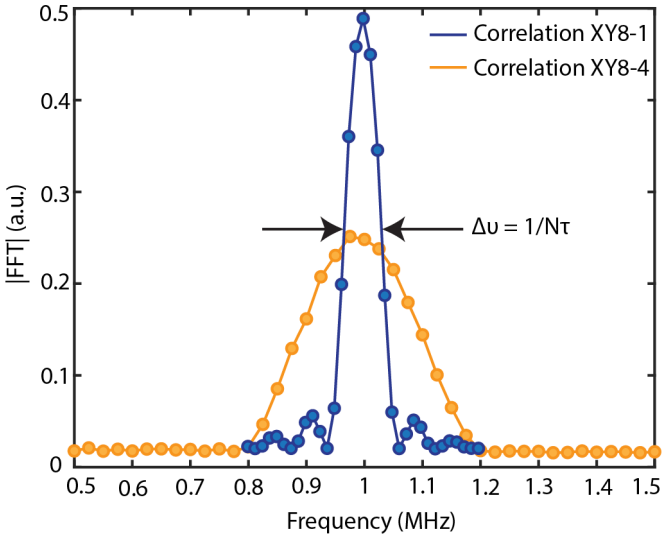

Figure 3.12.: Filter window of correlation experiment. Correlation using XY8-4 blocks has a much narrower filter window and higher obtained signal in comparison to correlation using XY8-1 blocks.

3.5. Application of NV-NMR to surface science

3.5.1. Atomic layer deposition of Al_2O_3

Through surface termination, we can obtain charge stabilized NV-centers with exceptional surface properties and corresponding photoluminescence and coherence properties. However, the low chemical reactivity is a limiting factor for using the diamond surface as a platform for investigating chemically or biologically relevant systems. Metal oxides are well known for the interaction of their surfaces with target molecules and its integration and compatibility with optical sensing techniques [53]. They are also commonly used as supports for catalytic processes [54]. Therefore, these properties are taken advantage of by using aluminum oxide

(Al_2O_3) as an adhesion layer on the diamond.

In this work we used it as a platform surface for both growing self-assembled monolayers (see Chapter 4) as well as metal-organic frameworks (see Chapter 5). A back-to-back publication with our work by Xie et al. has also used Al_2O_3 to immobilize biomolecules for quantum sensing [56]. Diamond-based sensing is also dependent on minimizing the distance from the target being sensed and the NV quantum sensor. Therefore, atomic layer deposition (ALD), a CVD technique which is able to make sub-nanometer thick material layers is used to deposit Al_2O_3 on the diamond [57]. ALD deposits these thin films based on a sequential use of gas-solid reactions.

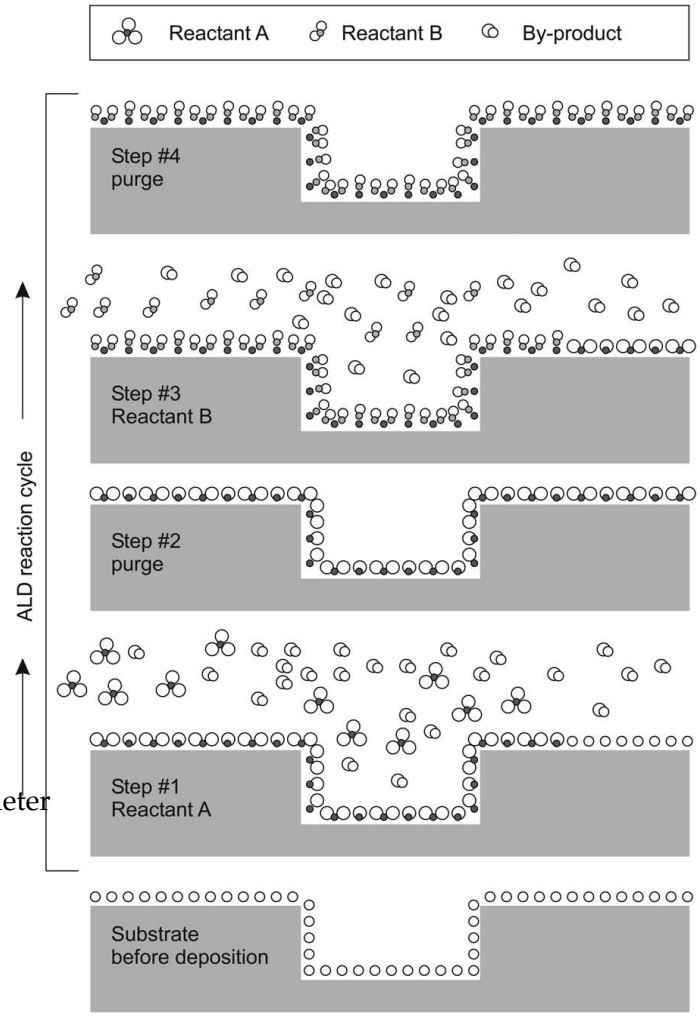

Figure 3.13.: Schematic illustration of one ALD reaction cycle. Reprinted from [55] with permission.

The layers are grown by repeating four characteristic steps (Fig. 3.13):

1) A self-terminating reaction of the first reactant (A)

2) A purge or evacuation to remove excess reactants and by-products from the reaction

3) A self-terminating reaction of the second reactant (B), or a surface activation for another reaction with reactant (A)

ALD processes have been developed for producing various inorganic solid materials including but not limited to oxide, nitrides, sulphides, tellurides, as well as pure elements. The

metal reactants in these precursors much be volatile at the elevated temperatures that ALD devices can support. [55]

For the growth of an oxide, a organometallic precursor have ligands that are replaced by an oxygen source. H_2O is used generally, but O_3 is used more often at higher temperatures. In our case, trimethyl aluminum ($AlMe_3$) is used as a precursor, with H_2O) as an oxidant reacting together to form Al_2O_3. The methods for the ALD process used is as described in Chapter 4.

The $AlMe_3/H_2O$ process occurs with the following stoichiometry[58]:
$Al(CH_3)_3$ (g) + $3/2H_2O$ (g) $\rightarrow$ $1/2Al_2O_3$ (s) + $3CH_4$ (g)
OH groups on the diamond react with $AlMe_3$ through ligand exchange for chemisorption to the surface of the diamond, producing O-Al bonds and releasing methane [59]. This occurs at elevated temperatures, 200 °C in our case.

3.5.2. Phosphonic acid based self-assembled monolayer formation on Al_2O_3

On the oxide surface formed by ALD, we prepare a monolayer of organic molecules for the work in Chapter 4. In general organic molecules that form self-assembled monolayers (SAMs) consist of two main parts: The first being an anchor group which is responsible for the adsorption to the surface. The second part is the linker or spacer, which are often alkyl chains or aromatic residues.[60] The intermolecular interaction is influenced mainly by this part, and therefore it is highly important for the ordering of the monolayer. In general, longer spacers result in a SAM with a higher degree of order [61, 62]. Energetically, the most favorable structure for the alkyl chains are tilted. In Chapter 4, we use phosphonic acid to form a monolayer on Al_2O_3. This system has a maximum packing density of 5 molecules/nm^2 [63]. The stability of the monolayer depends also on the stability of the organic molecules that form them. The molecules may either desorb or undergo a (reversible) phase transition.

Due to the anchor group having three oxygen atoms, phosphonic acids can bind in different modes. Most experimental studies indicate at least bidentate and often tridentate binding of

the surfactant molecules, which result in high monolayer stability (Fig. 3.14).[64]

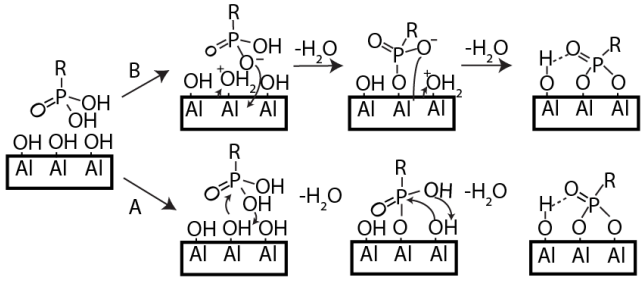

Figure 3.14.: Mechanism for attaching phosphonic acid molecules on hydroxylated metal oxide surfaces for basic adsorption sites (B) and acidic sites (A).

As shown in Figure 3.14, there are two routes for the grafting of the phosphonic acid onto the oxide. For acidic absorption sites, the hydroxyl oxygen on the phosphonic acid interacts with a proton of the hydroxyl group on the oxide. The oxygen of the oxide hydroxyl then binds to the phosphorus atom, and a H_2O molecule is released. This process is repeated to obtain the bidentate binding as shown. For basic absorption sites, the negatively charged oxygen on the phosphonic acid binds to the metal and replaces a H_2O. This process repeats for bidentate binding. These mechanisms show that a major consideration for the monolayer formation is the treatment of the surface. To ensure that the oxide surface is well covered with hydroxyl groups for grafting of the phosphonic acid, we expose the surface to O_2 plasma. A second key consideration for SAM formation is the polarity of the solvent used. Highly polar solvents make it favorable for the packing of hydrophobic moieties such as alkyl chain spacers and solvates the polar anchor group. It is also worth noting that protic solvents slow down adsorption by competing for binding sites on oxide surfaces.[65] Therefore, ethanol was chosen as the solvent we use in our work.

3.5.3. Layer by layer growth of UiO-66 SURMOF

At the nanoscale, molecular motion such as from diffusion limits the interaction time between molecules and a NV-center. There are different ways to model this behavior, one of which is the exponential decay. Considering an interaction time τ_d of a lipid molecule, the probability of a molecule staying within the sensing volume decreases exponentially with time. The Fourier transform of this decay result in a Lorentzian line shape commonly written as:

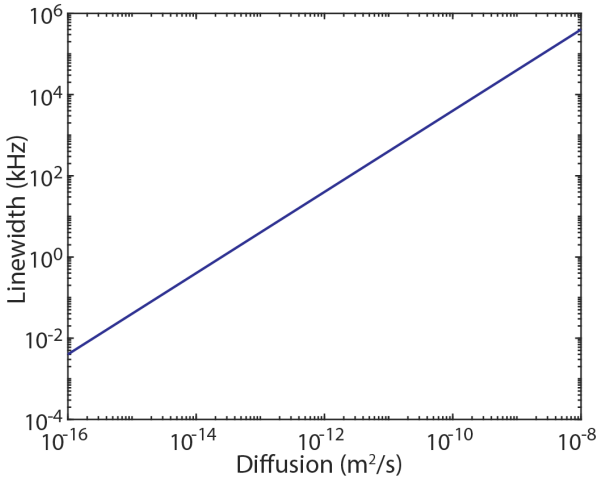

Figure 3.15.: Influence of diffusion on linewidth detected by shallow 5 nm NV as calculated from equation 3.

$$L(\tau,\omega) = \frac{1}{\pi} \frac{\tau_d}{1 + (\omega - \omega_0)^2 \tau_d} \quad (2)$$

where ω_0 specifies the center and τ_d is a parameter that determines the width. τ_d can be related to molecular diffusion by considering the linewidth, with a full width at half maximum (FWHM) $\frac{2}{\tau_d^2}$:

$$\tau_d = \frac{2d_{NV}^2}{D} \quad (3)$$

where d_{NV} is the depth of the NV and D is the diffusion coefficient (Fig. 3.15).[66]

As shown in Figure 3.15, diffusion broadens the signal detected by a shallow NV-center implanted on average 5 nm below the surfaces, making liquid-state molecules undetectable. Therefore we use a thin film of a special porous material, metal-organic frameworks (MOFs) to "trap" molecules within their pores and restrict diffusion. This would allow us to go beyond tethered molecules such as the self assembled monolayers in studying surfaces [49, 67]. In general, MOFs consists of metal ions or clusters, sometimes referred to as inorganic nodes, connected together by organic linkers. The term secondary building unit (SBU) is often used, which refers to the metal node including the coordinating functional groups [68]. The crystallization process is a tremendously complex topic as kinetic, thermodynamic, and entropic considerations must be taken into account. Typically, MOFs are produced in high

boiling organic solvents such as DMF at high temperatures under solvothermal conditions. For the modulation of the bond formation kinetics, accelerating bases or decelerating carboxylic acids can be added.

This allowed for the engineering of MOFs with defects such as missing linkers to increase porosity[69]. Liquid-phase epitaxy (LPE) is a method for the deposition of well-ordered materials in liquid phase. In the field of MOF growth, LPE is often synonymously used as a layer-by-layer deposition. The LPE method of MOF growth is a technique for thin film fabrication. Experimentally, the substrate surface is alternatively immersed in a metal precursor and organic linker solution (Fig. 3.16) [70]. The substrate is cleaned in between immersions with solvent to remove unreacted molecules from the surface. The LPE process produces smooth MOF thin films, which are known as surface mounted MOFs (SURMOFs) [71]. The thickness of these films can be controlled precisely by the number of LPE cycles. In Chapter 5 we use this method to produce thin films of UiO-66. This work is a step towards an application of NV-NMR to material science and studying the various processes that MOFs or other porous materials such as covalent organic frameworks are involved in [72]. These include the trapping of toxic chemical warfare agents or electrochemical reactons [73, 74].

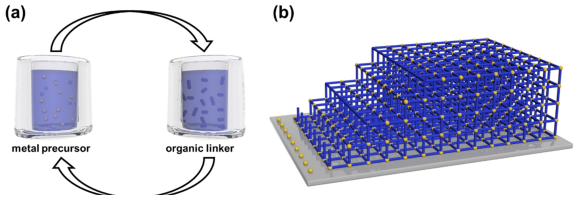

Figure 3.16.: Schematic representation of the LPE approach. A substrate is alternatively immersed in a metal precursor and an organic linker solution (a), resulting in the formation of an MOF thin film on the substrate (b). Reprinted with permission from A.Semrau et al. Langmuir 2021 37 (23), Copyright 2021 American Chemical Society.

3.5.4. Vesicle fusion formation of lipid bilayers on diamond

The work in Chapter 6 applied NV-NMR to study a model biological surface system, supported lipid bilayers (SLBs). Supported lipid bilayers are 2D films of phospholipid bilayers. They are mimetic of biological systems ranging from cell membranes to exosomes and viruses and can be used to study their interactions with small molecule such as drugs and cholestrol [75–77]. They are termed "supported" due to their formation on a solid substrate [78]. For

their fabrication, the vesicle fusion due to adsorption and rupture of lipid vesicles on a surface is commonly used.[79] Attractive interactions, such as van der Waals and electrostatic forces, between a vesicle and a solid surface it is in contact with causes the vesicle to adsorb onto the surface.[80] Depending on this interaction strength, an adsorbed vesicle may alter and deform and either remains intact or finally ruptures. The vesicle fusion process involves involves vesicle adsorption, deformation, and eventual rupture on a solid surface. As illustrated in Figure 3.17, vesicle fusion is challenging, as there are numerous factors that influence SLB formation success. Vesicle properties that impact the formation include lipid composition [81], size [82], and of course the pH, ionic strength and osmotic pressure of the solution [83]. The properties of the solid surface that affects SLB formation includes its atomic composition and morphology[84, 85]. Therefore, vesicle fusion works only on a narrow range of solid surfaces.

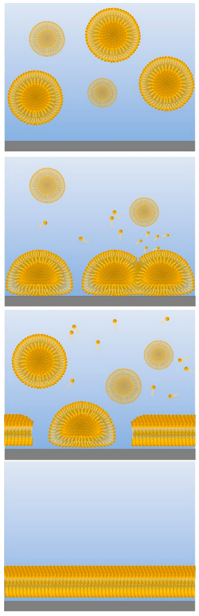

Figure 3.17.: The vesicle fusion method. Adapted with permission from Jackman, J. A. et al. Langmuir 2020, 36 (6), 1387–1400. Copyright 2020 American Chemical Society.

4. Surface NMR using quantum sensors in diamond

This chapter is adapted from a paper published in *Proceedings of the National Academy of Sciences of the United States of America* Volume Edition **2022** Vol. 119, No. 5 e2111607119
https://www.pnas.org/doi/10.1073/pnas.2111607119l
By Kristina S. Liu, Alex Henning, Markus W. Heindl, Robin D. Allert, Johannes D. Bartl, Ian D. Sharp, Roberto Rizzato, Dominik B. Bucher

Data Availability. Raw data have been deposited in Zenodo (link). All other study data are in the Appendix.
Author contributions:
D.B.B. designed research; K.S.L. and R.R. performed research; A.H., M.W.H., R.D.A., J.D.B., and I.D.S. contributed new reagents/analytic tools; K.S.L., A.H., R.R., and D.B.B. analyzed data; and K.S.L., R.R., and D.B.B. wrote the paper.

4.1. Synopsis

Many of the functions and applications of materials in catalysis, energy conversion, drug delivery, bioanalysis and electronics are based on their interfacial properties and structures. Characterization of their molecular properties under ambient or chemically reactive conditions is a fundamental scientific challenge. NMR is a non-invasive, molecular level spectroscopic

technique widely used for chemical characterization and would be ideal for probing surfaces and interfaces under ambient conditions. However, it lacks the sensitivity to probe the small number of spins at surfaces and interfaces. Here we use nitrogen vacancy (NV) centers in diamond as quantum sensors to optically detect NMR signals from chemically modified thin films. To demonstrate the method's capabilities, aluminum oxide (Al_2O_3) layers, common supports in catalysis and materials science, are prepared by atomic layer deposition and are subsequently functionalized by phosphonate chemistry to form self-assembled monolayers. The surface NV-NMR technique detects spatially resolved NMR signals from the monolayer, indicates chemical binding, and quantifies molecular coverage. In addition, it can monitor in real-time the formation kinetics at the solid-liquid interface. Here we develop a surface-sensitive magnetic resonance technique that combines the nanoscale sensing capabilities of defects in diamond with a high precision and versatile protocol for diamond surface modification. With our approach, we show that NV quantum sensors are a surface-sensitive NMR tool with femtomole sensitivity for in-situ analysis in catalysis, materials and biological research.

4.2. Introduction

The characterization of surface processes at the molecular level is essential for understanding fundamental processes in industrial catalysis, energy conversion, electronic circuits, targeted drug delivery, and biosensing [86]. However, many analytical techniques used in surface science are inaccessible under ambient or chemically relevant conditions. Therefore, it remains challenging to perform chemical analysis under the conditions in which these processes occur [10, 87]. Commonly used surface sensitive methods, such as X-ray photoelectron spectroscopy (XPS), Auger electron spectroscopy, and secondary ion mass spectroscopy can perform chemical analysis but require ultra-high vacuum and expensive equipment [88]. Great efforts have been devoted to extending XPS analysis to near ambient conditions [10]. Indeed, both near-ambient pressure XPS and extended X-ray absorption fine structure have

significantly expanded the applicability of these X-ray–based techniques for understanding reaction mechanisms at chemically active interfaces [10, 89]. However, both methods require intense synchrotron radiation to achieve high sensitivity and resolution, which limits their practical accessibility and increases their cost. State-of-the-art surface-sensitive spectroscopy techniques, such as sum frequency generation and second harmonic generation, can perform analysis under ambient conditions but require technically complex equipment such as femtosecond lasers [90]. Even with all these techniques available, molecular dynamics or chemical reaction kinetics at surfaces are still challenging to probe experimentally [91](Appendix A.1.2: Comparing established surface techniques to surface NV-NMR).

NMR spectroscopy is one of the major tools for chemical and structural analysis in chemistry, biology, and materials science.Solid-state NMR in particular [92] has advanced understanding of a range of systems, including metal organic frameworks [93], batteries [94], and catalysts [95]. However, sensitivity remains a challenge for traditional NMR spectroscopy, making studies at surfaces difficult because of the limited numbers of nuclear spins. Recently, surface-enhanced NMR spectroscopy (DNP-SENS) relying on hyperpolarization such as dynamic nuclear polarization [2, 3] or xenon-based techniques [96] gained research momentum and enabled probing spins located at surfaces. However, even in highly porous materials with greater than 1,000 m^2/g surface area, the concentration of NMR-active nuclei of interest often remains low (e.g., 1 mmol of surface atoms/g), which requires long averaging times to obtain solid-state NMR spectra with reasonable signal-to-noise ratios (SNR) [3] (Appendix A.1.1: Comparing DNP-SENS to surface NV-NMR).

Here, we demonstrate the use of quantum sensors in diamond as a surface-sensitive spectroscopy technique that works at ambient conditions and can probe planar interfaces on the microscopic length scale with far greater sensitivity (femtomoles, see Materials and Methods) than conventional NMR. The spectroscopic technique relies on the nitrogen vacancy (NV) point defect, consisting of a nitrogen impurity (N) and an adjacent vacancy (V) in the carbon lattice of diamond. These spin-1 defects allow for optical detection of magnetic resonance and have been established as highly sensitive nanoscale magnetic field sensors [97, 98]. Near-

surface NV centers are sensitive to magnetic fields from the Larmor precession of nuclei from samples positioned outside of the diamond. This enables nanoscale NMR detection—even down to a single molecule [99] or spin [6, 100]. The measurement volume of such NV sensors [47, 48] corresponds to a hemisphere whose radius is roughly their depth below the surface in the diamond lattice (e.g., 5 to 10 nm). At this small length scale, the thermal polarization of the nuclear spins can be neglected since spin noise dominates for a small number of spins [49, 50]. For that reason, the NMR signal strength is independent of the applied magnetic field B_0, reducing experimental complexity and costs,which makes the technique accessible to a broader community. Previously published nanoscale NV-NMR experiments detected NMR signals from either bulk samples [such as viscous oils [7, 48, 49] or samples tethered to [99] or placed directly on the diamond surface [101]. In this work, we propose the use of NV centers in diamond combined with state-of-the-art thin film deposition techniques as a general platform to detect NMR signals with high sensitivity and spatial resolution even from nondiamond surfaces. This approach is general and allows for the probing of a variety of surfaces and interfaces with NMR, thereby enabling their chemistry to be explored. Here, we use atomic layer deposition (ALD), a technology that can be applied to synthesize films of a wide variety of materials with high thickness precision to coat the diamond with amorphous aluminum oxide (Al_2O_3). Al_2O_3 provides an exemplary surface of high technical relevance in optoelectronic applications and acts as structural support in various catalytic processes [54]. In a proof-of-concept study for this surface-sensitive spectroscopic technique, we probe the chemical modification of the Al_2O_3 surface with phosphonate anchoring during the formation of a self-assembling monolayer (SAM) [102].

4.3. Results

4.3.1. Surface NV-NMR

The surface NV-NMR technique is performed on a diamond chip in which ^{15}N was implanted with a particle fluence of $2 \times 10^{12}/cm^2$ and with an energy of 2.5 keV (Fig. 4.1 A) (Appendix

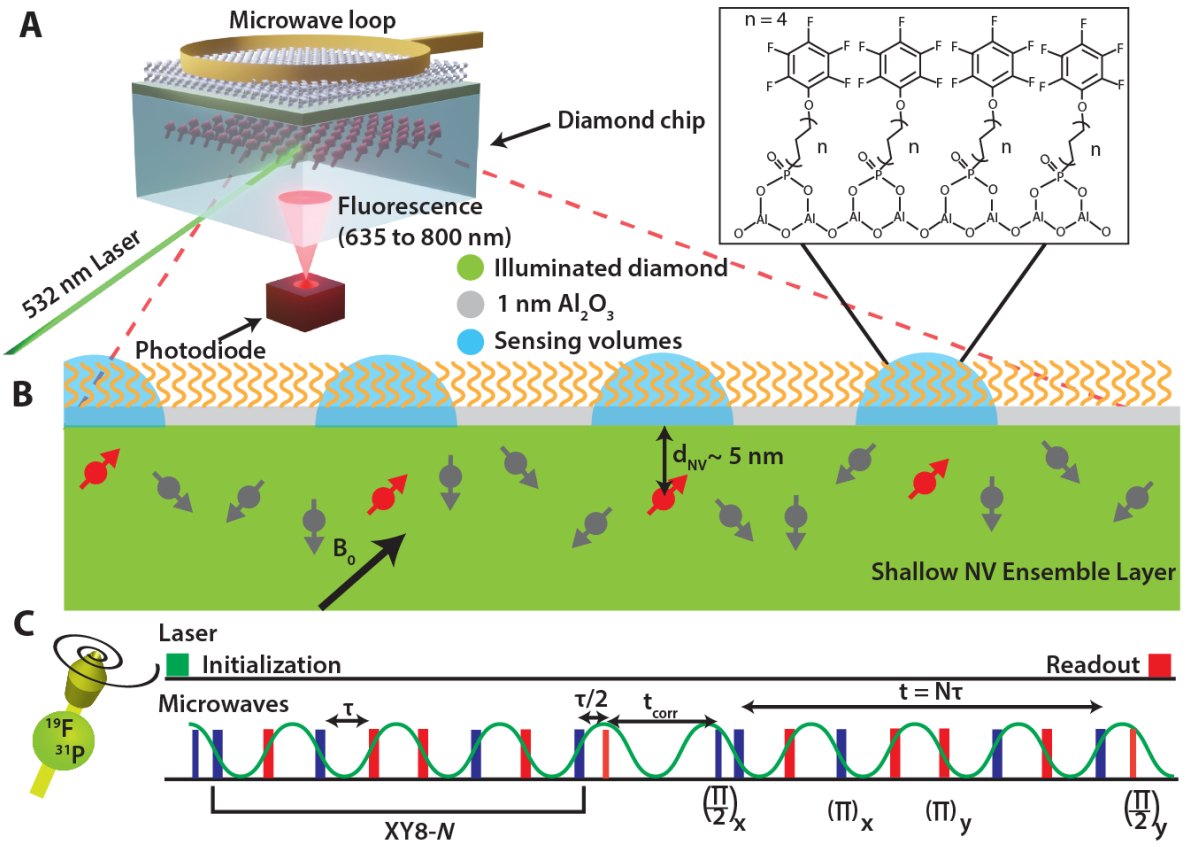

Figure 4.1.: **Surface NV-NMR spectroscopy on a functionalized metal oxide surface.** (A) Scheme of the experiment. Near surface NV centers in a 2 × 2 × 0.5 mm diamond chip are excited with a 532-nm laser in a total internal reflection geometry. The resulting spin-dependent photoluminescence from the NV defects is detected with an avalanche photodiode. The microwave pulses for quantum control of the spin state of the defects are delivered through a small wire loop. (B) NV centers aligned with the magnetic field have sensing volumes with a radius determined by their distance to the surface, 4.5 ± 1.9 nm in our case. (Inset) Schematic of an organic monolayer formed from PFPDPA on 1 nm Al_2O_3 deposited on the diamond surface by ALD. (C) Correlation spectroscopy pulse sequence. Two blocks of dynamic decoupling XY8-N sequences are correlated by sweeping the time between them (t_{corr}). The time spacing τ between the π pulses is set to half the period of the Larmor frequency of the nuclear spin being sensed. The NV spin state is initialized with a 532-nm laser pulse, and photoluminescence detection with a photodiode occurs after the microwave pulse sequence.

A.1.3: Annealing of implanted diamond for conversion to NV centers and A.1.4: Properties of NV centers after annealing), resulting in a distribution of near-surface NV centers 4.5 ± 1.9 nm below the surface (Appendix A.1.5: SRIM simulation of ^{15}N implantation depth). For these implant conditions, we estimate an NV density of ∼50 to 100 NVs/μm^2 [36, 37, 42], corresponding to 2 to 4 × 10^5 NV centers for the ∼4,000μm^2 spot used in our experiments as shown in Fig. 4.2 C (Appendix A.1.6: Gaussian fitting of laser spot size). These defects can have four different orientations in the tetrahedral diamond lattice; thus, one in four is aligned with the external magnetic field B_0. Consequently, an effective ensemble of ∼0.5 to 1 × 10^5 NV centers allows for random NMR sampling of the diamond surface within the laser spot. The NMR detection volume of each NV center is determined by its depth, indicated schematically as blue hemispheres in Fig. 4.1 B. The quantum-sensing scheme for detecting NMR signals with NV centers in diamond has been described in detail before [30, 49, 103, 104]. In brief, the electronic ground state of the NV center is a spin triplet with the Zeeman states m_s = 0 and ± 1, which are separated by ∼ 2.87 GHz at zero magnetic field. The degenerate m_s = ± 1 states are typically split by a static external magnetic field B_0, and transitions between the Zeeman split states can be addressed by microwave fields. The spin state of the NV center can be initialized in the m_s = 0 state with laser excitation at a wavelength of 532 nm and optically read out because of spin-dependent photoluminescence (PL), which is weaker for the m_s = ± 1 states compared to the m_s = 0 state. After optical excitation, nearly all the NV spins are in the m_s = 0 state. Subsequently, transitions between the m_s = 0 and m_s = ± 1 can be coherently controlled with microwave pulses. Dynamic decoupling sequences optimized for nuclear spin noise detection (such as XY8-N) are used because synchronized pulse schemes (such as the coherently averaged synchronized readout [CASR] protocol) detects thermal NMR signals [105, 106] inefficiently. These sequences are sensitive to frequencies corresponding to $1/(2\tau)$, where τ is the spacing between the π pulses (Fig. 4.1 C). Sweeping the time t_{corr} between two XY8-N sequences correlates oscillating magnetic fields such as spin noise from the Larmor precession of nanoscale nuclear spin ensembles (measured in B^2_{rms}). The detected spin noise appears as oscillations in the PL readout as a function of t_{corr} and resembles the free induction

decay in traditional NMR spectroscopy. However, this nanoscale NMR spectroscopy can be performed without strong magnets due to the detection of spin noise. Notably, there is no need to excite the nuclear spins with radiofrequency pulses or to wait for nuclear spin–lattice relaxation during signal acquisition.

4.3.2. Characterization of the Metal Oxide Layer

In prior works, NMR signals from samples directly on the diamond surface have been detected [37, 49]. Here, the goal is to probe nondiamond surfaces and interfaces. This requires the preparation of a material of interest on top of the diamond substrate. Our proof-of-concept study uses an Al_2O_3 film prepared by ALD [107], whose surface modification with organophosphonate chemistry shall be investigated through the surface NV-NMR technique. First, we optimized the thickness of the ALD layer by keeping it as thin as possible, allowing the NV centers to sense the surface modification while also ensuring that it was thick enough to create a closed film onto which a dense molecular monolayer could be bound. The formation of the fluorinated monolayer on the Al_2O_3 surface increases the surface hydrophobicity, which can be investigated with static water contact angle (SWCA) measurements. The minimal ALD layer thickness required to facilitate the formation of a dense SAM was determined using SWCA measurements as a function of Al_2O_3 thickness from 0.5 to 3 nm. The saturation of the SWCA signal appears for ALD layers of 1 nm and beyond (Appendix A.1.7: Determining optimal Al_2O_3layer thickness for monolayer assembly), which indicated that we reached the minimal thickness required for the organic monolayer to be fully formed. The hardness of the diamond chip allows for a scratching experiment to corroborate the thickness of the Al_2O_3 layer on the diamond using atomic force microscopy (AFM) (Fig. 4.2 A).

Removing the Al_2O_3 with the AFM tip revealed two different surfaces— the Al_2O_3 with an RMS roughness of 0.71 nm and the underlying diamond with a roughness of 0.25 nm. A vertical cut showed a step height of 0.9 ± 0.1 nm, confirming the thickness expected for 10 ALD cycles [55]. Second, we ensure that the material preserves the NV center properties by

quantifying the coherence times before and after depositing the Al_2O_3 film on the diamond. We observe a small reduction in the spin–lattice relaxation T_1 and spin–spin relaxation T_2 times (Table 4.1), with only a minor influence on the NV-NMR sensitivity.

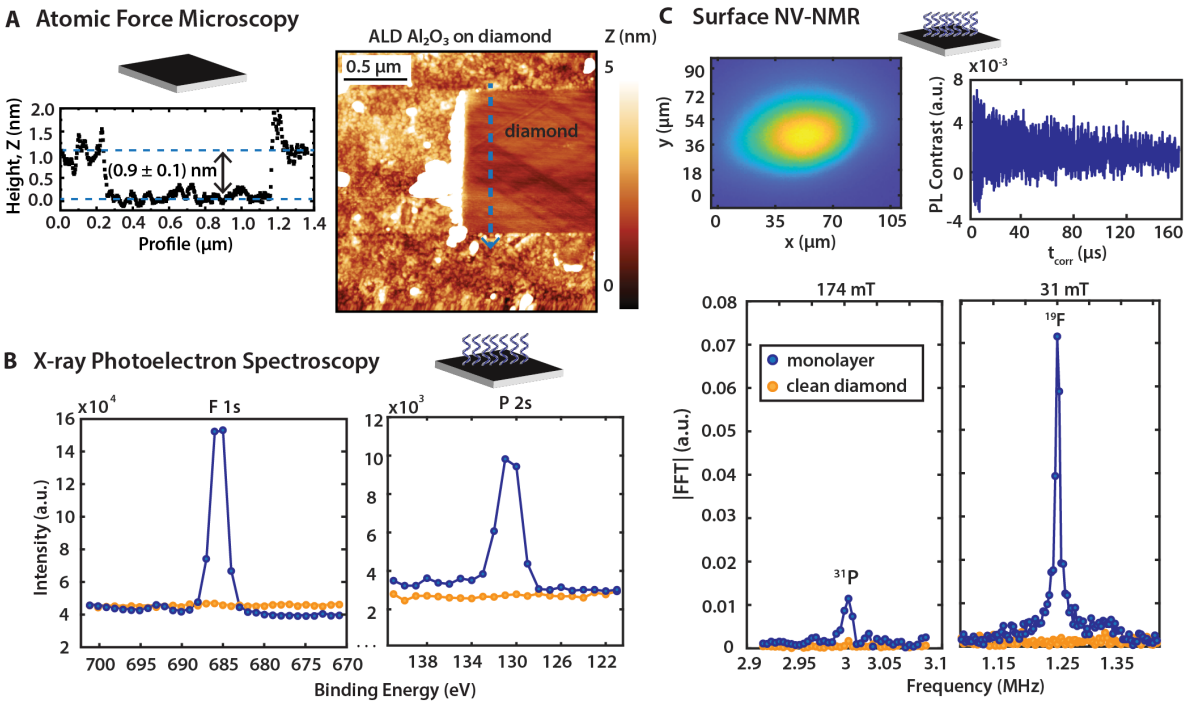

Figure 4.2.: **Surface NV-NMR and validation with complementary analytical surface techniques.** (A) Diamond coated with an Al_2O_3 layer. The thickness of the ALD-deposited Al_2O_3 layer was determined by AFM scratching measurements. The height profile along the segment indicated by a blue arrow was used to determine the Al_2O_3 film thickness of 0.9 ± 0.1 nm. (B) Functionalized Al_2O_3 surface on diamond. The presence of PFPDPA molecules on the surface is confirmed with XPS by the appearance of F 1s and P 2s peaks (blue), which are absent on the clean diamond (yellow). (C) Surface NV-NMR spectroscopy. (Top) Image of the laser spot ($\sim$ 4,000 μm^2) on the diamond and time domain correlation signal of ^{19}F. (Bottom) Surface NV-NMR spectrum of ^{31}P detected from the monolayer measured at 174 mT and ^{19}F nuclei detected at 31 mT. The clean diamond reference is shown in yellow.

4.3.3. Chemical Characterization of the Functionalized Metal Oxide Support.

Following thickness optimization, we analyzed the chemical composition of the functionalized Al_2O_3 layer. We selected a C12 chain phosphonic acid (PA) terminated with a fluorinated phenolic ring (12-Pentafluorophenoxydodecylphosphonic acid [PFPDPA]) for chemical mod-

ification of the Al_2O_3 surface. The functionalization occurs via the binding of phosphonic acid groups to the hydroxy groups of the Al_2O_3 surface. Fig. 4.1 B illustrates the bridged bidentate-binding motif. We note, however, that multiple binding modes might be present on the surface [64]. These fluorinated monolayers can be easily prepared by soaking the Al_2O_3/diamond in the PA solution. X-ray photoelectron spectroscopy (XPS) confirmed the presence of the F 1s peak and P 2s peaks from the monolayer (4.2 B). Corresponding spectra from the bare substrate prior to functionalization did not contain any detectable fluorine or phosphorous. Thus, the phosphorous and fluorine peaks originate from the PFPDPA molecules at the Al_2O_3 surface. The surface NV-NMR technique is capable of providing chemical information from the SAM-functionalized Al_2O_3 surface with high sensitivity, much like XPS but under ambient conditions. The ^{19}F correlation spectroscopy data provides a time domain NMR signal (4.2 C), clearly showing an oscillation at the ^{19}F Larmor frequency that decays. The Fourier transform of these data results in the ^{19}F NMR spectrum with a resonance at 1.247 MHz, which agrees with the theoretical Larmor frequency at 31 mT (details can be found in Materials and Methods). Similarly, we can detect the ^{31}P signal from the functionalized surface, which results in a peak at 3 MHz at 174 mT (Appendix A.1.8: Magnetic field sweep of ^{31}P signal). The signal is weaker since the number of spins per molecule and the gyromagnetic ratio are lower compared to ^{19}F. Both signals were taken from the same monolayer and laser spot. We note that other NMR-active nuclei are present in this system, most notably^{27}Al and ^{1}H. However, the strong ^{13}C signals naturally occurring within the diamond is likely precluding the detection of the ^{27}Al resonance in the current experiment. This can be overcome in the future by using an isotopically enriched ^{12}C diamond. ^{1}H signal is ubiquitously observed on a clean diamond and cannot be unambiguously attributed to a characteristic of our system. Therefore, it has been excluded from the present analysis.

	T_2 (μs)	T_1 (ms)
clean diamond (n = 5)	5.59 $\pm$ 0.13	0.80 $\pm$ 0.28
After ALD (n = 8)	4.19 $\pm$ 0.24	0.73 $\pm$ 0.30

Table 4.1.: Influence of Al_2O_3 on NV center relaxation properties

4.3.4. Probing the Spatial Homogeneity of the Phosphonate Monolayer.

The spatial resolution (Fig. 4.2 C) is a considerable advantage of our technique which we utilized to probe the homogeneity of the phosphonate monolayer. The ^{19}F signal from the monolayer was measured in multiple areas within the MW loop and normalized to a constant reference signal generated by an external radiofrequency source, which allows the quantification of ^{19}F nuclei at each spot. It reveals gradient-like local differences rather than spot-by-spot differences, which may be caused by inhomogeneity in the ALD process (Fig. 4.3). Because of the microwave delivery, experiments can only be performed within the loop, whose position can be scanned together with the laser spot across the entire diamond. We avoid repositioning the loop because of possible scratching and damaging the SAM layer. This approach allows for correlating optical images with spatially resolved NMR signals.

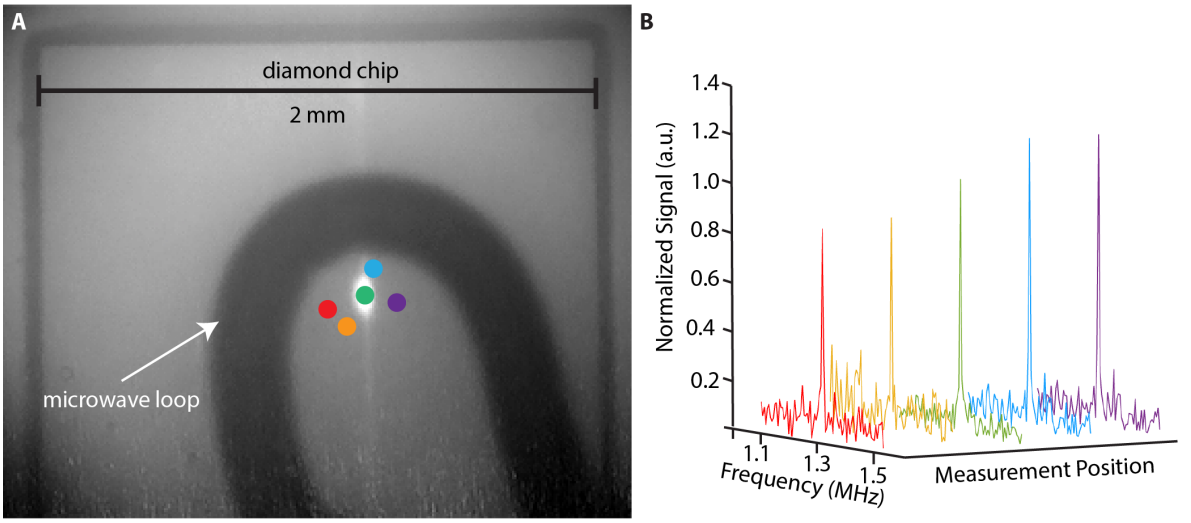

Figure 4.3.: **Probing the homogeneity of the phosphonate monolayer.** (A) Optical image of the diamond with marked measurement positions (color-coded,the laser spot for the green position is shown). The microwave loop for quantum control appears in black, the NV fluorescence of the excitation laser spot in white. (B) Normalized ^{19}F spectra of the different positions that are indicated in A.

4.3.5. Detection of Molecular Dynamics at the Surface.

From our measurement of the PFPDPA monolayer, a resonance linewidth of ∼3 kHz was observed, which is narrower than the linewidths observed in previous NV-NMR experiments of solid samples [7]. For that reason, we performed a second set of experiments in which the Al_2O_3 surface was functionalized with a shorter but perfluorinated PA molecule (1H,1H,2H,2H-peruoroctanephosphonic acid [PFOPA]) (Fig.4.4 A). The resonance linewidth is much broader (∼12 kHz) than for the case of the monolayer made from PFPDPA. In the solid state, the linewidth is typically limited by dipolar broadening, which can be minimized by local molecular dynamics such as rotations. The fluorinated phenolic moiety attached to a long carbon chain is more mobile than the ^{19}F nuclei in the perfluorinated chain of PFOPA, which likely reduces the linewidth [108, 109].

4.3.6. Spectroscopic Investigation for Binding of the Phosphonate Head Group to the Oxide Surface.

Following characterization of the phosphonate monolayer, we studied the molecular interaction between the phosphonate head group and the Al_2O_3surface. This was explored in a set of experiments in which the ^{31}P resonance linewidth was measured for a monolayer and on a drop cast sample on the diamond surface. Drop casting results in a random distribution of the molecules on the diamond surface with no chemical binding to the surface. The resonance linewidth of the monolayer (∼7 kHz) is significantly broader than for the drop cast molecules (∼3 kHz) (Fig. 4.4 B). In an additional set of experiments, we also monitored the linewidth of the ^{19}F signal, which broadened to a much lesser extent compared to the ^{31}P signal upon binding (Appendix A.1.9: Comparison of the linewidths of the ^{19}F and ^{31}P resonances). These results imply that the broadening effect is mainly on the phosphorus headgroup, indicating an interaction with the Al_2O_3 layer.

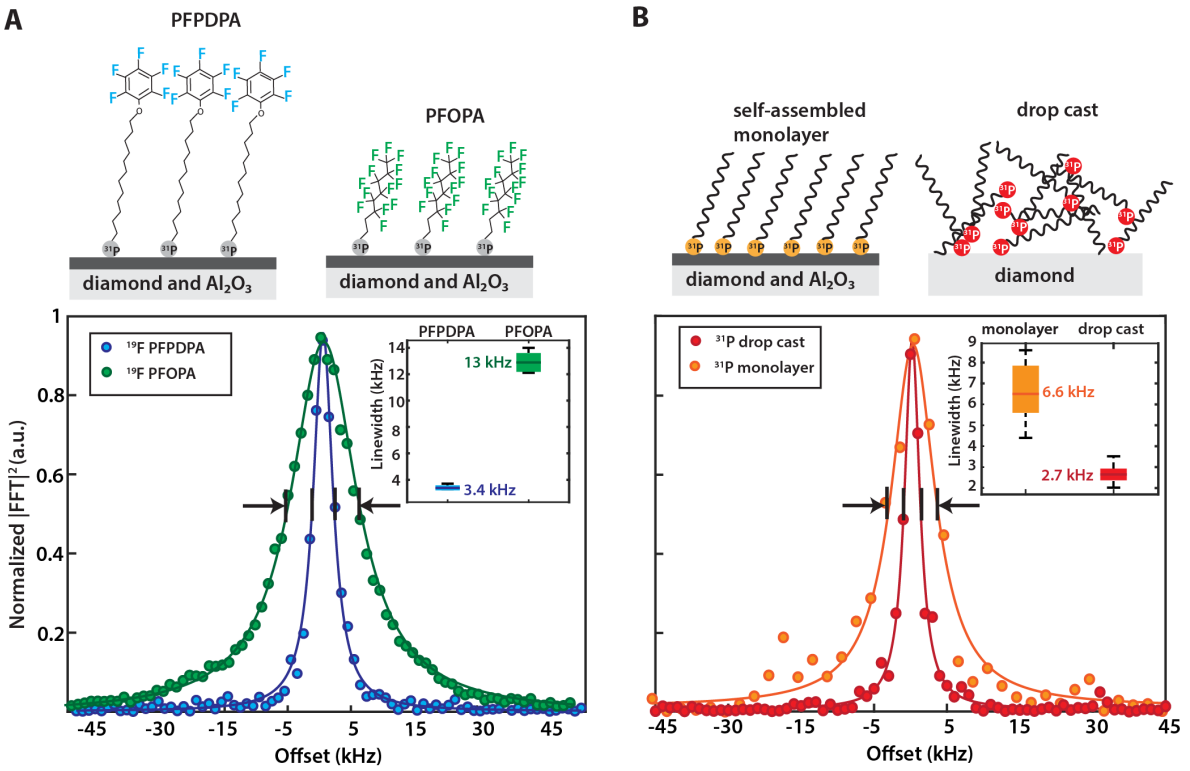

Figure 4.4.: **Spectroscopic characterization of the SAM layer.** (A) Influence of molecular structure on ^{19}F resonance linewidth. The ^{19}F linewidth of a monolayer made from PFOPA is approximately four times broader than that of PFPDPA. This is likely caused by local dynamics of the fluorinated phenolic moiety, which lead to line narrowing of the NMR signal. (Inset) Statistics over three experiments. The green and blue bars show one SD for the PFPDPA and PFOPA monolayers. The darker green and blue lines indicate the mean. The black lines are the minimum and maximum obtained linewidths. (B) Comparison of the ^{31}P linewidth for a SAM layer (Left) and a drop cast sample (Right). The ^{31}P linewidth in the case of a SAM layer is more than two times broader than that of the drop cast sample. (Inset) Statistics over eight repeated experiments. The orange and red bars show one SD for the monolayer and drop cast, respectively. The darker orange and red lines indicate the mean. The black lines are the minimum and maximum obtained linewidths.

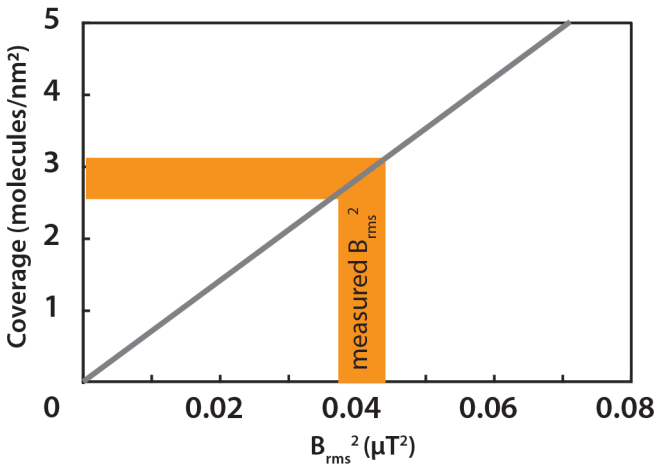

Figure 4.5.: **Quantification of the molecular coverage.** The gray curve shows the molecular coverage as a function of sensed fluctuating magnetic field (B^2_{rms}). Experimentally obtained B^2_{rms} of $\sim$0.04 μT^2 corresponds to a molecular coverage of $\sim$3 molecules/nm^2 shown in yellow shading for a monolayer.

4.3.7. Quantification of the Molecular Coverage.

An advantage of the quantum-sensing detection scheme is the facile quantification of the molecular coverage. The signal size (i.e., B^2_{rms}) is proportional to the spin density, which can be described by the following equation[110]:

$$B^2_{rms} = 5\pi/96(\mu_0 h\gamma_{nuc}/4\pi)^2\rho[1/d^3_{NV}\text{-}1/(d^3_{NV} + h^3_{spins}] \quad (1)$$

where $\mu_0 = 4\pi \times 10^7$ (m $\cdot$ T/A) is the vacuum permeability, h = 6.626 10^{34} (J $\cdot$ s) is the Planck constant, γ_{nuc} is the nuclear gyromagnetic ratio in MHz/T (40.05 MHz/T for ^{19}F), ρ is the nuclear spin density, h_{spins} is the thickness of the nuclear spin layer, and d_{NV} is the depth of the NVs. With a known NV depth distribution and defined sample geometry (Appendix A.1.5: SRIM simulation of ^{15}N implantation depth and A.1.10: Determining of the thickness of the organophosphate and Al_2O_3 surface), the equation correlates the measured signals (B^2_{rms}) to the spin density and the corresponding molecular coverage as shown in Fig. 4.5. With a reference signal, we calibrated our experiment and obtain 0.041 $\pm$ 0.003 μT^2 as the signal strength B^2_{rms} for the monolayer ^{19}F. This corresponds to a coverage of circa 3 molecules/nm^2

, which is in good agreement with a dense monolayer [65].

4.3.8. Monitoring Surface Chemistry in Real Time.

In contrast to other surface-sensitive techniques, surface NV-NMR allows for measurements under chemically relevant conditions, for example, at the solid–liquid interface. In the present case, this enables the observation of the binding of the phosphonate-anchoring group to the Al_2O_3 support at the solid/liquid interface depicted in Fig. 4.6 A. The chemical reaction kinetics were directly detected by the addition of PFPDPA solution onto a freshly prepared Al_2O_3 layer on a diamond and measurement of the surface NV-NMR signal as a function of time. Fig. 4.6 B shows individual surface NV-NMR spectra at different times after adding the PFPDPA solution. The ^{19}F resonance signal grows on a time scale of tens of minutes and plateaus after approximately half an hour. The broad resonance at 1.325 MHz next to the ^{19}F signal originates from ^{1}H, which is present from the beginning and is not characteristic of the surface chemistry. We repeated the experiment using solutions of different concentrations of the PFPDPA displaying an increase in the monolayer formation rate at higher concentration (Fig. 4.6 C). The kinetics of the ^{19}F signal can be modeled with an exponential growth function (Appendix A.1.11: Fitting parameters of the monolayer growth kinetics) [63, 111, 112]. As a reference, we repeated the experiment with a clean diamond without an Al_2O_3 layer. In this case, we did not observe a signal at the expected ^{19}F resonance, which indicates that the monolayer is inefficiently formed on diamond surfaces.

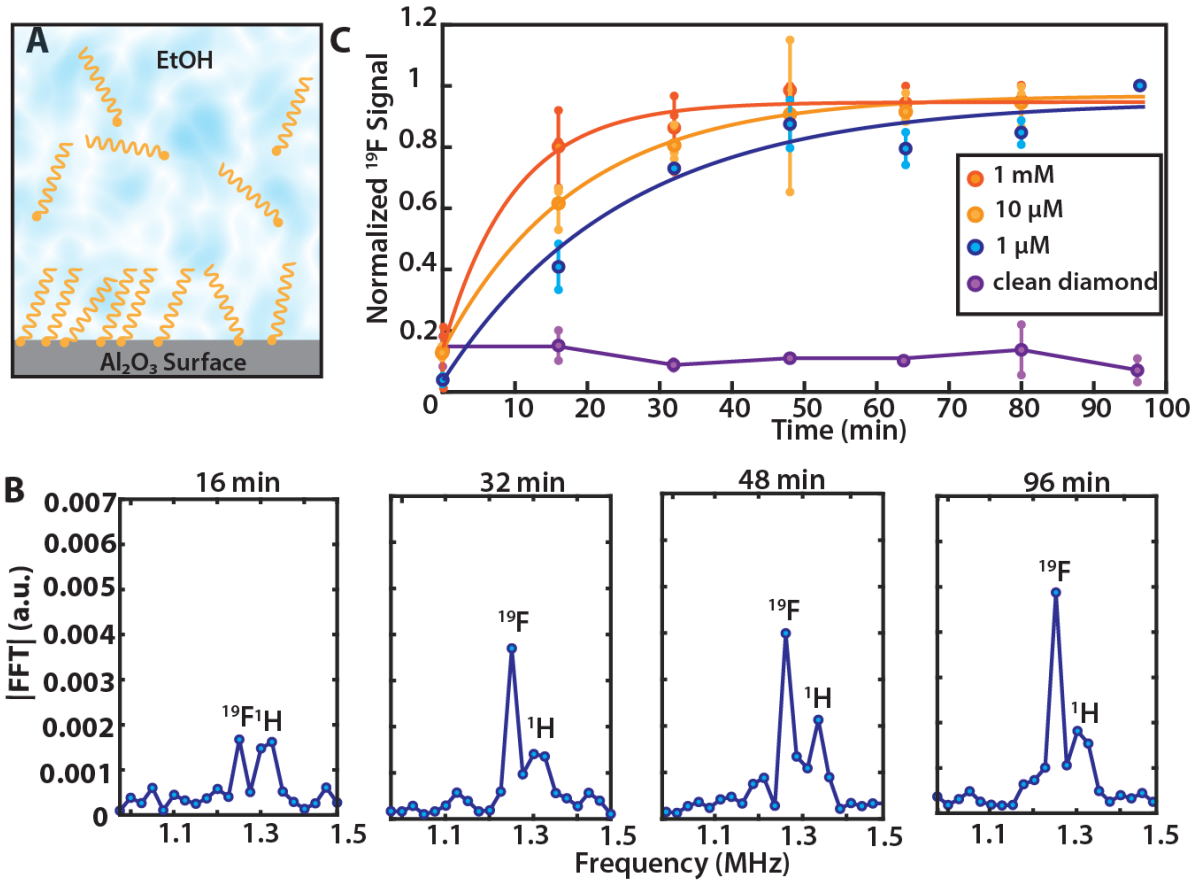

Figure 4.6.: Probing surface chemistry in situ. (A) Schematic of monolayer formation on Al_2O_3 in PA solution. (B) Individual spectra of ^{19}F showing the time evolution for a 1-μM solution. The peak around 1.35 MHz can be assigned to protons (^{1}H) which are known to be ubiquitous on or within the diamond and are not characteristic of the surface chemistry. (C) Real-time monitoring of the ^{19}F NMR signal amplitude growth in solution for three different PA concentrations shows a decrease in formation rate for lower concentrations. Small markers are measured data points of repeated experiments connected with a vertical line, averaged data are shown with the large points. Data points are fitted with a single exponential. Background signal of a clean, non- Al_2O_3–coated diamond in a 10-μM PA solution shows no ^{19}F signal. Note that due to the absolute value of the Fourier transformation, the noise floor is always positive.

4.4. Discussion

The surface NV-NMR technique has been successfully demonstrated to detect microscopic NMR signals down to submonolayer coverages, by observing real-time formation of molecular monolayer assembly on Al_2O_3. The use of a diamond-based sensor that is chemically inert and can withstand high temperatures and high pressures is advantageous, especially for chemical applications and catalysis. It will not only bridge the "pressure gap" in surface science but has the resilience to probe chemical reactions even under harsh conditions in situ [87]. Although this study used ALD-deposited Al_2O_3 this technique is not limited to this material. A variety of surfaces or thin films and its associated processes can be investigated ranging from lipid bilayers [113], two-dimensional (2D) materials [101], to metal organic frameworks and covalent organic frameworks as electrocatalysts in the form of thin films on conductive substrates [74].

Nevertheless, the technique is still in its infancy and has many possible avenues for improvement. The main challenge is the lack of molecular structural information due to dipolar broadening in the solid state that causes resonance linewidths on the order of a few kilohertz. Such a problem is well known in the field of solid-state NMR and has been solved by spinning the sample at the magic angle. Such a solution may be adopted for NV-NMR too, although with significant engineering challenges [114]. Alternatives are decoupling pulse sequences, which reduce sensitivity and cannot fully recover high-resolution spectra [7]. In order to resolve chemical shifts, the magnetic field B_0 must be increased up to $\sim$1 Tesla, which is feasible but technically demanding due to Q-band microwave electronics. Another approach is to utilize quadrupolar nuclei such as ^{14}N, ^{2}D, etc., which have been shown to convey detailed structural information despite their broad lines, making them ideal targets for surface NV-NMR at low fields [109].

Although the sensitivity did not limit this study, future analysis with faster temporal resolution of reaction kinetics or the detection of nuclei with low gyromagnetic ratios would benefit from further improvement. Advanced NV generation techniques [34, 38] or the growth of

preferentially orientated NV centers [115] can significantly improve the sensitivity. Additionally, an improved readout scheme of the NV quantum state has been shown to increase the sensitivity for single NV centers over an order of magnitude [99]. Finally, it should be noted that NV centers are strongly influenced by magnetic noise. Consequently, paramagnetic samples will deteriorate the NV coherence times and preclude surface NV-NMR studies of this type. However, other quantum-sensing schemes are available to study these types of materials [116].

In summary, the results from this study demonstrate the use of NV centers in a surface-sensitive and spatially resolved magnetic resonance technique for probing the chemical composition, binding to surfaces, and quantifying molecular coverage. Moreover, it can monitor chemical reactions in real time at the solid–liquid interface. In contrast to other surface analysis techniques, signals can be detected under chemically relevant conditions quantitatively in a low-cost experimental setup [30]. We are convinced that this presented technique will facilitate further understanding and probing of a variety of surface phenomena and materials. Not only does this method offer the noninvasive benefit of NMR spectroscopy but its functionality under chemically relevant conditions and low technical complexity also makes it a practical and sensitive technique for advanced studies in important areas of catalysis, materials science, biological sensing, or 2D materials research.

4.5. Materials and Methods

4.5.1. Diamond Preparation.

An electronic grade diamond (natural ^{13}C abundance, Element Six) was implanted with ^{15}N at an energy of 2.5 keV with an off-axis tilt of 7° and with a fluence of $2 \times 10^{12}/cm^2$ by Innovion. Then, the implanted sample was annealed under vacuum in a home-built oven for over 32 h (Appendix, A.1.3) with a Tectra BORALECTRIC sample heater. The diamond was cleaned before every Al_2O_3 deposition with a triacid cleaning protocol involving equal parts boiling sulfuric, nitric, and perchloric acid according to Brown et al. [46].

4.5.2. Atomic Layer Deposition.

ALD was performed using a Veeco Fiji G2 system. Prior to deposition, the diamond surface was cleaned in situ by 5× 0.15 s cycles of ozone, which was generated via electrical discharge in O_2. For the deposition of Al_2O_3 thin films, the ozone-treated diamond substrates were sequentially exposed to trimethyl aluminum (TMA) (98-1955, STREM Chemicals) followed by H_2O at 200 ° C cyclically. Each ALD cycle followed the sequence: TMA pulse/Ar purge/H_2O pulse/Ar purge. This was repeated for 10 cycles to achieve a final thickness of $\sim$ 1 nm (nominal growth per cycle of 0.1 nm/cycle). To achieve a reproducible surface hydroxyl surface termination suitable for monolayer assembly by phosphonate chemistry, the sample was exposed to a remote oxygen plasma within the ALD system. In particular, the radiofrequency (13.64 MHz) inductively coupled plasma source of the Fiji G2 system was operated at 300 W for a total of 1 min exposure. For repeated use of diamond substrates, the Al_2O_3 was removed by soaking overnight in a 5 % NaOH solution (Appendix A.1.12: Diamond surface cleaning for redeposition of Al_2O_3) before the next ALD deposition.

4.5.3. Phosphonic Acid Surface Functionalization.

For the fully formed monolayer shown in Figures 4.2-4.4, the following procedure was used. After the ALD process, the diamond is immersed in a 10 mM solution of either 12-pentafluorophenoxydodecylphosphonic acid (CAS number 1049677–16-8, Sigma-Aldrich) or 1H,1H,2H,2H-Perfluorooctanephosphonic acid (CAS number 252237–40-4, Sigma-Aldrich) for 2 days to allow the monolayer formation to equilibrate. Then, the diamond is sonicated for 5 min in ethanol to remove all physisorbed molecules, afterwhich the sample was dried with flowing nitrogen.

4.5.4. Surface NV-NMR Setup.

This NV-NMR setup has been previously described in detail in Bucher et al. [30].

Diamond alignment and optical approach.

The diamond was flatly positioned in the center of two neodymium magnets. These magnets were secured to rotation stages, the larger of which (RPO3M, Thorlabs) rotates the magnets to the orientation of the diamond. The smaller rotation stage (RP005M, Thorlabs) tilts the magnets in the direction of the NV-centers. This allows for alignment of the B_0 field along one of the four possible NV-center orientations. The diamond was glued on one side to a 12 mm thin round glass slide (89015-725, VWR) and a 6 mm glass hemisphere (TECHSPEC® N-BK7 Half-Ball Lenses, Edmund Optics) was glued to the other side, allowing for a total internal reflection geometry. This assembly was glued to a 30 mm cage plate (CP4S, Thorlabs) and fixed onto the experiment 1.2 cm above the top condenser lens (ACL25416U-B, Thorlabs).

Collection of Photoluminescence.

The photoluminescence (PL) from the NV-centers was collimated by condenser lenses, the bottom one aligned directly above a large area avalanche photodiode (ACUBE-S3000-10, Laser Components GmbH) that was positioned below the diamond. A long-pass filter (Edge Basic 647 Long Wave Pass, Semrock) was placed immediately between the bottom condenser lens and the photodiode to filter out non-NV PL wavelengths. The photo-voltage from the photodiode was digitized with a data acquisition unit (USB-6229 DAQ, National Instruments) and transferred to the computer.

Quantum state initialization and control.

A 532 nm laser (Verdi G5, Coherent) beam was controlled by an acousto-optic modulator (Gooch and Housego, model 3260-220) to pulse the NV-centers with 5 μs pulses of the laser. The laser power after the AOM was $\sim$ 400 mW when the AOM is fully on. A half-wave plate (AQWP05M-600, Thorlabs) polarized the laser beam in the direction of the NV-centers to maximize contrast. The laser beam was focused onto the diamond using a 125 mm focusing lens (LA1986-A-M, Thorlabs). Microwave frequencies from a signal source (SynthHD, Windfreak Technologies, LLC., New Port Richey) were phase shifted (ZX10Q-2-27-S+, Mini-Circuits) and controlled by switches (ZASWA-2-50dRA+, Mini-Circuits) to generate X and Y pulses. These pulses were then combined (ZX10-2-442-s+) and amplified by a microwave amplifier (ZHL-16W-72+, Mini-Circuits), and delivered to the diamond through

a small homemade loop. The electron spin resonance (ESR) frequency measured from the dip in PL was used to determine the NV resonance frequency at which to perform a Rabi experiment. The Rabi experiment (during which the duration of microwave pulses were swept from 0 to 200 ns) then determined the $\pi/2$ and π pulse durations for the correlation spectroscopy pulse sequences in which the contrast reached the midpoint and the minimum respectively. The magnetic field strength B_0 can be adjusted by changing the distance between the magnets to tune the nuclei Larmor frequency to that which is suitable for correlation spectroscopy. The correlation spectroscopy sequence has the highest performance for sensing frequencies between ∼1-4 MHz because of the T_2 relaxation time of the NVs and the finite π pulse durations. Therefore, we detect ^{19}F (∼1.2 MHz) at 31 mT ^{31}P (∼3 MHz) at 174 mT.

4.5.5. Surface NV-NMR and Sensitivity Estimate.

Correlation spectroscopy was performed using XY8-4 blocks (a total of 32 π pulses) with t_{corr} swept starting from 2 μs to obtain the spectra. For ^{19}F detection, t_{corr} was swept until 160 μs in 801 points. The time domain data were then Fourier transformed and the absolute value plotted using MATLAB. Each spectrum shown in Fig. 4.2 C is zero filled with 801 points. For the ^{19}F signal shown in Fig. 4.2 C, we obtain an SNR of 95 as calculated by dividing the signal value by the SD of the noise floor within a region without signal. For our laser spot area of 4,000 μm^2 and a monolayer coverage of 15 ^{19}F spins/nm^2, we obtain for 6 × 1010 (100 femtomoles) ^{19}F spins an SNR of 2.5 after 1 s integration. For ^{31}P detection, t_{corr} was swept until 80 μs in 801 points. The ^{31}P signal was averaged twice to obtain an SNR of 15. The ^{19}F and ^{31}P NMR signals were obtained in 25 and 32 min, respectively. For linewidth measurements as shown in Fig. 4 A and B, each monolayer ^{31}P signal was measured to 2,501 points, and t_{corr} swept to 0.25 ms, and each spectrum averaged 10 times (20 h) and zero filled to 5,001 points. For each drop cast measurement, the ^{31}P signal was measured to 5,001 points, and t_{corr} swept to 0.5 ms and zero filled to 10,001 points. The ^{19}F signals for the linewidths were measured to 2,501 points, t_{corr} swept to 0.5 ms and zero filled to 5,001 points (45 min). After zero filling, each fast Fourier transform (FFT) power spectrum ($|FFT|^2$) is plotted, and

the linewidth of the resonance is fit with a Lorentzian model [105]. For the homogeneity study, the t_{corr} was swept until 160 μs in 801 points again to obtain the ^{19}F signal with only one average (25 min). For the 1-MHz reference signal the t_{corr} was swept until 80 μs in 401 points.

4.5.6. Imaging of Diamond and Laser Spot.

The laser spots for the homogeneity study shown in Fig. 4.3 were imaged using a Basler a2A1920-160umBAS camera. The signal was normalized with a 1-MHz reference signal generated with an arbitrary waveform generator (DG 1032, Rigol), amplified (LZY-22+, Mini-Circuits), and then delivered through a wound coil fixed close to the diamond. The t_{corr} was swept until 80 μs in 401 points to obtain the reference signal. The described procedure was manually performed as a proof of principle but can be converted to a systematic scan of the surface by simply motorizing the optics with standard piezo components to obtain microscale control of the laser spot position.

4.5.7. Determining the Molecular Coverage.

To simulate spin noise, we use an oscillating magnetic field with tunable strength. This signal is generated with an arbitrary waveform generator (DG 1032, Rigol) and amplified (LZY-22+, Mini- Circuits) and then delivered through a large wound coil fixed close to the diamond. The NMR signal from the monolayer can be calibrated by comparing it to this reference signal to determine the B^2_{rms} [117]. A simple model was set up to quantify the molecular coverage of the SAM layer from the signal size measured in the experiments. The alkyl chain length = 1.5 nm was added to the NV depth d_{NV}, and h_{spins} = 0.5 nm was considered to be the thickness of the layer with nuclear spins (fluorinated benzene ring). The sensed fluctuating magnetic field (B^2_{rms}) corresponding to different nuclear spin densities was calculated applying Eq. 1 and the value weighted according to a Gaussian probability function utilizing d_{NV} = 4.5 nm and σ = 1.9 nm as mean and SD. These values were obtained from the SRIM simulation as reported in Appendix A.1.6 [35]. The nuclear spin density ρ was multiplied by the thickness

of the spin layer h_{spins}, converting it to a coverage (spins/nm^2), and then divided by the number of fluorine spins in each molecule, obtaining the final molecular coverage as in the curve reported in Fig. 4.5.

4.5.8. In Situ Kinetics of Monolayer Formation.

The triacid-cleaned diamond was first coated with 1 nm Al_2O_3 and activated with oxygen plasma as described in Atomic Layer Deposition. Subsequently, the diamond was glued down to a watertight liquid sample holder made from a 30-mm cage plate (CP4S, Thorlabs) with a thin round cover slide (100493678, VWR) glued to the bottomand the top fitted with a threaded lens tube (SM30L03, Thorlabs). The cage plate was then mounted to the surface NV-NMR experiment. ^{19}F is detected with 24 time traces, which were continuously acquired by sweeping t_{corr} to 40 μs with 201 points. Each data point in Fig. 4.6 B was an average of four time traces, which were then Fourier transformed and the ^{19}F signal amplitude plotted, resulting in six points for the kinetic dataset. Each of these experiments are repeated three times (1 mM, 10 μM) and two times (1 μM), and the signal amplitudes are averaged and then fit. Each time trace is normalized to 1 for the time point at 96 min. The first point at t = 0 min is set to the mean of the noise floor of the Fourier-transformed spectra. The background signal is the value at the ^{19}F frequency within spectra obtained with a clean diamond measured in the intermediate concentration 10-μM solution. As there is no ^{19}F, the background data are normalized to the final ^{19}F signal of a 10-μM growth kinetics data set.

4.5.9. Static Water Contact Angle Measurements.

SWCA measurements were performed on an OCA 15Pro contact angle system (DataPhysics Instruments). Data acquisition and evaluation were realized with SWCA 20—contact angle (DataPhysics Instruments, version 2.0). For quantifying an average Young's contact angle ($\theta\gamma$), 2 μL deionized H_2O (18.2 M Ωcm at 25 °C, Merck Millipore) was dispensed with a rate of 0.2 μL/s from a 500-μL Hamilton syringe onto the sample surface. After allowing the droplet to settle for $\sim$3 s, an image was acquired for further processing. The procedure was repeated at

least three times on different spots on the surface, and the SD was calculated.

4.5.10. Atomic Force Microscopy.

A MultiMode 8 (Bruker Corp.) was used in tapping mode and in contact mode under ambient conditions using NSG30 (TipsNano) for standard characterization and to estimate the Al_2O_3 layer thickness. Scratching in contact mode was performed over areas of 1×1 μm^2 with a deflection set point of 5 V. Amplitude modulation (tapping mode) AFM was done with an amplitude set point of 0.3 V (at a free amplitude of 0.5 V). The surface roughness was evaluated via the RMS average of height deviations taken from the mean image data plane of 2×2 μm^2 tapping mode micrographs. The roughness and step heightswere analyzed using Gwyddion 2.56.

4.5.11. X-ray Photoelectron Spectroscopy.

XPS measurements were performed with an Axis Supra (Kratos) spectrometer. The monochromatized Al $\kappa\alpha$ (1486.9 eV) X-ray tube source was operated at an emission current of 15 mA. The data were recorded with a circular acceptance area of Al source, and the analyzed area was 700×300 μm in diameter. Spectra were processed with CasaXPS (Casa Software Ltd, version 2.3.17).

5. Using metal-organic frameworks to confine liquid samples for nanoscale NV-NMR

This chapter is adapted from a paper submitted to ACS Nano Letters.

By Kristina S. Liu, Xiaoxin Ma, Roberto Rizzato, A. Lisa Semrau, Alex Henning, Ian D. Sharp, Roland A. Fischer, Dominik B. Bucher

Author contributions:

K.S.L. and X.M. contributed equally to this work. D.B.B. conceived the idea of a confined NV-NMR method, designed the experiments and supervised the study. K.S.L. performed SCWA, Raman, NV-NMR experiments and ALD deposition. A.L.S. and X.M. performed surface modification. X.M. performed X.R.D. measurements and elemental analysis. A.H. performed AFM measurements. R.R., R.A.F. and I.D.S. advised on several aspects of theory and experiments. All authors discussed the results and contributed to the writing of the manuscript.

5.1. Synopsis

Atomic-scale magnetic field sensors based on nitrogen vacancy (NV) defects in diamonds are an exciting platform for nanoscale nuclear magnetic resonance (NMR) spectroscopy. The detection of NMR signals from a few zeptoliters to single molecules or even single nuclear spins has been demonstrated using NV-centers close to the diamond surface. However, fast molecular diffusion of sample molecules in and out of nanoscale detection volumes impedes

their detection and limits current experiments to solid-state or highly viscous samples. Here, we show that restricting diffusion by confinement enables nanoscale NMR spectroscopy of liquid samples. Our approach uses metal-organic frameworks (MOF) with angstrom-sized pores on a diamond chip to trap sample molecules near the NV-centers. This enables the detection of NMR signals from a liquid sample, which would not be detectable without confinement. These results set the route for nanoscale liquid-phase NMR with high spectral resolution.

5.2. Introduction

Despite the advantages described in Chapter 4, nanoscale NMR comes with its own challenges. The main drawback is that the time scale of diffusion of liquid samples across nanoscale detection volumes limits the interaction of the samples with the NV-sensor, which leads to broadened signals for viscous samples and to undetectable signals for low viscosity liquid samples [7, 49, 67, 118, 119]. Within sensing volumes, liquid-state molecules can diffuse in and out because of Brownian motion (Fig. 5.1 A, left). For illustrative purposes, one can visualize the effect that molecular diffusion has on the nuclear spin signal by simulating a random walk of a molecule at a certain distance from the NV center, with its molecular mobility physically restricted by the presence of the diamond surface. Then, following the approach in Pham et al.[66], the coupling factor $c = \frac{u_z^2(1-u_z^2)}{r^6}$ can be calculated, where r is the length of the vector connecting the NV center and the molecule and u_z contains the angular terms in spherical coordinates. This coupling factor estimates how strongly the target nucleus interacts with the NV sensor at a certain time point within the experimental timescale. The decay of this value over time, caused by the average distance of the molecules from the NV center over time, ultimately results in the expected NV-NMR linewidth.

Here, two different exemplary conditions for molecular mobility can be envisioned, as represented in Figure 5.1 B. With a diffusion coefficient of D = 5×10^{-10} m^2/s (ten times

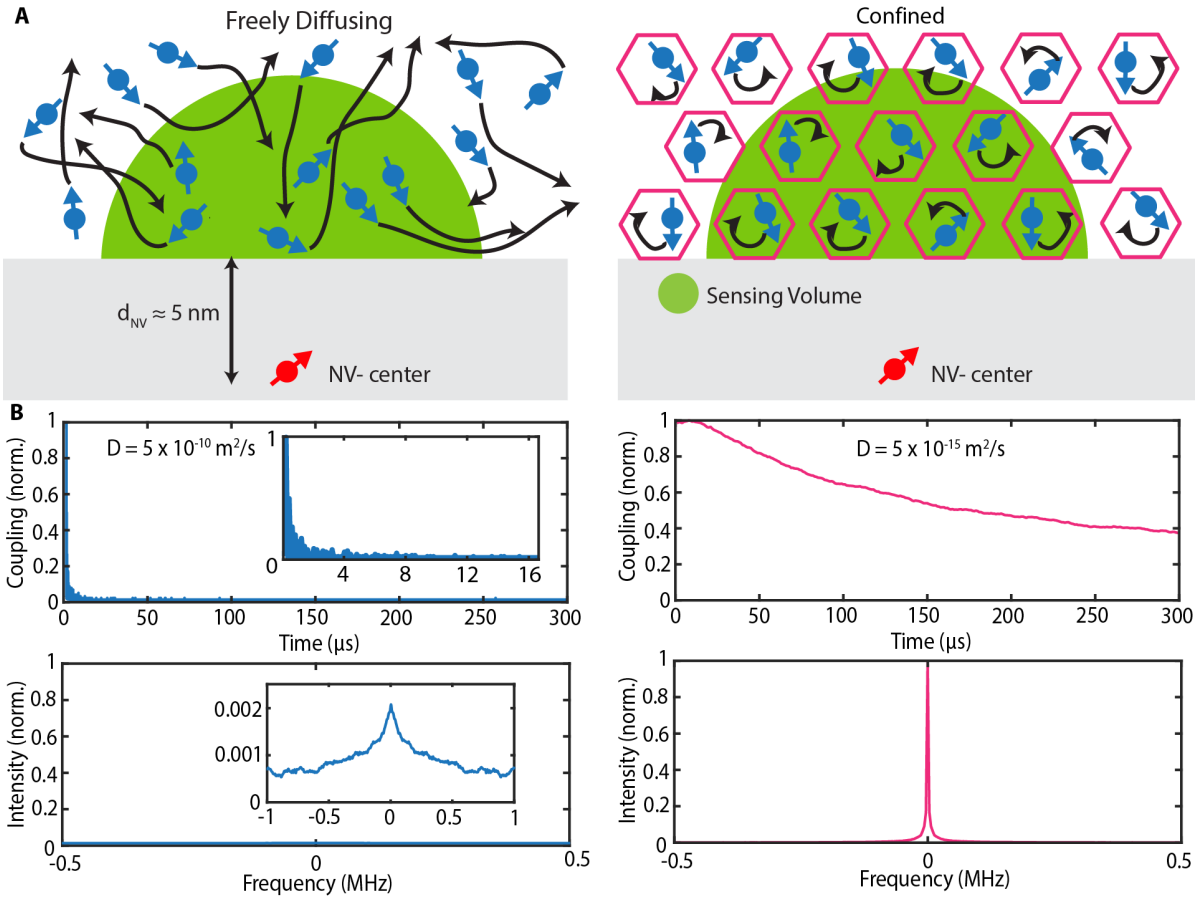

Figure 5.1.: **Confinement of liquid samples for nanoscale NV-NMR spectroscopy.** A) Schematic of nanoscale NV-NMR with liquid samples. Freely diffusing (blue) nuclei enter and leave the sensing volume (green) of the NV-centers while those confined (magenta) stay within the sensing volume. B) Fast diffusion limits the interaction time with the NV-center and causes a fast decay of the NMR signal (left), leading to severely broadened lines that are typically not detectable. Confinement of the spins (right) results in a long-lived NMR signal, enables its detection and opens a way to high spectral resolution nanoscale NV-NMR spectroscopy.

lower than water), the probability of a molecule free to move in the vicinity of the diamond remaining within the sensing volume of the NV center drops off rapidly in time (Fig. 5.1, left). This has a dramatic impact on the NV-based NMR sensing, yielding signals that are too broad to be detected experimentally. For a slow diffusion coefficient of D = $5{\times}10^{-15}$ m^2/s (Fig. 5.1 C, right) a much narrower linewidth is expected, allowing for a detectable signal. Consequently, the restriction of diffusion, while keeping the sample in the liquid state to avoid dipolar broadening, is crucially important for NV-NMR. Prior theoretical work raised a compelling possibility for counteracting the effects of diffusion by confinement of liquid samples in small volumes, thereby enabling this major impediment to nanoscale NMR to be overcome[67]. An intriguing system for achieving such confinement is based on metal-organic frameworks (MOFs), which are porous materials with high surface areas [120, 121]. Furthermore, the CoRE MOF database contains thousands of different MOFs with various physical and chemical properties, including different and precisely defined pore sizes [122]. This powerful capability enables specific MOFs to be rapidly identified that have suitable pore sizes and flexibility to efficiently impede diffusion by trapping small sample molecules [122]. In the present work, we selected the MOF UiO-66, which has been computationally identified for capturing ^{31}P containing small molecules, resulting in slow diffusion coefficients [73]. This material can also be grown as a surface-anchored MOF, or "SURMOF", with well-ordered nanocrystals, achieving film thicknesses of less than 100 nm [74, 123–126]. When grown on a NV-diamond, this UiO-66 SURMOF can realize the confinement of liquid-state nuclei within the nanoscale detection volumes of the NV-quantum sensors. Therefore here, we modify the diamond surface with thin films of UiO-66, which enabled us to observe ^{31}P NMR signals from the small phosphorous-containing molecule trimethyl phosphate (TMP). The size of TMP is comparable to those of other molecules that have been described by Agrawal et al. [73] as having very low diffusion coefficients in UiO-66, but with low toxicity. This proof-of-concept study can be generalized to the detection of a wide array of small molecules and sets the route to the detection of liquid-state samples using nanoscale NMR.

5.3. Results

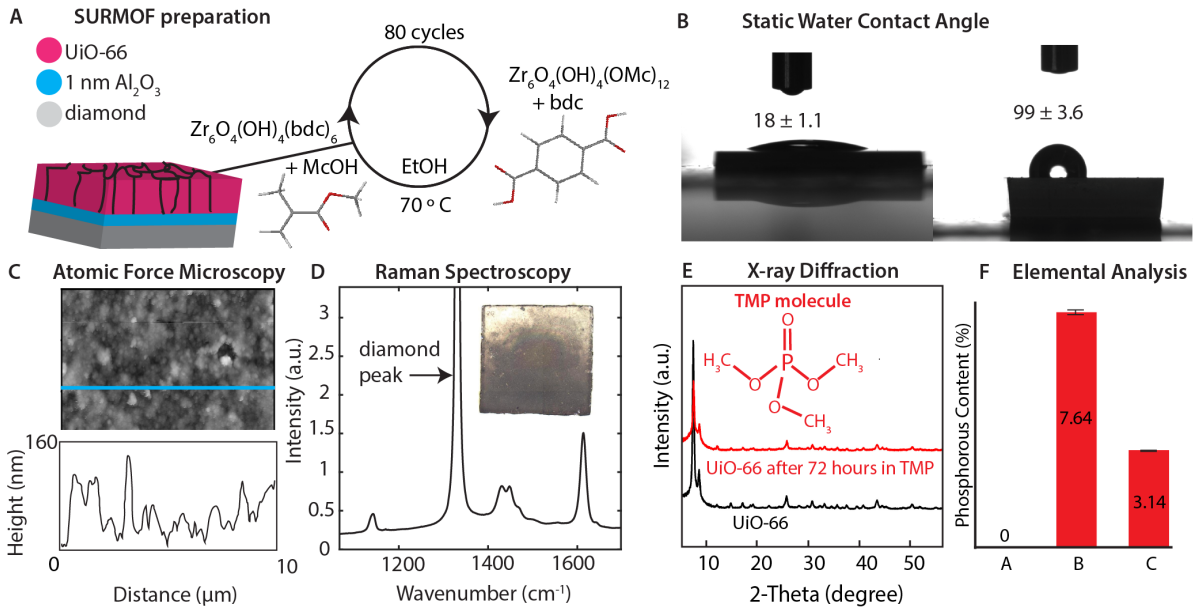

Figure 5.2.: A) Left: Schematic of the functionalized diamond chip with 1 nm of Al_2O_3 grown by ALD and ∼80 nm of UiO-66 grown by SURMOF (not to scale). Right: chemical process for functionalization of the diamond surface with UiO-66 SURMOF. B) Top: Static water contact angle measurements show the transformation of the hydrophilic Al_2O_3-terminated diamond to a hydrophobic surface following deposition of UiO-66. C) Height profile analysis of atomic force microscopy images yields an average MOF film thickness of 85 nm D) Raman spectroscopy of the diamond chip functionalized with UiO-66 SURMOF reveals clear modes from the MOF, with peaks at: 1141 cm−1 and 1614 cm−1, along with a doublet at 1441 cm−1. The strong peak at 1332 cm−1 corresponds to the zone center optical phonon of diamond. Inset: optical microscope image of the functionalized diamond with a size of 2×2 mm^2. E) X-ray diffraction of UiO-66 powder still contains distinctive peaks after soaking in trimethyl phosphate for 72 h. Inset: Illustration of the TMP molecule structure. F) Elemental analysis shows no phosphorous in UiO-66 powder (Sample A) but 7.64 ± 0.1 % of phosphorous after soaking in TMP (Sample B), and 3.14 ± 0.01 % after soaking in TMP and washing (Sample C).

5.3.1. Functionalizing diamond with UiO-66 SURMOF.

In order to restrict diffusion within the NV-detection volume, we functionalized the diamond surface with a thin layer (SURMOF) of UiO-66, which is a MOF with $Zr_6O_4(OH)_4$ nodes linked by 1,4-benzene-dicarboxylate (bdc). The UiO-66 ($Zr_6O_4(OH)_4(bdc)_6$) was formed via

coordination modulation-controlled step-by-step liquid-phase growth (Fig. 2 A)25. We chose to facilitate adhesion of the SURMOF by coating the diamond surface with a 1 nm thick layer of alumina (Al_2O_3) via atomic layer deposition (ALD) [127, 128]. The alumina film is hydrophilic, as indicated by the relatively low static water contact angle (SWCA) of $18^\circ \pm 1.1^\circ$ (Fig. 5.2 B), whereas the SURMOF surface is hydrophobic with an SWCA of $99^\circ \pm 3.6^\circ$. This is expected because the bdc linkers are poorly soluble in water (Fig. 5.2 B). Following 80 cycles of the liquid-phase MOF deposition yields a discontinuous film showing miniscule cracks on a micrometer scale and with an average thickness of $\sim$85 nm (Fig. 2C). This is consistent with previous results from growth on a silicon dioxide surface [124]. The SURMOF on the diamond chip was then characterized by Raman spectroscopy, revealing known UiO-66 peaks in addition to a large diamond peak (Fig. 5.2 D) [129]. From these results, successful formation of a thin film of UiO-66 is confirmed.

5.3.2. Characterization of SURMOF stability in and trapping of TMP within MOF pores.

Comparison of X-ray diffraction data obtained before and after soaking UiO-66 in trimethyl phosphate (TMP) confirms the stability of the MOF in solution (Fig. 5.2 E). This indicates that the SURMOF remains intact during the process applied to fill the MOF pores with TMP, which was accomplished via soaking in TMP overnight. TMP is soluble in H_2O, which we take advantage of to verify that the NV-detected NMR signal comes from within the pores using elemental analysis, as follows (Fig. 5.2 F). As expected, within the detection limit, the pure UiO-66 MOF powder contains no phosphorous F, condition A). After soaking the MOF in TMP for 2 days and filtering directly afterwards, the P content is $\sim$7.6 wt. % (condition B), which decreases to $\sim$3.2 wt. % after careful washing in H_2O before filtering (condition C). The decrease of phosphorous content is likely due to removal of TMP from the surface of the MOF. This result suggests that the remaining phosphorous content is within the pores, which verifies the absorption of TMP by the MOF. Quantification of the elemental analysis indicates a molar ratio of 1:2 of UiO-66 MOF to TMP (see Appendix A.2.1: Elemental analysis of TMP

and UiO-66 MOF powder). Pore volumes for UiO-66 have been reported to be ~ 0.5 cm^3/g [130–132] (see Appendix A.2.2: Estimation of pore filling from elemental analysis). From this we can estimate that the MOF contains approximately $1.9{\times}10^{24}$ pores/mol of MOF and that $\sim 64\%$ of these available pores are filled, meaning that TMP is well-absorbed by the MOF.

5.3.3. Detecting NV-NMR-signals from small molecules trapped within SURMOF pores.

After functionalization, NV-NMR at 174 mT was performed on a shallowly implanted diamond (Appendix A.2.3: Experimental Conditions) to detect ^{31}P NMR signal from neat TMP. We observe that the Al_2O_3-terminated diamond soaked in TMP shows no detectable ^{31}P signal (Fig. 5.3 A, left). Freely diffusing TMP molecules with Brownian motion on that order would produce an undetectable signal due to extremely broadened lines (Fig. 5.1 B). Diffusion-ordered NMR spectroscopy (DOSY) measurements of TMP in D_2O revealed a diffusion constant of $\sim 6{\times}10^{-10}$ m^2/s (see Appendix A.2.4: Diffusion-ordered NMR Spectroscopy of Trimethyl Phosphate). In contrast to the fast diffusion of free TMP, slow diffusion due to confinement or adsorption within the pores is expected [73]. UiO-66 has two different types of pores, one with a size of 11 Å, called the primary pore, and a smaller one with a size of 7.2 Å, called the secondary pore. Each primary pore is connected to a secondary pore through a window of diameter 4.5 Å(Fig. 5.3 B). Due to the low molecular stiffness of UiO-66, physical hopping between pores is greatly slowed down for molecules that are larger than the window, which consequently strongly reduces the diffusivity [73].

Upon growing SURMOF on the oxide surface and filling the pores with TMP, we observe a narrow NV-NMR signal at 5.3 A, right). After rinsing and soaking the MOF-terminated diamond in H_2O and then drying with nitrogen, the ^{31}P signal is still present (see Appendix A.2.5: Measuring ^{31}P signal from dried MOF). This further indicates that the ^{31}P signal arises from TMP within the pores since TMP is soluble in water and non-incorporated molecules would be readily cleaned from the surface of the MOF. Due to limited SNR, we are unable to completely resolve the linewidth (the spectrum shown has been zero-filled). However, we

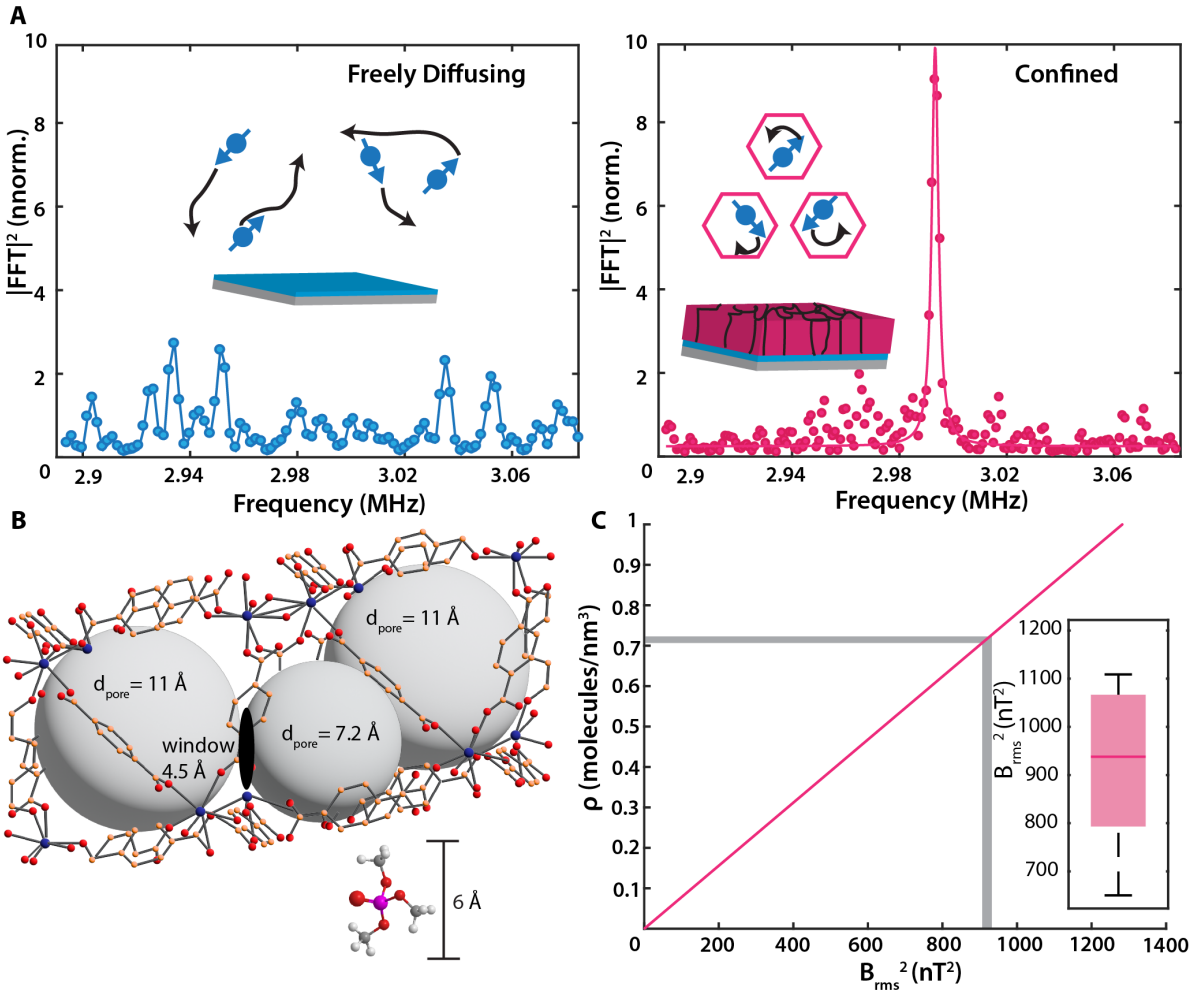

Figure 5.3.: A) Left: Reference experiment on a Al_2O_3 functionalized diamond. No NMR signal can be detected due to fast diffusion of the TMP molecule. Right: The ^{31}P-NMR signal from TMP measured by NV-NMR shows a narrow signal. Data is normalized to a reference signal. B) UiO-66 with pore sizes shown as spheres and windows connecting the pores. Adapted with permission from Agrawal, M. et al., J. Phys. Chem. Lett. 10, 7823–7830 (2019) Copyright 2019 American Chemical Society. A trimethyl phosphate (TMP) molecule with a size of approximately 6 Åcan be confined within these pores, restricting its diffusion above the NV-centers. C) The magenta line shows the density of molecules as a function of sensed fluctuating magnetic field (B^2_{rms}) and the standard deviation is shown using the thicknesses of the grey lines. Inset: statistics of ^{31}P signal strength B^2_{rms} is determined (n = 4). The magenta line shows the mean, while the box shows the upper and lower quartiles. Black lines show minimum and maximum values.

can claim an upper limit of $\sim$ 3 kHz which is set by the specific t_{corr} of the correlation measurement [105]. Importantly, this ^{31}P signal and associated linewidth is obtained exclusively from the MOF-terminated diamond, whereas no signal is detectable from freely diffusing TMP. We note that the data for both the MOF- and Al_2O_3-terminated surfaces soaked in TMP, as shown in Figure 5.3 A, are normalized to the reference signal (see Appendix A.2.6: Signal normalization using a 1 MHz reference signal).

The number of molecules within the detection volume can also be quantified by measuring the spin noise (B^2_{rms}) using this 1 MHz reference signal. The calibrated strength of the ^{31}P signal from TMP is determined to be $\sim$ 920 nT^2 (Fig. 5.3 C). From this, we can estimate a density of TMP molecules trapped within the MOF pores using the equation [110]:

$$B^2_{rms} = \frac{5\pi}{96}(\mu_0 h\gamma_{nuc}/4\pi)^2\rho[1/d^3_{NV}\text{-}1/(d^3_{NV} + h^3_{spins}] \quad (1)$$

where $\mu_0 = 4\pi \times 10^7$ (m $\cdot$ T/A) is the vacuum permeability, h = 6.626 10^{34} (J $\cdot$ s) is the Planck constant, γ_{nuc} is the nuclear gyromagnetic ratio in MHz/T (17.235 MHz/T for ^{31}P), ρ is the nuclear spin density, d_{NV} is the depth of the shallow NV-centers, and h_{spins} is the thickness of the nuclear spin layer. Using the 85 nm average height of the MOF layer as the thickness and the simulated average NV depth of 4.5 nm [35, 127] with an additional 1 nm from the Al_2O_3 deposited on the surface, we estimate that $\sim$ 700 TMP molecules are trapped in each (10nm)^3. This calibration result is comparable to 530/(10nm)^3, the density of molecules calculated from the molar ratio determined from elemental analysis (see Appendix A.2.8: Calculation of TMP density within UiO-66 SURMOF pores from Elemental Analysis).

5.4. Conclusion

In summary, we show that restricting diffusion by confinement enables nanoscale NMR spectroscopy of liquid samples. Our approach uses MOFs with angstrom-sized pores on the surface of a NV-diamond chip to trap sample molecules near the NV-centers. This enables us to detect NMR signals from a liquid sample, which would not be detectable

without confinement. We obtain the ^{31}P signal from TMP trapped within the pores of UiO-66 grown as a thin layer on the diamond. Our results pave the way towards nanoscale liquid-state NMR with high spectral resolution. A great advantage of MOFs is that due to their reticular synthesis they can be tailor-made to have various physical and chemical properties, including pores of desired sizes, chemical compositions that do not interfere with molecules from the solution, and stabilities under different environments[68, 133]. This method is therefore broadly usable for enrichment, colocalization and trapping of sample molecules near the NV-center for molecular analysis on a single molecule level[99] or NV-based hyperpolarization[134].

5.5. Material and Methods

Diamond preparation, NV-NMR setup, SWCA and ALD has already been described in the Material and Methods section of chapter 4.

5.5.1. Synthesis of cluster-$[Zr_6O_4(OH)_4(OMc)_{12}]$ and fabrication of UiO-66 thin-films (SURMOFs).

The $Zr_6O_4(OH)_4(OMc)_{12}]$ (OMc = Methacrylate) was synthesized using the previously described procedure [124]. In detail, 70 Wt.% $Zr(OnPr)_4$ in n-propanol (3.1 mmol, Sigma-Aldrich,) was combined with 1 mL of methacrylic acid (11.8 mmol, McOH, Sigma-Aldrich,) in a flask under Argon at room temperature. After two weeks, the colourless crystals were collected after cleaning with n-propanol (Sigma-Aldrich). The $[Zr_6O_4(OH)_4(OMc)_{12}]$ cluster could be obtained after drying at 80 °C overnight. The diamond (2×2 mm^2) was placed in a double-walled reaction vessel after being exposed to ozone for 5 min. Prior to the experiment, a 0.5 mM $[Zr_6O_4(OH)_4(OMc)_{12}]$ ethanol solution (Solution 1) was mixed with 300 mM McOH, and the deprotonated organic linker solution (Solution 2) was made by combining 3mM terephthalic acid (H_2BDC,Sigma-Aldrich,), 1L ethanol (99.9 %, Th. Geyer GmbH & Co. KG, Germany), and 320 μL trimethylamine (Et_3N, Acros). The thin film deposition was carried

out through a layer-by-layer (LBL) method in a homemade pump system at 75 °C following a reported procedure [125]. The diamond substrate was initially soaked in Solution 1 for 10 min before being washed in pure ethanol for 2 min. The substrate was then maintained in solution 2 for 10 min before the first synthesis cycle was completed with a 2 min ethanol washing step. The process was repeated 80 times. LabView software was used to control operate of the pump system.

5.5.2. Emptying and filling SURMOF pores.

The diamond with UiO-66 SURMOF was glued to the assembly previously described above in NV-NMR Setup. The glue was cured overnight at 50 °C to ensure stability in trimethyl phosphate. The glued diamond assembly was placed in an oven at 80 °C overnight to empty the ethanol from the pores, after which the diamond was soaked overnight in trimethyl phosphate.

5.5.3. NV-NMR

Correlation spectroscopy was performed using XY8-4 blocks (a total of 32 π pulses) with t_{corr} swept starting from 2 µs to obtain the spectra. For ^{31}P detection t_{corr} was swept until 320 μs in 3201 points. The time domain data were then Fourier transformed and the absolute value plotted using MATLAB. For the ^{31}P signal shown in Fig. 5.3 A, we obtain a SNR of $\sim$12, as calculated by dividing the signal value by the standard deviation of the noise floor within a region without signal. This signal was obtained in 180 min. The spectrum shown is zero-filled with 10000 points (to 1 ms). After zero-filling, the power spectrum ($|\mathrm{FFT}|^2$) is plotted, and the linewidth of the resonance is fit with a Lorentzian model [105].

5.5.4. Atomic Force Microscopy.

A MultiMode 8 (Bruker Corp.) was used in tapping mode utilizing NSG30 (TipsNano) to estimate the UiO-66 SURMOF thickness. The thickness of the SURMOF was obtained from

the height profiles taken from the mean image data plane of 10 x 10 μm^2 tapping-mode micrographs. Images were analyzed using Gwyddion 2.56.

5.5.5. Preparation of UiO-66 powder and powder X-ray diffraction (PXRD).

0.159g $ZrCl_4$ (Alfa Aesar) was added to the 25ml N,N-Dimethylformamide (DMF, Sigma-Aldrich) with stirring at room temperature for 20 min. Then, 0.102g H_2BDC was adding to the aforementioned solution. After continuously stirring for 30 min, the homogenous solution was heated in an autoclave at 120 °C for 24 h. After centrifugation and DMF washing, the white powder was soaked in methanol liquid for 3 days for exchange with the DMF in the MOF pores. The UIO-66 powders were collected after centrifugation and dried in vacuo at 80 °C. Powder X-ray diffraction (PXRD) patterns were acquired using a Rigaku MiniFlex 600-C diffractometer with a Cu Kα irradiation source (λ = 1.54056 Å) and a scan speed of 10° per min.

6. Probing phase dependent diffusion of lipid bilayers using quantum sensors in diamond

This chapter is adapted from a manuscript in preparation.

By Kristina S. Liu, Stefanie D. Pritzl, Theobald Lohmüller, Dominik B. Bucher

Author contributions:

D.B.B. designed the experiments and supervised the study. K.S.L. performed SCWA and NV-NMR experiments. S.D.P performed FRAP measurements and prepared material for SPB formation. T.L advised on several aspects of theory and experiments. All authors discussed the results and contributed to the writing of the manuscript.

6.1. Synopsis

Nitrogen vacancy (NV) centers as quantum sensors in diamonds can perform nuclear magnetic resonance (NMR) spectroscopy with sufficient sensitivity to detect unique nuclei with nanoscale localization under ambient or biologically relevant conditions. These properties make it suitable for label-free direct probing of diffusion of systems as thin as bilayers, which is an essential process to understand within analogous biological systems such as the cell membrane. Here, supported phospholipid bilayers (SPB) of the phospholipid dipalmitoylphosphatidylcholine (DPPC) are used as a membrane model. Nanoscale NMR spectroscopy of ^{31}P nuclei in the gel phase and the fluid phase is measured. We observe a clear diffusional broadening of the ^{31}P signal from the gel phase to the fluid phase, correlating with faster diffusion. The results are compared with a commonly used fluorescence technique,

indicating that diamond is a support substrate that exhibit a slower diffusion of the bottom SPB layer.

6.2. Introduction

The cell membrane consists of a phospholipid bilayer, and its motion is involved in biological processes which move along with the membrane [135]. The functions within nanodomains (10-200 nm) of the membrane (including the transport of molecules or cell signaling) is related to the fluidity of these domains and is characterized by lateral diffusion, the translational diffusion along layers of phospholipids [136]. Therefore, understanding the nanoscale dynamics of these domains are essential for understanding cellular processes [75]. Fluorescence microscopy is commonly utilized for the probing of nanoscale dynamics such as diffusion. However, fluorescent probes alter the molecular mass and structure of the molecules they interact with which may affect the results [137, 138]. Therefore, a label-free technique is ideal for directly probing the diffusion. Nuclear magnetic resonance (NMR) spectroscopy is a widely used chemical analysis technique that is label-free and non-invasive. Nitrogen vacancy (NV) centers have emerged as highly sensitive quantum sensors of magnetic signals at the nanoscale under ambient, biologically relevant conditions [5, 127]. Shallow NV-centers of only a few nanometers depth are highly sensitive to molecular motion on this length scale [67]. Therefore, nanoscale NMR using NV-centers can provide highly localized information about diffusion.

SPBs are established models for a complex biological membrane[139]. They consist of phospholipids adsorbed to a solid support[140], such as a NV-diamond. The dynamics of the bilayers are dependent on parameters such as the density of the lipid per area, the thickness of bilayer, and disorder of hydrophobic tails [138]. These parameters are all influenced by temperature[139]. Prior works have both theoretically and experimentally explored diffusion of supported lipid bilayers (SPBs) using NV-centers [113, 141]. Shagieva et al.[141] implemented a power law model of the decay of the NMR signal in the time domain.

This signal decay was analyzed as the motion of the molecule moving outside the detection area of a NV-center, and was related to the 2D dynamics of the lateral diffusion of SPBs. Their work used single NV-centers, which has far less sensitivity than an NV-ensemble. For that reason, they determined that the signal strength from nuclei with low gyromagnetic ratio such as ^{31}P was not strong enough to measure, and only ^{1}H signal could be detected [141]. Ishiwata et al.[113] explored diffusion of SPBs using NV-NMR using an NV-ensemble instead and measuring ^{1}H nuclei. Here we would mention, ^{1}H signal may originate from a variety of sources, including the surface termination of the diamond [22, 45] or inside the diamond from H_2 plasma during the chemical vapor deposition growth process [25], which was also observed in our prior work Liu. et al.[127] (see Fig. 6). The results however agreed with pulse field gradient (PFG) NMR measurements of lipid dispersions [142]. They also compared diffusion results using fluorescence microscopy and noted that markers have strongly variable results dependent on which marker is used (see Fig. 4 of the reference). It is , that probing diffusion using NV-NMR with nuclei unique to the SPB is still lacking in literature due to sensitivity challenges.

In this work, Dipalmitoylphosphatidylcholine (DPPC) is selected as the phospholipid for forming the SPB as in Ishiwata et al. for its similarities in properties to sphingomyelin (SM), a major constituent of membrane rafts [143]. For saturated phosphatidylcholines, such as DPPC, phase behavior in SPB is dominated by the main L_β–L_α (gel-fluid) transition [144]. DPPC has a melting point of around 41 °C [144], and therefore above that temperature, DPPC is no longer found in a gel phase but in a fluid one. Correlation spectroscopy at relevant temperatures using NV-centers of nuclei specific to the lipid bilayer such as ^{31}P can provide a high degree of localization to study the phase dependent lateral diffusion as nuclei enter and leave the sensing volume. Here, we observe a clear increase in diffusional broadening of the ^{31}P signal from the gel phase at 30 °C to the fluid phase at 45 °C, correlating with faster diffusion. Our diffusion measurement results are slower than what is obtained by fluorescence microscopy. This difference in addition to the knowledge of the distance dependence of NV-NMR signal indicate a slower diffusion of the bottom layer of the SPB which is a consequence of the

diamond substrate.

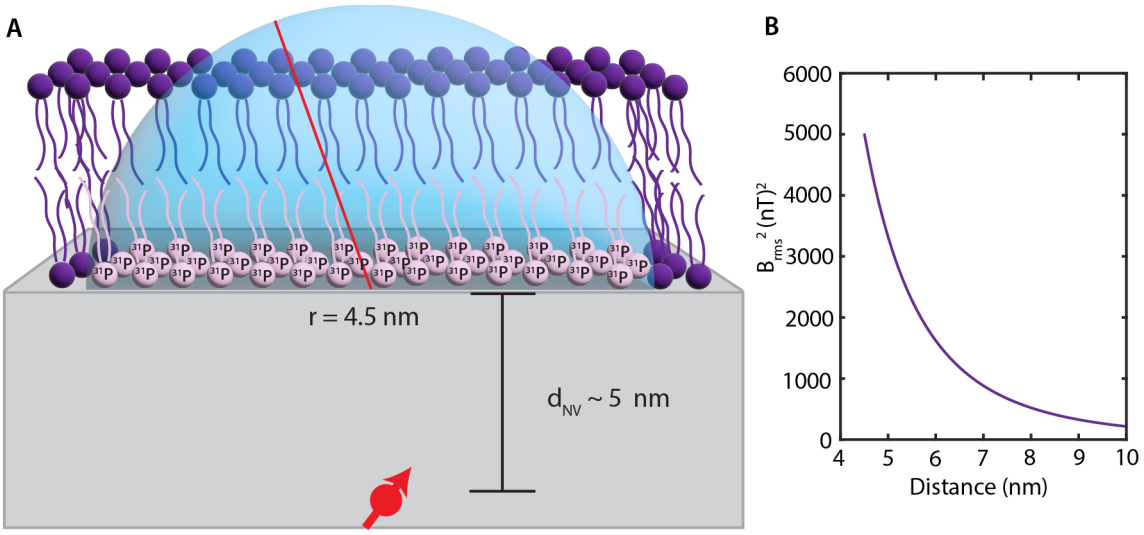

Figure 6.1.: A) Schematic of SPB on a diamond implanated with shallow NV-centers $\sim$ 5 nm in depth. B) Simulated distance dependent contribution of magnetic resonance signal from ^{31}P nuclei from gel phase DPPC sensed by NV-centers.

6.3. Results

6.3.1. Signal origins of NV-NMR.

NV-NMR is performed on a diamond chip in which ^{15}N was implanted with properties as previously described [127], resulting in a distribution of near-surface NV-centers 4.5 $\pm$ 1.9 nm below the surface [35]. The sensitive volume of each NV-center is then a hemisphere with a radius of approximately the depth (Fig. 6.1 A). In the gel phase at 30 °C, the thickness of a fully hydrated DPPC SPB obtained from atomic force microscopy (AFM) is $\sim$ 4.4 nm. In the fluid phase, the thickness decreases slightly and is $\sim$ 3.6 nm. [139, 145, 146] As the main contribution to the signal comes from nuclei closest to the NV-centers (Fig. 6.1 B), a crucial consideration of NV-NMR measurements is how the strength of the signal from the NMR active ^{31}P nuclei alters with distance from the NV-centers. The curve in Fig. 6.1 B depicts the expected signal originating from ^{31}P nuclei with the expected density of DPPC

SPB, calculated using the following equation [110]:

$$B_{rms}^2 = \frac{5\pi}{96}(\mu_0 h\gamma_{nuc}/4\pi)^2\rho[1/d_{NV}^3\text{-}1/(d_{NV}^3 + h_{spins}^3] \quad (1)$$

where $\mu_0 = 4\pi \times 10^7$ (m $\cdot$ T/A) is the vacuum permeability, h = 6.626 10^{34} (J $\cdot$ s) is the Planck constant, γ_{nuc} is the nuclear gyromagnetic ratio in MHz/T (17.235 MHz/T for ^{31}P), ρ is the nuclear spin density, d_{NV} is the depth of the shallow NV-centers, and h_{spins} is the thickness of the nuclear spin layer. Using the known area per lipid of 0.57 nm^2 to estimate approximately 1.75 ^{31}P atoms per nm^2 [144], and 0.2 nm, the size of the ^{31}P atom, as the thickness of the layer with nuclear spins, the equation correlates the measured signal size (B_{rms}^2) to the corresponding distance from the NV.

As expressed by the equation and shown in Figure 6.1, the signal contribution decreases cubically with distance from the NV-centers. The expected signal from a SPB is $\sim$4227 nT^2 at the 4.5 nm SRIM simulated implantation distance from the surface of the diamond. This reflects the distance of the NV-center to the ^{31}P nuclei of the phosphonate head groups within the bottom layer of the SPB. The expected signal then decreases to $\sim$ 547 nT^2 after an additional distance of 3.4 nm from the surface (to a total of 7.9 nm). This replicates the effect of the distance to the ^{31}P nuclei at the top of the SPB in the fluid phase. This expected signal further decreases to $\sim$374 nT^2 after 4.2 nm (to a total of 8.7 nm), which is the distance to the ^{31}P at the top of the SPB in the gel phase. These estimates indicate that only around 9 % of the signal comes from the top ^{31}P of the SPBs in the gel phase, and 13 % in the fluid phase.

6.3.2. Formation of supported phospholipid bilayers.

Small Unilamellar Vesicles (SUVs) favorably form SPB in an aqueous environments [81]. This formation is also dependent on having a hydrophilic surface [85], such as an acid cleaned diamond (see Appendix A.3.1: SWCA of clean diamond). The formation of the SPB on the diamond sample was confirmed through fluorescence recovery after photobleaching (FRAP) performed with DPPC sample mixed with 1 mol % Texas Red^{TM} 1,2-Dihexadecanoyl-sn-

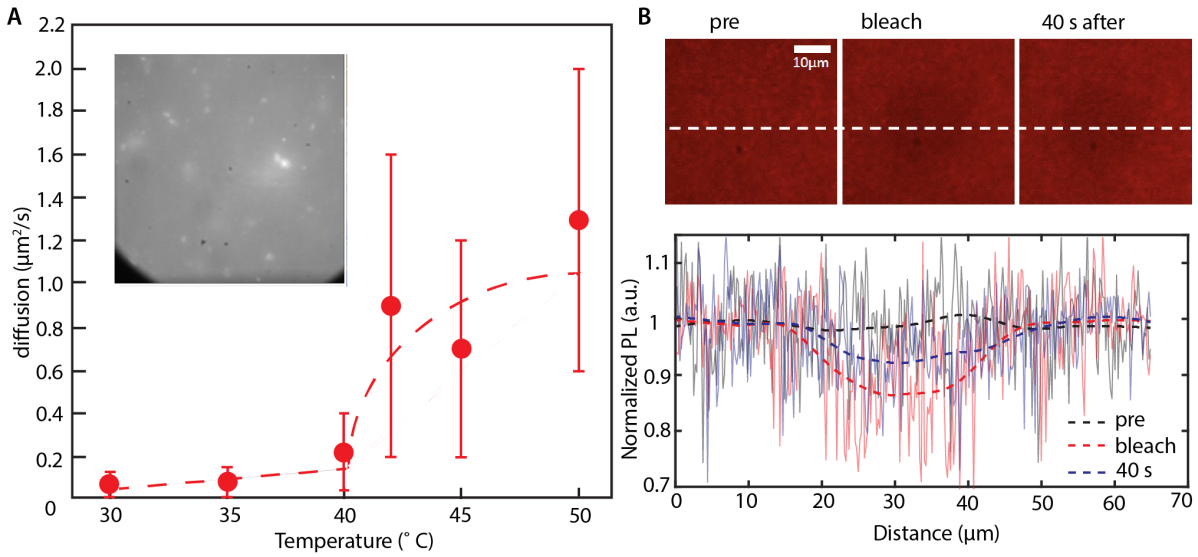

Figure 6.2.: A) Fluorescence recovery after photobleaching measured using Texas Red™ DHPE. Below the phase transition temperature of $\sim 41^{\circ}$C diffusion is slow (below 0.2 $\mu m^2/s$) in the gel phase. Above the phase transition temperature there is a rapid increase in diffusion in the fluid phase. Inset: fluorescence image of DPPC on diamond shows even bilayer formation (grey), bright spots are areas with multilayers. B) Bleaching recovery at 45 °C after 40 s indicates the formation of a SPB. Inset: Images of bleached spot. From left to right: before, after bleaching, and after 40 s of recovery time.

Glycero-3-Phosphoethanolamine, Triethylammonium Salt (Texas™ Red DHPE) with temperatures ranging from 30°C to 50 °C (Fig. 6.2 A). A simple fluorescence image at room temperature indicates a well-formed homogeneous SPB on a clean diamond with negligible formation of multilayers (inset of Fig. 6.2 A). Texas™ Red DHPE is bleached in the area of high laser exposure, and the fluorescence recovery is determined after 40 seconds. FRAP measurements at 45 °C is shown in Fig. 6.2 B as an example and demonstrates recovery of emission on laser damaged spot of lipid bilayer. This confirms the continuity of the SPB which has a fluidity that allows for the recovery of fluorescence. In the case of randomly deposited lipids, the laser damaged spot would show no recovery due to absence of a continuous SPB and diffusion between the damaged spot and surrounding areas that are not damaged. Below the melting temperature FRAP measurements indicate very slow diffusion (below 0.2 $\mu m^2/s$). FRAP shows a marked increase in fluorescence recovery above the melting temperature in the fluid phase correlating with faster diffusion.

6.3.3. Decay of NV-NMR signal with diffusion and influence on lineshape.

The linewidth of the ^{31}P NMR signal from the SPB measured by NV-NMR is dependent on its fluidity and how long it remains in the NV-center sensing volume. There are different ways to model this behavior, one of which is the exponential decay (Fig. 6.3 A). Considering an interaction time τ_d of a lipid molecule, the probability of a molecule staying within the sensing volume decreases exponentially with time such that S(t) $\sim$ cos(ωt)e-t/τ_d. The Fourier transform of this decay result in a Lorentzian line shape usually expressed as:

$$L(\tau,\omega)= \frac{1}{\pi} \frac{\tau_d}{1+(\omega-\omega_0)^2\tau_d} \quad (2)$$

where ω_0 specifies the center and τ_d is a parameter that determines the width. τ_d can be related to molecular diffusion by considering the linewidth, with a full width at half maximum (FWHM) $\frac{2}{\tau_d^2}$:

$$\tau_d=\frac{2d_{NV}^2}{D} \quad (3)$$

where d_{NV} is the depth of the NV-center and D is the diffusion coefficient [66]

The second way to model the behavior is using a power-law [141, 147, 148]. It has been suggested, that for times exceeding this characteristic diffusion time τ_d, the decay of the correlation signal diverges from an exponential decay for certain sample geometries and instead follows a power-law where S(t) $\sim$ cos(ωt)t$^{\alpha}$, where α depends on whether the diffusion is 2D or 3D (Fig. 6.3 B). The noise in the data reduces the R^2. However, considering the R^2 values as shown in Figure 6.3, the exponential fit is better suited for the τ_d in the range of the diffusion of DPPC SPBs in the gel phase. Therefore, and for consistency, we do line shape analysis using a Lorentzian fit for both gel and fluid phase data. The expected linewidths as a function of diffusion are shown in Figure 6.3 C.

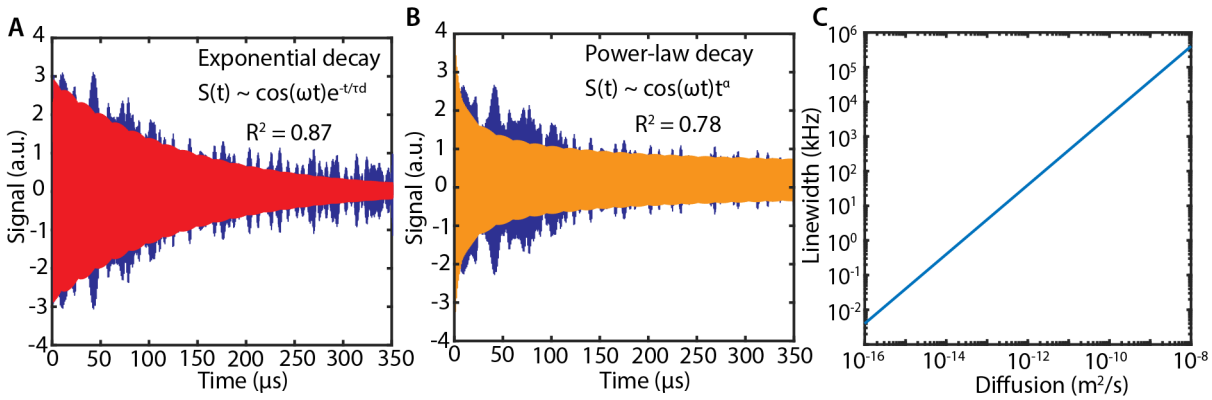

Figure 6.3.: Fitting of the time domain signal of ^{31}P signal from gel phase DPPC with an A) exponential decay and B) power-law decay. The R^2 values suggests that exponential decay fits our data with better predicted values. C) Effect of diffusion on signal linewidth from NV-NMR.

6.3.4. Probing diffusion of SPBs using NV-NMR.

Correlation spectroscopy was performed at 174 mT using 64 π pulses (see Appendix A.3.2: Experimental Conditions). Fourier transform of time traces revealed signals of $\sim$ 3 MHz, which match with the Larmor frequency of ^{31}P at this magnetic field. At 30 °C, an average linewidth of 2.6 $\pm$ 0.15 kHz was obtained for a SPB in the gel phase (Fig. 6.4). For a shallow NV ensemble on average 4.5 nm deep, this corresponds to a diffusion coefficient of $\sim$5.3 x 10^{-14} m^2/s. Notably, this would be below the FRAP resolution limit of 1 x 10^{-13} m^2/s. At 45 °C, an average linewidth of 3.9 $\pm$ 0.46 kHz linewidth was obtained for a SPB in the fluid phase, corresponding to a line broadening due to a $\sim$ 50 % increase in diffusion to $\sim$7.9 x 10^{-14} m^2/s (Fig. 6.4). This is more than an order of magnitude lower than 1.3 x 10^{-12} m^2/s measured using FRAP at 45 °C.

As discussed earlier, the ^{31}P signal contribution from the top layer of the SPB is less than from the bottom layer. Table 6.1 summarizes the results from FRAP experiments and NV-NMR. The large difference between the FRAP data analysis and the NV-NMR data analysis suggest that perhaps the bottom layer has slower diffusion than that of the top layer. The slower diffusion of the bottom layer has been observed before, and is substrate dependent [149]. Therefore for the first time, NV-NMR results indicate a slower diffusion of the bottom

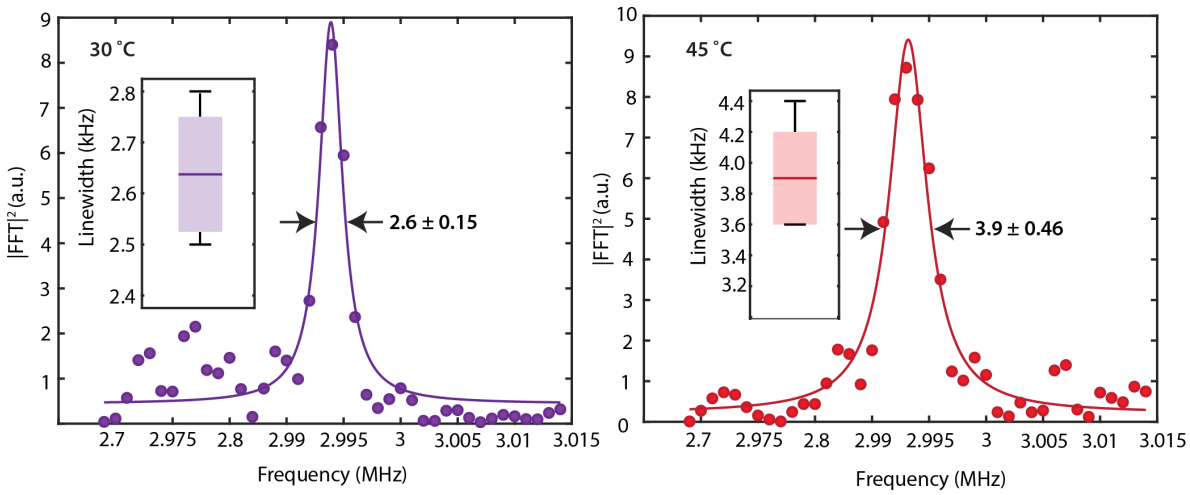

Figure 6.4.: Below the transition temperature at 30°C a linewidth of ∼2.6 kHz is observed (left). This corresponds to a diffusion of $\sim 5.3 \times 10^{-14}$ m^2/s. Above the transition temperature at 45°C a broadened linewidth of ∼ 4 kHz is observed (right). This corresponds to diffusion of $\sim 7.9 \times 10^{-14}$ m^2/s. Insets: statistics of ^{31}P signal linewidth, the purple and red lines indicate the mean, while the boxes show the upper and lower quartiles. Black lines show minimum and maximum values.

layer of a SPB formed on diamond.

	Gel phase	Fluid phase ^{31}P
FRAP	$1 \pm 0.1 \times 10^{-13}$ m^2/s	$1.3 \pm 0.7 \times 10^{-12}$ m^2/s
NV-NMR	$5.3 \pm 0.31 \times 10^{-14}$ m^2/s	$7.8 \pm 0.94 \times 10^{-14}$ m^2/s

Table 6.1.: Summary of diffusion measurements from FRAP and NV-NMR

6.4. Conclusion

In our work, we specifically probed nuclei unique to the SPBs, and observed the influence of the nuclei's location on the diffusion. The location of the ^{31}P nuclei only at the base and at the top of the SPB in our work uniquely allows us to selectively obtain information about the fluidity from the base of the bilayer. These results demonstrate the nuance of measuring diffusion using NV-NMR. Therefore, it is important to measure nuclei on the alkyl chains through which the two layers are in contact. In future work, better localization

should be performed, perhaps with a fluorinated alkyl chain. For the first time, NV-NMR was performed with sufficient sensitivity to detect nuclei unique to the DPPC SPB. This allows us to characterize the diamond as a support substrate that the bottom layer of the SPB may have slower diffusion on.

6.5. Materials and Methods

The diamond preparation and NV-NMR setup has been described in chapter 4.

6.5.1. Preparation of Small Unilamellar Vesicles (SUVs).

SUVs were made from 16:0 PC lipids (1,2-dipalmitoyl-sn-glycero-3-phosphocholine, Avanti Lipids). For fluorescence experiments, 1 mol% of TexasRed DHPE (TexasRed 1,2-Dihexadecanoyl-sn-Glycero-3-Phosphoethanolamine, Thermo Fisher) was added. To prepare the SUVs, 100 μL of a lipid stock solution (lipids dissolved in $CHCl_3$ to a concentration of 6.36 mM) was pipetted to a glass vial and dried using pressure air. The dry lipids were rehydrated with 1.5 mL of deionized H_2O and tip-sonicated (Bandelin Sonopuls) on ice at least two times for 30 s at high intensity until the solution became transparent. At last, the vesicle suspension was centrifuged for 10 min at 8000 rpm.

6.5.2. Fluorescence Recovery after Photobleaching (FRAP).

FRAP experiments were done on an inverted microscope (IX81, Olympus) equipped with a heating stage (temperature controllable range: 20-60 ^{c}ircC), a 60x air objective (Olympus, LUCPLFLN), a mercury short arc lamp (HBO, 100W), and a CCD camera (iXon Ultra, Andor) for image acquisition. Fluorescence excitation and SLB imaging were achieved with a green filter cube (λ_{exc} = 510-550 nm; λ_{em} > 590 nm) and suitable ND filters (ND2) that reduce photobleaching. The FRAP data, i.e. image series recorded with a frame rate of 20 Hz, were analyzed according to Jönsson et al.[150]. The method is based on circularly averaging the bleach spot profiles in each image frame and determining the radial recovery via spatial

frequency analysis/ numerical Hankel transformations. Thereby, impacts from nonideal imaging conditions, low signal-to-noise ratios, and photobleaching are minimized.

6.5.3. Formation of SPBs on diamond.

A bubble of 100 μL of the SUV and 100 μL of PBS 1X buffer solution was formed over the diamond, and incubated at a room temperature for 20 min. The process was repeated. Deionized water was added to increase the volume to ensure hydration of the bilayer over the time of NV-NMR experiments.

6.5.4. NV-NMR.

Correlation spectroscopy was performed using XY8-4 blocks (a total of 32 π pulses) with t_{corr} swept starting from 2 μs to obtain the spectra. For ^{31}P detection t^{corr} was swept until 350 μs in 3501 points. For the ^{31}P signal of the gel phase shown in Fig. 6.4 we obtain a SNR of 33 as calculated by dividing the signal value by the standard deviation of the noise floor within a region without signal. For the ^{31}P signal of the gel phase shown we obtain a SNR of 9.4. Each spectrum shown in Fig. 6.4 is zero-filled to 6500 points (650 μs). The time domain data was then Fourier transformed and the absolute value plotted using MATLAB. ^{31}P NMR signals were obtained in 160 minutes. After zero-filling, each power spectrum ($|\mathrm{FFT}|^2$) is plotted, and the linewidth of the resonance is fit with a Lorentzian model.

7. Concluding Remarks

In this work, we have made steps towards applying quantum sensing to surface science. Currently, the shallowly implanted diamonds have femtomole sensitivity. As the layer is only a few nanometers deep and is sensitive analogous to this depth, a practical way to reduce background noise and improve coherence properties is to enrich the diamonds with thin (hundreds of nanometers to a few micrometers) layers of ^{12}C diamonds.

Although this work has been completed using diamonds with natural abundance of ^{13}C, ^{12}C enriched diamonds have been acquired and future work would benefit from its properties. For example, especially with the detection of low gyromagnetic ratio nuclei such as ^{31}P, noise peaks appear which cannot be assigned to Larmor frequencies of known nuclei. In experimental data from the detection of drop cast phosphonic acid using diamonds with natural abundance ^{13}C, noise peaks are present from 3.5-4.5 MHz (Fig. 7.1). This indicates that the source of certain noise peaks are perhaps couplings with the ^{13}C. While these peaks are not particularly close to the ^{31}P around 3

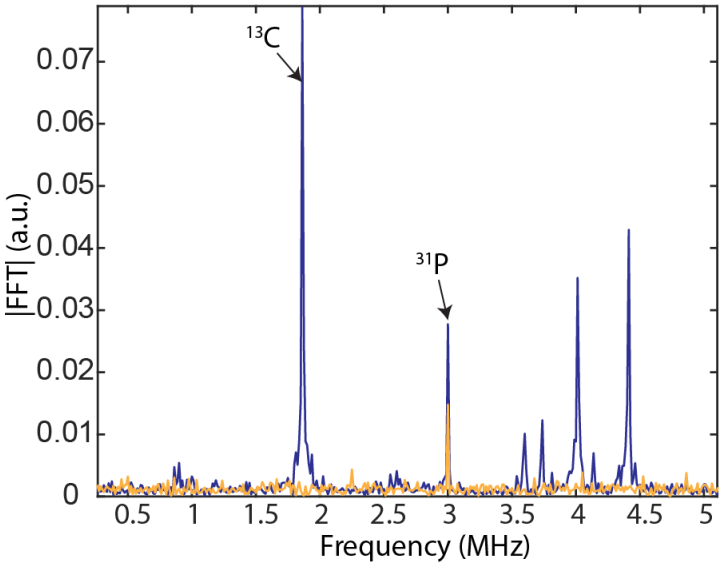

Figure 7.1.: Detection of drop cast phosphonic acid. Characteristic ^{13}C peak at 1.86 MHz is no longer visible in the ^{12}C enriched diamond. Many noise frequencies from 3.5 MHz to 4 MHz are also no longer detectable.

MHz, the noise patterns vary with the detection of different frequencies. For example, in spectroscopy of ^{2}H, sizable noise peaks appear at 0.58 MHz, 0.89 MHz, and 1 MHz (Fig. 7.2). Consequently, the noise peaks could potentially be an issue for the detection of other nuclei where at least one may appear where the Larmor frequency is expected. Performing NV-NMR spectroscopy with ^{12}C enriched diamonds would overcome this challenge.

Another limitation of this technology are the broad linewidths due to dipolar coupling which is greater than chemical shift at the magnetic fields we work at.

Therefore, we are unable to resolve chemical shifts and obtain chemical information in the way conventional NMR can. The frequency of ^{31}P at 1 T for example is 17.24 MHz. A chemical shift of 10 ppm would be $\sim$ 170 Hz. At 3 T, that would be $\sim$ 0.52 kHz which could potentially be resolvable by NV-NMR. Performing NV-NMR at or above 3 T however, is technically challenging and would require future efforts in technological development. Another potential route for obtaining chemical information is the detection of quadrupolar nuclei (nuclei with spin I > 1/2), which can provide structural information even with broad lineshapes. Nuclear quadrupole resonance spectroscopy is a powerful tool for chemical analysis due to the couplings of the nuclei to electric field gradients which results in more complex NMR energy levels and orientation dependent "powder patterns" [151]. NV-NMR could be applied to detect even atomically thin layers such as 2D materials of quadrupolar nuclei [101]. We explored quadrupolar nuclei detection of deuterium (^{2}H) at a moderate field. ^{2}H signal was acquired at 174 mT and room temperature using XY8-4 blocks (a total of 32 π pulses) with

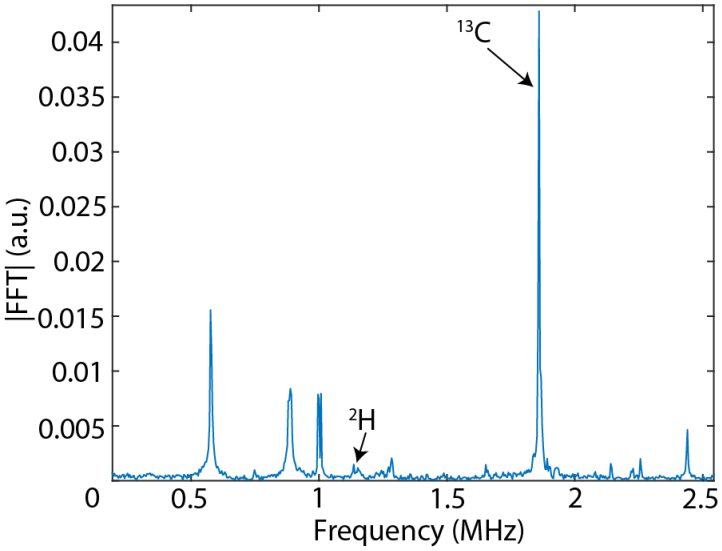

Figure 7.2.: Detection of ^{2}H from d62-DPPC lipid bilayer.

t_{corr} swept starting from 2 μs to obtain the spectra. The Larmor frequency of ^{2}H is around 1.137 MHz. For ^{2}H detection, t_{corr} was swept until 250 μs in 1251 points. The time domain data were then Fourier transformed and the absolute value plotted using MATLAB. Below the transition temperature of $\sim$ 41 °C, a splitting appears in the ^{2}H signal in the gel phase of the d62-dipalmitoylphosphatidylcholine (d62-DPPC) supported phospholipid bilayer.

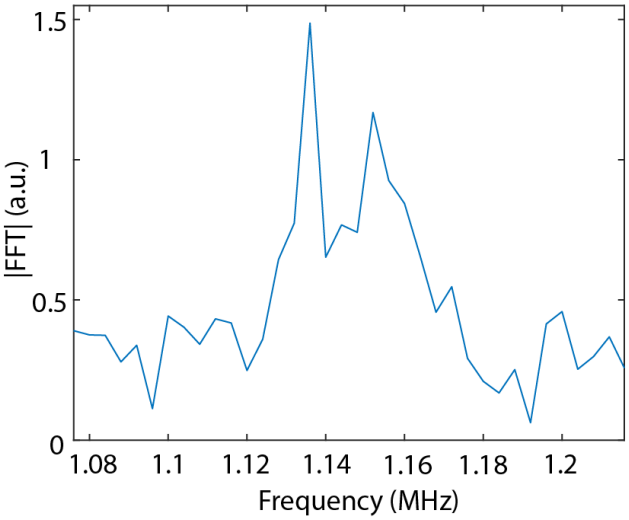

Figure 7.3.: ^{2}H spectrum in the gel phase at room temperature contains a splitting, with the first peak at 1.136 MHz and the other at 1.152 MHz.

This is similar to a methyl group splitting, although the broader pake may be cut off due to a combination of the low SNR and the filter window from our decoupling sequence. It is notable that we have an asymmetry, which is not expected from a spin-1 nuclei such as deuterium [152]. Prior work with ^{2}H detection of d62-DPPC using conventional solid-state NMR [153, 154] have shown symmetric splittings. Higher spin number nuclei such as ^{87}Rb[155] or ^{71}Ga [151] have shown more complex splittings and asymmetries. While it is not clear what exactly causes the asymmetry in our ^{2}H, quadrupolar effects are field dependent [151]. ^{2}H NMR in literature are performed at high fields to allow for detectable signal due to its inherent low sensitivity. We uniquely perform ^{2}H NMR at more moderate fields. In future work, more investigation is needed to understand this. However, these are initial results that would set the route towards obtaining structural information using nanoscale NMR.

A. Appendix

A.1. Supplementary Information: Surface NMR using quantum sensors in diamond

A.1.1. Comparing DNP-SENS to surface NV-NMR

	DNP-SENS [3]	Surface NV-NMR
Sensitivity	$\sim$ 1.8 nmol (1 h, SNR 21, ^{31}P)	$\sim$ 0.2 fmol (0.5 h, SNR 15, ^{31}P)
Cost	1-3 M $ (Superconducting magnet and gyrotron)	$\sim$ 20-40 K $ (Inexpensive microwave parts, permanent magnet, laser and a diamond chip)
Spatial Resolution	none	4000 μm^2 (higher resolution possible)
Linewidth	$\sim$ 10 ppm (magic angle spinning)	$\sim$ 1000 ppm (static conditions)

Table A.1.: Comparison of DNP-SENS to surface NV-NMR

A.1.2. Comparing established surface techniques to surface NV-NMR

	SIMS [156, 157]	XPS [158, 159]	SFG/SHG spectroscopy [160]	Surface NV-NMR
Basic principle	Mass spectrometry	Electron spectroscopy	Non-linear laser spectroscopy	Nuclear magnetic resonance
Information Content	Detects elemental, isotopic, or molecular composition	Detects elements and chemical states (electronic structure and density of electronic states)	Detects vibrational or electronic transitions	Detects NMR active nuclear spins
Ambient Conditions	No	Partly (e.g., ambient pressure XPS [161])	Yes	Yes
Limitations	Highly destructive to surface, Requires ultra-high vacuum	Cannot detect hydrogen, Possible sample degradation	Complicated optics	So far, lack of chemical shift resolution, Diamond substrate needed
Spatial resolution (lateral)	50-100 nm for NanoSIMs	Typically, microns - millimeters	Diffraction Limit, less than 1 μm in VIS/UV to >10 μm IR	In this study tens of microns, ultimately limited by diffraction
Sensitivity	+++	++	++	++
Costs ($)	>200,000	> 500,000	> 200,000	15,000- 40,000

Table A.2.: Surface techniques compared to surface NV-NMR

A.1.3. Annealing of implanted diamond for conversion to NV centers

After implantation, the diamond was annealed in vacuum to form NV centers using gradual ramp rates and precisely controlled temperatures. The time- and pressure-traces during the annealing process are shown in Fig. A.1. The specifications of the oven can be found in the

Methods section. The annealing procedure is critical for forming shallow NV centers, while preserving their sensitivity and brightness and avoiding graphitization of and/or damage to the surface.

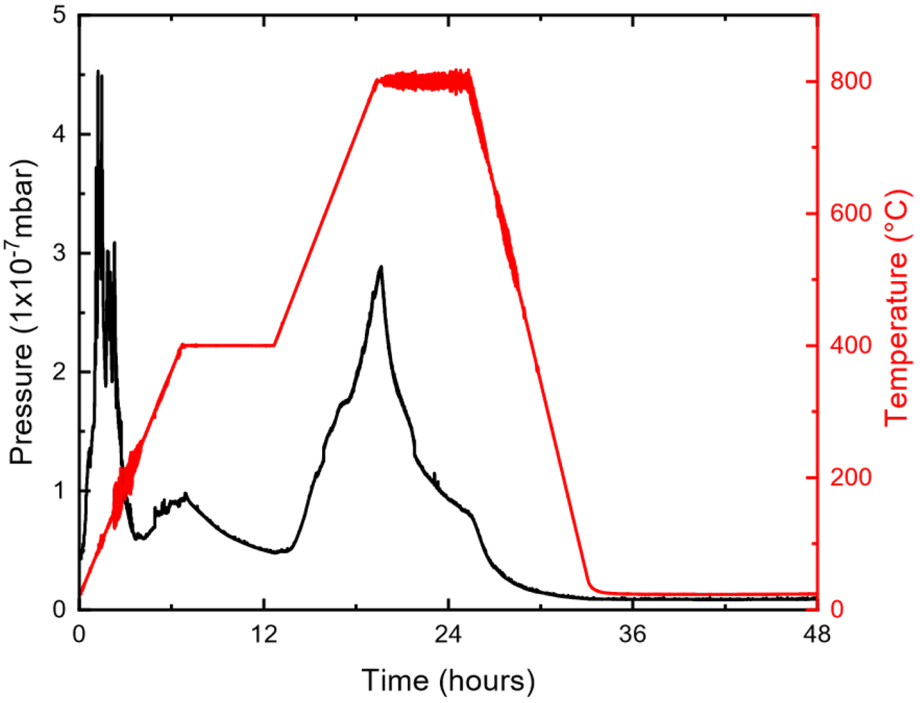

Figure A.1.: Diamond annealing: Temperature and pressure profiles of ^{15}N implanted diamond annealing procedure.

A.1.4. Properties of NV centers after annealing

The properties of our shallow NV-ensemble in diamond is depicted in Fig. S2. We used the NV resonance for the ms = 0 to -1 transition to determine the magnetic field strength. The contrast of the Rabi oscillations is typically around 7 % for dry state (shown in blue), but is reduced to 4 % in the case of liquid samples on the diamond (shown in yellow). An alternative to the detection of NMR signals on the nanoscale with correlation spectroscopy are dynamic decoupling sequences, where the time between the π pulses is swept. Two dips, corresponding to the ^{19}F and ^{1}H can be observed in this experiment. The spin-lattice relaxation time T_1, is measured by increasing the time between optical initialization and readout. Fitting to an exponential

gives a range of 700 to 800 μs for clean diamond and after ALD. The spin-spin relaxation time T_2, is measured with a Hahn Echo sequence. The pulse sequence consists of a sequence of $\pi/2$-t-π-t-$\pi/2$ pulses, where t is swept. After the $\pi/2$ pulse, the Bloch vector starts to rotate in the plane due to magnetic noise. The π pulse sandwiched by the two $\pi/2$ cancels phase accumulation if the magnetic noise is identical in the two free precession times. Since the magnetic noise B fluctuate over time, the spin echo will decay called Hahn Echo or NV-T_2. The dips arise from coupling with ^{13}C in the diamond. The data are fit to a stretched exponential function resulting in a range from 4-6 μs for clean diamond and after ALD deposition.

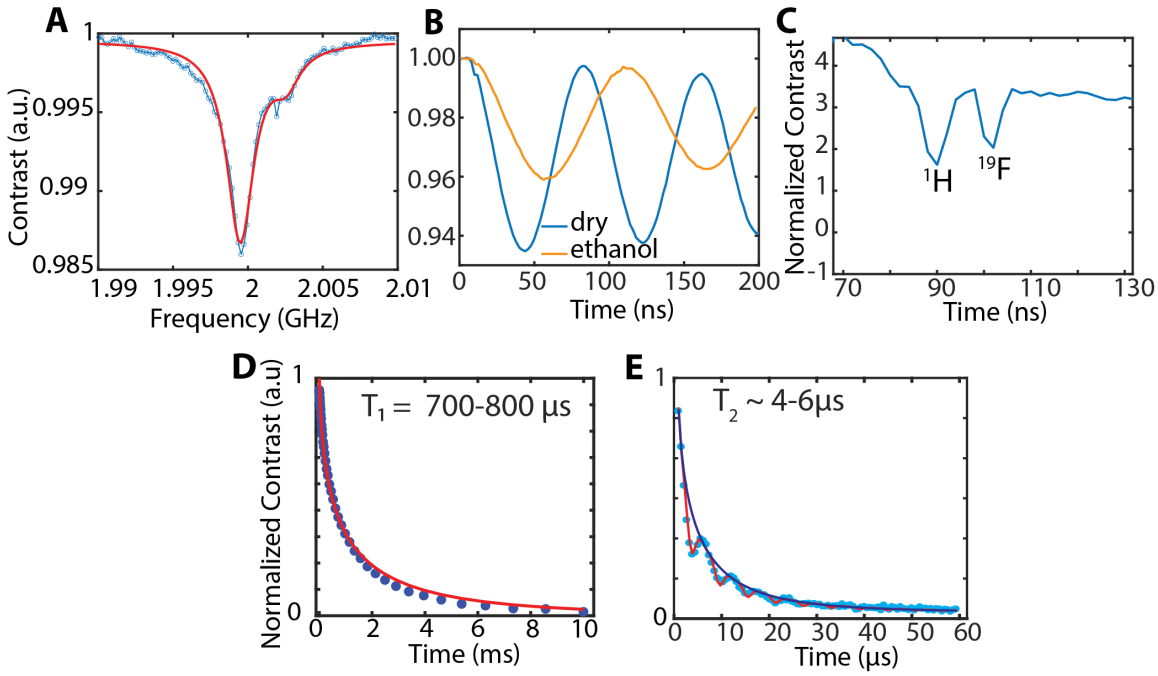

Figure A.2.: Example of NV ensemble properties A) ESR lineshape and resonance frequency B) Typical Rabi contrast dry and in ethanol C) XY8-12 dips of the ^{1}H peak on the left and the ^{19}F peak from drop cast phosphonic acid on the surface on the right. D) Spin-lattice relaxation T_1 E) Spin-spin relaxation T_2.

A.1.5. SRIM simulation of ^{15}N implantation depth

The Monte Carlo simulations using a software package SRIM (Stopping and Range of Ions in Matter) gives a mean depth of 4.5 nm with a range of $\pm$ 1.9 nm in crystalline diamond. The acceleration energy is 2.5 keV. The incident angle is 7 $^\circ$ normal to the surface.

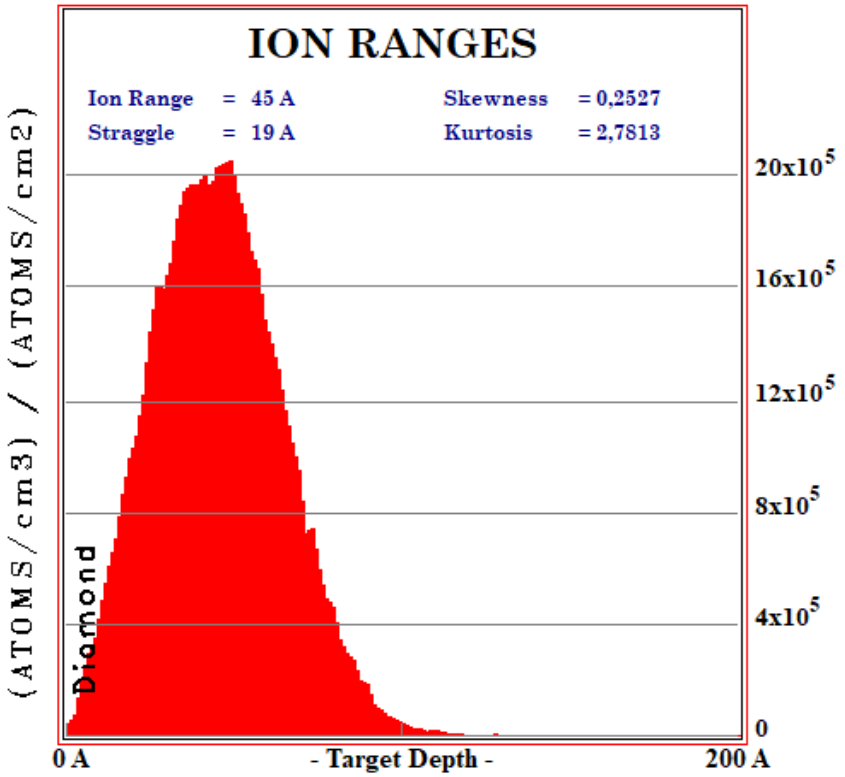

Figure A.3.: SRIM simulation of ^{15}N ion implantation.n

A.1.6. Gaussian fitting of laser spot size

Photoluminescence (PL) spot size of our NV centers was imaged and the size was determined by vertical and horizontal cuts which were fit to a Gaussian function. The laser spot was imaged using a Basler a2A1920-160umBAS camera (Fig. 4.2 C). The entire diamond was imaged with a known size of 2 mm as our reference. Fitting a vertical cut through the center of the laser spot to a Gaussian lineshape allowed for the determination of a full width at half maximum (FWHM) of 61.8 μm. The horizontal line had a FWHM of 82.9 μm. Taking these

values as the maximal extent of an elliptical area yields a total of $\sim 4000\ \mu m^2$.

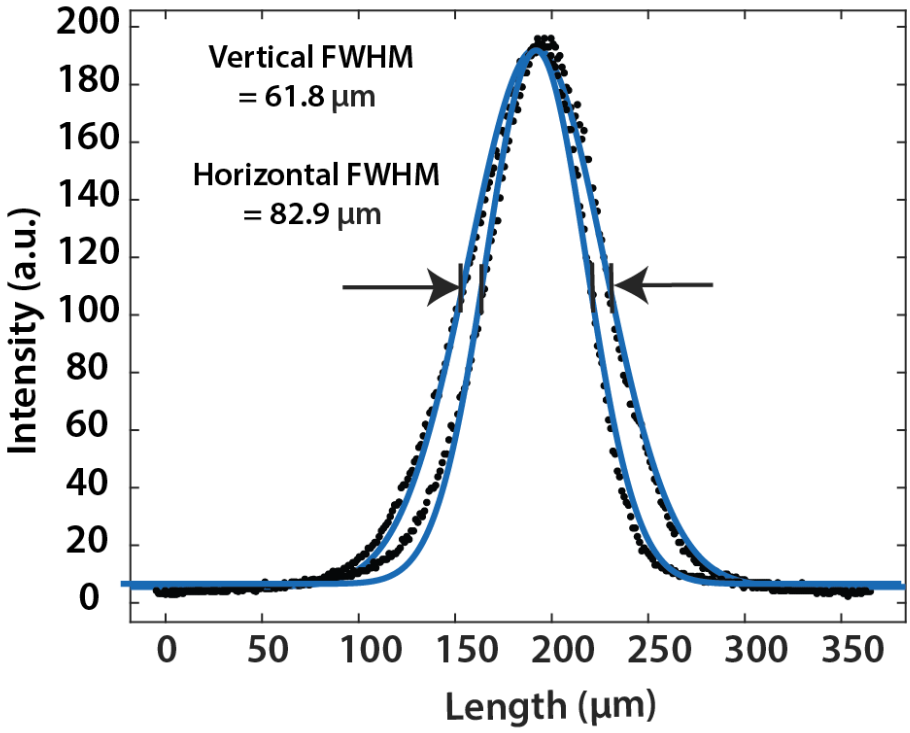

Figure A.4.: Area of optical excited NV centers. The photoluminescence (PL) spot size of our NV centers was imaged and the size was determined by vertical and horizontal cuts which were fit to a Gaussian function.

A.1.7. Determining optimal Al_2O_3 layer thickness for monolayer assembly

As NMR signal decreases with the cubed distance from the NV center, it is crucial to keep the Al_2O_3 layer as thin as possible. However, it must also be sufficiently thick to form a closed layer that enables assembly of dense molecular monolayers based on phosphonate linking chemistry. We used static water contact angle measurements to determine the thinnest layer of Al_2O_3 that reaches saturation, as well as to verify dense, ordered monolayer growth from PFPDPA. As a reference, a clean diamond without an Al_2O_3 layer was soaked in a phosphonic acid solution without undergoing the ALD process. The low contact angle indicates low reactivity. By contrast, for an Al_2O_3 layer of 1 nm after soaking in phosphonic acid has a

contact angle of approximately 91 degrees. Comparable angle values are maintained for 2 and 3 nm, which indicates that the monolayer reaches a saturation value. Therefore, a thickness of 1 nm was chosen as the thickness of the Al_2O_3 for surface NV-NMR due to the fact that the nuclear spins are as close as possible to the NV layer for sensing and thick enough to form a dense monolayer.

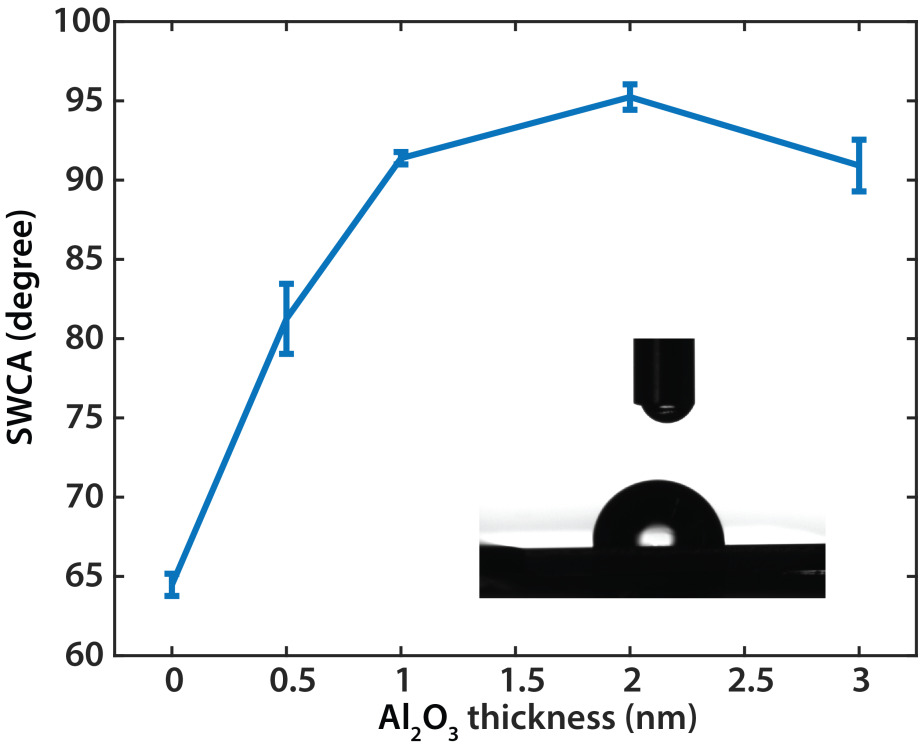

Figure A.5.: Static water contact angle as a function of monolayer growth on different Al_2O_3 layer thicknesses

A.1.8. Magnetic field sweep of ^{31}P signal

The ^{31}P from the PFPDPA monolayer was detected at 3 different magnetic fields. A linear fit of the resonance frequency as a function of magnetic field is used to calculate the gyromagnetic ratio. This corroborates that the source of the signal arises from ^{31}P spins. The gyromagnetic ratio of 17.24 (17.24, 17.25) MHz/T matches the known value for ^{31}P.

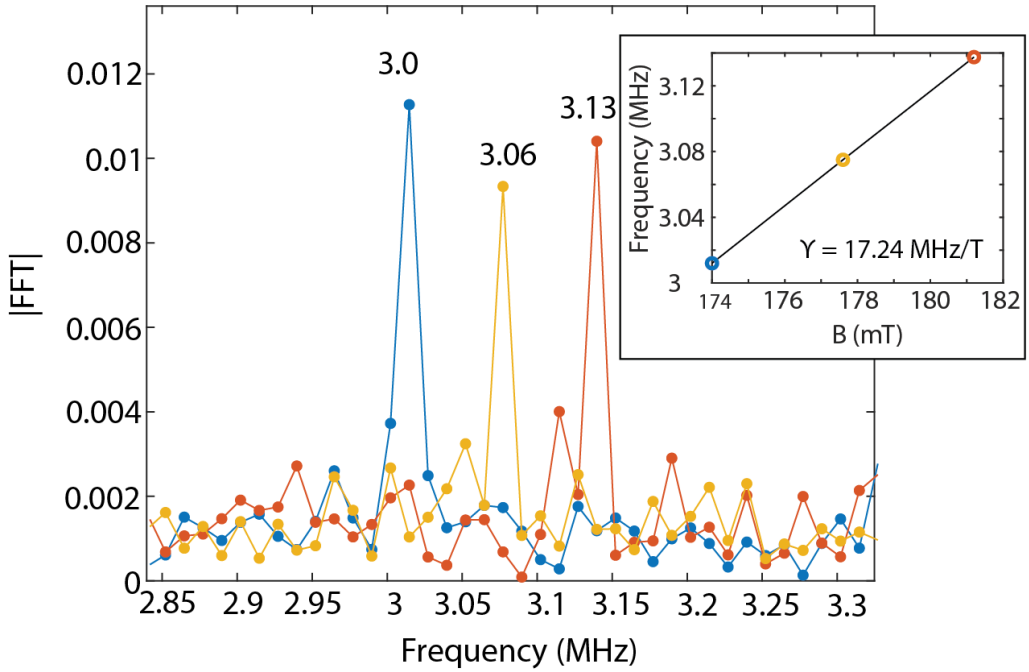

Figure A.6.: Magnetic field sweep of ^{31}P signal from PFPDPA monolayer.

A.1.9. Comparison of the linewidths of the ^{19}F and ^{31}P resonances

We performed experiments comparing the line broadening of the ^{19}F and the ^{31}P peaks when the sample is in the form of a monolayer and when is simply drop cast. These results indeed show that the formation of the monolayer causes a stronger broadening of the ^{31}P resonance (2.4x), in comparison to the ^{19}F which increases only $\sim$ 1.4x (PFPDPA). This indicates that surface attachment has a stronger effect on the ^{31}P nuclei than on the ^{19}F, also taking into account the difference in the gyromagnetic ratios. In addition to the PFPDPA phosphonic acid, we also investigated the linewidth of the ^{19}F resonance for a polyfluorinated chain molecule (PFOPA acid). Compared to PFPDPA, we observe an overall resonance linewidth which is much broader, probably caused by restricted mobility of the ^{19}F molecules, see Chapter 4. The linewidth change upon formation of the monolayer is comparable to that of PFDPA. These results indicate that the phosphorus headgroup exhibits the largest increase in linewidth upon forming the SAM layer. One possible reason could be increased relaxation

due to magnetic noise (e.g. caused by spin defects [162]) in the ALD layer, also indicated by the reduced T_1 relaxation time of the NV centers.

	drop cast (kHz)	SAM (kHz)
^{31}P linewidth	2.7 ± 0.2	6.6 ± 1.5
^{19}F linewidth	PFPDPA: 2.4 ± 0.1 PFOPA: 9.9 ± 1.6	PFPDPA: 3.4 ± 0.3 PFOPA: 13 ± 1.1

Table A.3.: Comparison of the linewidths of the ^{19}F and ^{31}P resonances

A.1.10. Determining of the thickness of the organophosphate and Al_2O_3 surface

The Al_2O_3 is only weakly bound to the diamond surface (van der Waals interactions) while the phosphonate is covalently bound to the Al_2O_3. Therefore during the scratching experiment both the Al_2O_3 and the organic PFPDPA monolayer is removed from the surface. The height of this organic monolayer and Al_2O_3 is determined to be 2.9 ± 0.26 nm. After minimizing the energy using Avogadro, the size of the molecule is estimated to be 2.06 nm. With a known Al_2O_3 of 0.9 nm, the height corresponds to the thickness of a monolayer.

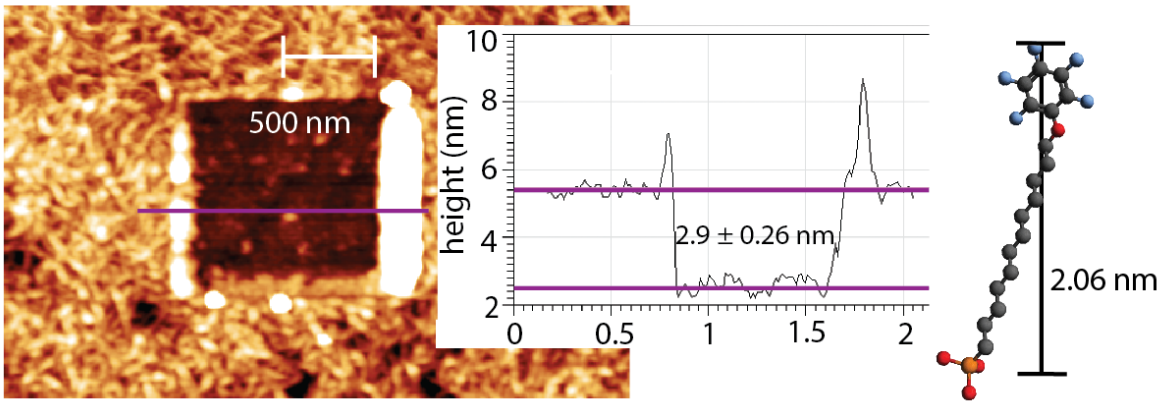

Figure A.7.: AFM scratching experiment of the Al_2O_3 and PFPDPA monolayer

A.1.11. Fitting parameters of the monolayer growth kinetics

The rate of monolayer formation can be influenced by changing the concentration of the PFPDPA solution for the in situ growth kinetics experiments. The averaged data points for

each concentration were fit with a single exponential: $y = a(1 - e^{-bx}) + c$. We observe an increase in the rate with an increase in concentration (Table A.4).

[Conc.]	a	b	c
1 mM	0.81	0.10	0.13
10 μM	0.084	0.052	0.13
1 μM	0.093	0.039	0.027

Table A.4.: Fitting parameters of the monolayer growth kinetics

A.1.12. Diamond surface cleaning for redeposition of Al_2O_3

To be able to reproduce the ALD and monolayer growth process, removal of the Al_2O_3 is crucial. XPS measurements of F 1s and Al 2s peaks before (blue) and after (yellow) overnight soaking in 5% NaOH shows that NaOH is effective at completely removing the monolayer and Al_2O_3.

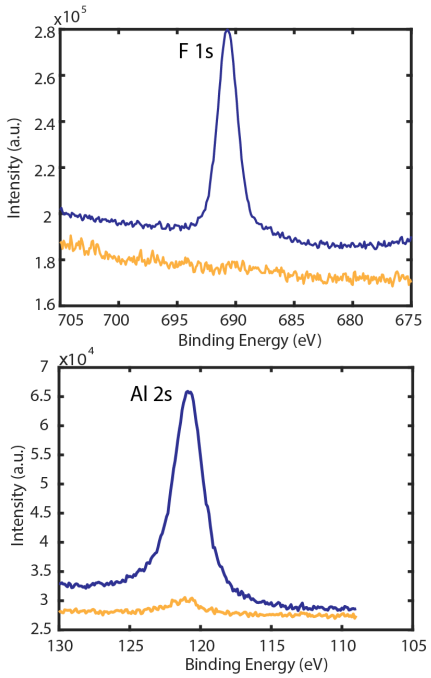

Figure A.8.: XPS of the surface before and after Al_2O_3 removal with NaOH

A.2. Supplementary Information: Using metal-organic frameworks to confine liquid samples for nanoscale NV-NMR

A.2.1. Elemental analysis of TMP and UiO-66 MOF powder

The TMP content was determined via elemental analysis, which was performed with Euro EA (HEKAtech). Upon dynamic spontaneous combustion (+Sn=1800°C) and with subsequent chromatographic separation and determination using a thermal conductivity detector, the percent by weight (wt. %) of different elements were determined. The molar ratio between UiO-66 and the guest is approximately 1:6 when the UiO-66 powders were directly filtered without washing after being immersed in TMP liquid for two days, with an experimental P (phosphorous) content of about 7.54 wt.%. This value was obtained by matching the experimental phosphorus content to what is expected from the chemical formulas of UiO-66 and TMP. To remove the TMP adsorbed on the surface, the powders were repeatedly washed. The resulting molar ratio of UiO-66 to TMP was found to be 1:2 with a 3.15 wt.% phosphorous content.

UiO-66 +x Guest(TMP)	C	H	Zr	P
Exp.	25.4	2.90	24.4	3.15
0	34.6	1.70	32.9	0.00
1	40.0	2.07	30.3	1.72
2	33.4	2.39	28.2	3.19
3	32.4	2.67	26.3	4.46
4	32.4	2.91	24.6	5.57
5	32.0	3.12	6.55	23.2
6	31.7	3.31	7.42	21.9

Table A.5.: Elemental analysis of (TMP)x@UiO-66. X in (TMP)x@UiO-66 indicates the amount of TMP based on the best match of the experimental phosphorus value.

A.2.2. Estimation of pore filling from elemental analysis

We estimate the amount of pores available to corroborate whether TMP fills the pores of UiO-66 MOF and to estimate to what extent. Our calculations are based on literature porosity values, the spherical geometry of the pores, and the elemental analysis reported above. UiO-66 is characterized by two pores diameters, and so an average of the two are calculated to have a volume of 4.5×10^{-28} m^3. Next, we multiply the literature porosity by the weight of 1 mol of MOF to get the number of pores per mol of MOF. We chose the most suitable porosity considering both literature and commercially available UiO-66 MOF (`https://www.strem.com/catalog/v/40-1105/`)[123, 130–132]. 0.5 cm^3/g × 1664 g = 8.3×10^{-4} m^3 of pore volume/ mol of MOF. Then we divide by the average pore volume to get the number of pores: 8.3×10^{-4} m^3 / 4.5×10^{-28} m^3 = 1.9×10^{24} pores/mol of MOF. Our elemental analysis indicates the presence of 2 mol of TMP/mol of MOF, which would be 1.2×10^{24} total TMP molecules. This indicates that approximately 63% of the total pores are filled assuming that each pore can trap 1 TMP molecule.

A.2.3. Experimental Conditions

The properties of our shallow NV-ensemble in diamond after the growth of a UiO-66 SURMOF layer on the surface are depicted in Table A.6. We used the NV resonance for the ms = 0 to -1 transition to determine the magnetic field strength. The contrast of the Rabi oscillations is on average 4.2 %. The spin-lattice relaxation time T_1 was fit to an exponential, giving a range of 2.2 $\pm$ 0.79 ms. The spin-spin relaxation time T_2 was fit to a stretched exponential function, resulting in a range of 5.8 $\pm$ 0.35 μs.

Contrast (%)	T_1 (ms)	T_2 (μs)
4.2 $\pm$ 0.83	2.2 $\pm$ 0.79	5.8 $\pm$ 0.35

Table A.6.: Active NV ensemble coherence properties and Rabi contrast

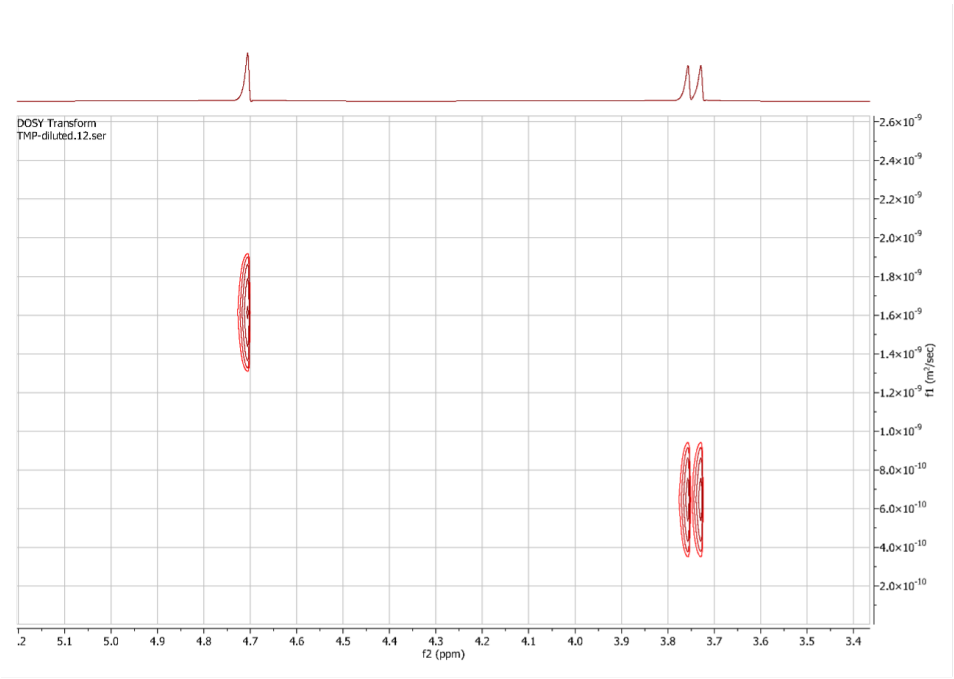

Figure A.9.: Diffusion-ordered NMR spectroscopy experiment of trimethyl phosphate in D_2O reveals a doublet split ^1H signal by ^{31}P and a diffusion coefficient of approximately $6{\times}10^{-10}$ m^2/s. To the right, a water signal shows a diffusion of $1.6{\times}10^{-10}$ m^2/s, which is close to the diffusion coefficient of D_2O at near room temperature.

A.2.4. Diffusion-ordered NMR Spectroscopy of Trimethyl Phosphate

Nuclear magnetic resonance (NMR) samples were prepared by adding 30 μL of neat trimethyl phosphate (TMP) and then 570 μL of D_2O to total 600 μL in a 5 mm NMR tube. Diffusion experiments were carried out on the ^1H signal in an Avance II 400 MHz 9.4 T (Bruker Biospin) NMR device using a stimulated echo Pulse Field Gradient NMR pulse sequence. The intensity change in NMR signal in the DOSY experiment is described by: $I = I_0 e^{-D\gamma^2 g^2 \delta^2 (\Delta - \frac{\delta}{3})}$, where I is the observed intensity, I is the unattenuated intensity, D is the diffusion coefficient, γ is the gyromagnetic ratio of the observed nucleus (26752.2205 rad·Hz/G for ^1H), g is the gradient strength (0.24 G/cm to 45.7 G/cm), δ is the length of the gradient (3.6 ms) and Δ is the diffusion time (100 ms). To simplify, the parameters can be combined as: $I = I_0 e^{-Dq^2(\Delta - \frac{\delta}{3})}$. The gradients were changed in 32 steps to generate $q^2(\Delta - \delta/3)$ up to $1.92{\times}10^6$ s/cm^2. The

data were then processed in Mestrenova with the DOSY processing using the Bayesian method. The ^{1}H signal from TMP was split into a doublet by the ^{31}P nuclei, for which a diffusion coefficient of $\sim 6{\times}10^{10}$ m^2/s was obtained. The ^{1}H signal from H_2O is also visible, yielding a diffusion coefficient in D_2O of $1.6{\times}10^{-6}$ m^2/s, which is close to the diffusion of D_2O near room temperature obtained using the tracer method [163].

A.2.5. Measuring ^{31}P signal from dried MOF

To ensure that the detected signal comes from within the pores of the MOF, after filling the pores with TMP the liquid was removed from the assembly and was rinsed with H_2O, in which TMP is soluble. Then the MOF-coated diamond was soaked in H_2O for 1 h and dried with nitrogen. The contrast increases from 4.2% to 7% due to the diamond/MOF/air interface, allowing 50 percent more light to be detected by our photodiode in comparison to the diamond/MOF/TMP interface, where more light escapes the diamond. A strong ^{31}P signal is still present, indicating that the signal originates from TMP within the pores since there are no other sources of ^{31}P.

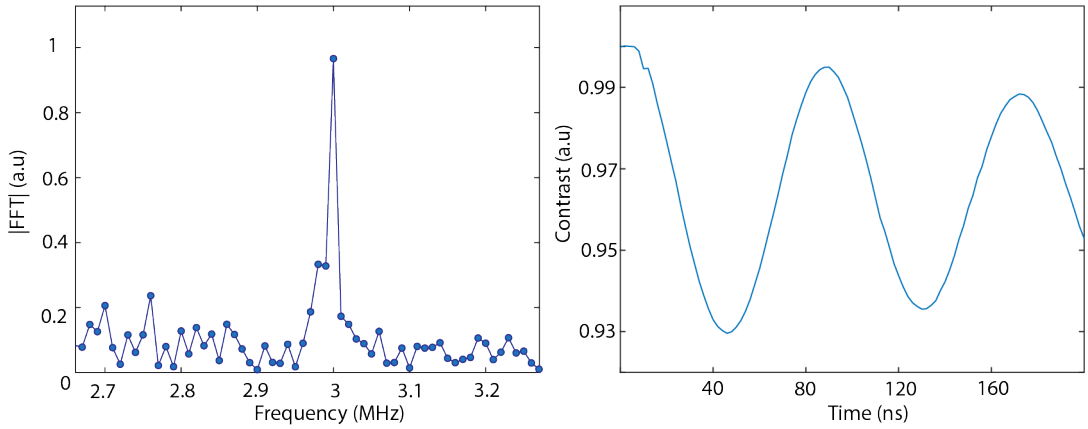

Figure A.10.: Left: ^{31}P signal from MOF rinsed and soaked in H_2O and then dried with nitrogen indicates that the signal originates from within the pores of the MOF. Right: The contrast for measuring the MOF dry rather than soaked in TMP increases from 4.2% to 7% due to less light escaping the diamond due to the higher refractive index of TMP compared to air

A.2.6. Signal normalization using a 1 MHz reference signal

To accurately compare between the ^{31}P signal from UiO-66 SURMOF soaked in TMP and Al_2O_3 soaked in TMP we use a 1 MHz reference signal. Variations in the resulting signal size from a signal source of the same strength would be due to differences in experimental conditions. To ensure that the lack of signal is not due to much less sensitive experimental conditions, we normalize the data using correlation spectroscopy data of the 1 MHz signal measured to 80 μs in 401 points obtained before each ^{31}P correlation experiment. The ^{31}P experiment on only Al_2O_3 is 67% as sensitive as the ^{31}P experiment with the SURMOF.

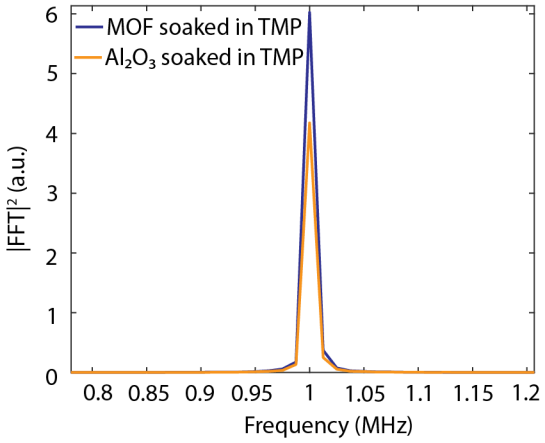

Figure A.11.: 1 MHz coil signal indicating experimental conditions for each dataset in 5

A.2.7. Calculation of TMP density within UiO-66 SURMOF pores from Elemental Analysis

From the molar ratio obtained from elemental analysis of UiO-66 MOF powder, we can make an estimate for the density of TMP molecules to corroborate our calibration and whether the NV-NMR signal size agrees with the porosity of UiO-66. In a prior publication[124] of the UiO-66 SURMOF growth method it was found that 9700 ng of UiO-66 SURMOF was deposited on a 14 mm diameter quartz crystal microbalance (154 mm^2 circular area). In our laser spot of 4000 μm^2, that would correspond to 0.25 ng or 1.5×10^{-13} mol of UiO-66 and

3×10^{-13} mol of TMP. Multiplying by Avogadro's number gives 1.8×10^{11} molecules of TMP. Dividing this by the total cylindrical volume of 3.4×10^{11} nm (calculated from the area of the laser spot multiplied by 85 nm average height of the UiO-66 SURMOF) 3 yields a density of 530 molecules of TMP/$(10\text{nm})^3$. This agrees well with the NV-NMR experimental calibration.

A.3. Supplementary Information: Probing phase dependent diffusion of lipid bilayers using quantum sensors in diamond

A.3.1. SWCA of acid cleaned diamond

Figure A.12.: SWCA measurements of acid cleaned diamond show a rather hydrophilic surface of 46 $\pm$ 0.9 degrees.

Static water contact angle (SWCA) measurements were performed on an OCA 15Pro contact angle system (DataPhysics Instruments). The acquisition of data and its evaluation were conducted with SWCA 20 - contact angle (DataPhysics Instruments, version 2.0). A 2 μL droplet of deionized H_2O (18.2 M Ωcm at 25 °C, Merck Millipore) was dispensed at a rate of 0.2 μL/s from a 500 μL Hamilton syringe onto the sample surface. After allowing the droplet to settle for $\sim$ 3 s, an image was acquired for further processing and quantification of the average Young's contact angle ($\theta\gamma$). This procedure was performed on different spots on the surface, and the standard deviation (error) was determined. The obtained results indicate a

hydrophilic surface.

A.3.2. Experimental conditions

The coherence properties of our shallow NV-ensemble in diamond are depicted in Table A.7. The spin-lattice relaxation time T_1 fit to an exponential gives a range of 3.0 $\pm$ 2.1 ms. The spin-spin relaxation time T_2 fit to a stretched exponential function resulting in a range of 6.0 $\pm$ 0.12 μs.

Contrast (%)	T_1 (ms)	T_2 (μs)
6.2 $\pm$ 1.2	3.0 $\pm$ 2.1	6.- $\pm$ 0.12

Table A.7.: Active NV ensemble coherence properties and Rabi contrast

A.4. Diffusion measured with deuterium

Prior work from Shagieva et al.[141] and Ishiwata et al.[113] with experimental sensitivity that precluded detection of nuclei with low gyromagnetic ratios such as ^{31}P which NMR detects with lower sensitivity. The benefit of our technique using an ensemble of NV-centers is that we can detect not only ^{31}P but even inherently less sensitive and more challenging to detect nuclei such as ^{2}H. This allows us to measure DPPC with deuterated alkyl chains and probe diffusion measurements from the chain between the lipid layers. FRAP measurements indicates successful formation of the deuterated SPB with slower diffusion values than non-deuerated (Fig. A.13 A). We note that ^{2}H as a quadrupolar nuclei in the solid-state have strong orientation dependent splitting that result in a "pake" pattern, which we also observe from the gel phase at 30 °C (see Chapter 7. However, in the fluid phase the line becomes sharp and narrow with increased molecular motion [154]. The broad shoulders usually observed in ^{2}H Solid-State NMR may also be filtered by our decoupling sequence (see Chapter 3.4.6: Correlation Experiment and Filter Window). SPBs were formed using a deuterated d62-DPPC. Correlation spectroscopy of ^{2}H nuclei was performed at 174 mT, with signal appearing at the ^{2}H Larmor frequency of $\sim$ 1.14 kHz. ^{2}H NMR signals were obtained by sweeping until 250

*mu*s in 1251 points, 10 averages taking 9 hours with an SNR of 9. The spectrum shown in Fig. A.13 is zero-filled to 1501 points (300 μs), and the power spectrum fit to the Lorentzian model. The ^{2}H signals show a linewidth of $\sim$ 7 kHz (Fig. A.13 B). This corresponds to a diffusion of approximately 1.5 x 10^{-13} m^2/s. This is 3 times lower than what was measured from FRAP measurements. Nonetheless, it is considerably more similar than what is measured from ^{31}P which was over an order of magnitude lower for the fluid phase. In conventional NMR, quadrupolar splitting is averaged out in the liquid state. Our data shows no splittings, which may indicate that at the nanoscale quadrupolar splitting may be mitigated with much less molecular motion.

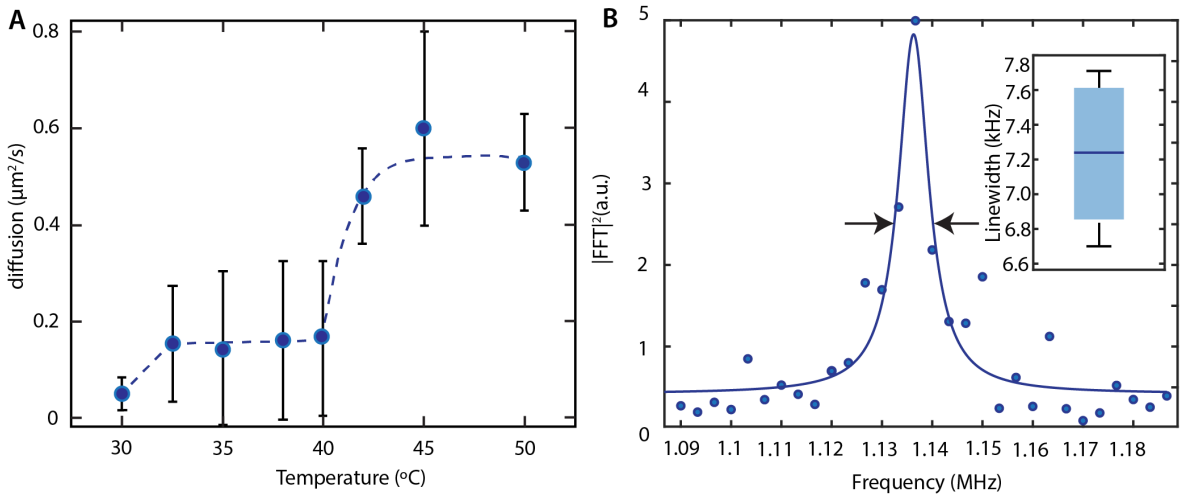

Figure A.13.: A) FRAP measurements of d62-DPPC indicates a transition temperature similar to non-deuterated DPPC. Obtained diffusion measurements are slower than non-deuterated DPPC. B) ^{2}H spectrum obtained in the fluid phase reveal a linewidth of $\sim$ 7.3 kHz. Inset: statistics of ^{2}H signal linewidth, the blue line indicates the mean, while the box shows the upper and lower quartiles. Black lines show minimum and maximum values.

Bibliography

[1] B. Reif, S. E. Ashbrook, L. Emsley, M. Hong, *Nature Reviews Methods Primers* **2021**, *1*, 2, http://www.nature.com/articles/s43586-020-00002-1 (visited on 04/08/2022).

[2] A. J. Rossini, A. Zagdoun, M. Lelli, A. Lesage, C. Copéret, L. Emsley, *Accounts of Chemical Research* **2013**, *46*, Publisher: American Chemical Society, 1942–1951, https://doi.org/10.1021/ar300322x (visited on 12/29/2020).

[3] B. J. Walder, C. Berk, W.-C. Liao, A. J. Rossini, M. Schwarzwälder, U. Pradere, J. Hall, A. Lesage, C. Copéret, L. Emsley, *ACS Central Science* **2019**, *5*, Publisher: American Chemical Society, 515–523, https://doi.org/10.1021/acscentsci.8b00916 (visited on 12/29/2020).

[4] A. Lesage, M. Lelli, D. Gajan, M. A. Caporini, V. Vitzthum, P. Miéville, J. Alauzun, A. Roussey, C. Thieuleux, A. Mehdi, G. Bodenhausen, C. Coperet, L. Emsley, *Journal of the American Chemical Society* **2010**, *132*, Publisher: American Chemical Society, 15459–15461, https://doi.org/10.1021/ja104771z (visited on 12/29/2020).

[5] R. Schirhagl, K. Chang, M. Loretz, C. L. Degen, *Annual Review of Physical Chemistry* **2014**, *65*, 83–105, http://www.annualreviews.org/doi/10.1146/annurev-physchem-040513-103659 (visited on 06/25/2020).

[6] C. Müller, X. Kong, J.-M. Cai, K. Melentijević, A. Stacey, M. Markham, D. Twitchen, J. Isoya, S. Pezzagna, J. Meijer, J. F. Du, M. B. Plenio, B. Naydenov, L. P. McGuinness, F. Jelezko, *Nature Communications* **2014**, *5*, Publisher: Springer Science and Business Media LLC, DOI 10.1038/ncomms5703, https://doi.org/10.1038/ncomms5703.

[7] N. Aslam, M. Pfender, P. Neumann, R. Reuter, A. Zappe, F. Fávaro de Oliveira, A. Denisenko, H. Sumiya, S. Onoda, J. Isoya, J. Wrachtrup, *Science* **2017**, *357*, 67–71, http://www.sciencemag.org/lookup/doi/10.1126/science.aam8697 (visited on 11/05/2019).

[8] F. Höök, B. Kasemo, M. Grunze, S. Zauscher, *ACS Nano* **2008**, *2*, 2428–2436, https://pubs.acs.org/doi/10.1021/nn800800v (visited on 08/17/2022).

[9] D. W. Boukhvalov, V. Paolucci, G. D'Olimpio, C. Cantalini, A. Politano, *Physical Chemistry Chemical Physics* **2021**, *23*, 7541–7552, http://xlink.rsc.org/?DOI=D0CP03317K (visited on 08/17/2022).

[10] M. Salmeron, *Topics in Catalysis* **2018**, *61*, 2044–2051, http://link.springer.com/10.1007/s11244-018-1069-0 (visited on 02/17/2021).

[11] A. W. Overhauser, *Phys. Rev.* **1953**, *92*, Publisher: American Physical Society, 411–415, https://link.aps.org/doi/10.1103/PhysRev.92.411.

[12] J. M. Taylor, P. Cappellaro, L. Childress, L. Jiang, D. Budker, P. R. Hemmer, A. Yacoby, R. Walsworth, M. D. Lukin, *Nature Physics* **2008**, *4*, 810–816, https://doi.org/10.1038/nphys1075.

[13] M. W. Doherty, N. B. Manson, P. Delaney, F. Jelezko, J. Wrachtrup, L. C. Hollenberg, *Physics Reports* **2013**, *528*, 1–45, https://linkinghub.elsevier.com/retrieve/pii/S0370157313000562 (visited on 06/10/2022).

[14] L. Childress, R. Hanson, *MRS Bulletin* **2013**, *38*, 134–138, https://doi.org/10.1557/mrs.2013.20.

[15] V. M. Acosta, D. Budker, P. R. Hemmer, J. R. Maze, R. L. Walsworth in *Optical Magnetometry*, (Eds.: D. Budker, D. F. Jackson Kimball), Cambridge University Press, Cambridge, **2013**, pp. 142–166, https://www.cambridge.org/core/product/identifier/CBO9780511846380A062/type/book_part (visited on 06/10/2022).

[16] R. H. Telling, C. J. Pickard, M. C. Payne, J. E. Field, *Phys. Rev. Lett.* **2000**, *84*, Publisher: American Physical Society, 5160–5163, https://link.aps.org/doi/10.1103/PhysRevLett.84.5160.

[17] T. Evans, Z. Qi, J. Maguire, *Journal of Physics C: Solid State Physics* **1981**, *14*, Publisher: IOP Publishing, L379–L384, https://doi.org/10.1088/0022-3719/14/12/005.

[18] G. Davies, T. Evans, R. W. Ditchburn, *Proceedings of the Royal Society of London. A. Mathematical and Physical Sciences* **1972**, *328*, Publisher: Royal Society, 413–427, https://doi.org/10.1098/rspa.1972.0086 (visited on 06/11/2022).

[19] A. Zaitsev, *Optical Properties of Diamond A Data Handbook*, 1st ed., Springer Berlin, Heidelberg, 502 pp.

[20] J. Manca, M. Nesladek, M. Neelen, C. Quaeyhaegens, L. De Schepper, W. De Ceuninck, *Microelectronics Reliability* **1999**, *39*, 269–273, https://www.sciencedirect.com/science/article/pii/S002627149800225X.

[21] T. Teraji, T. Yamamoto, K. Watanabe, Y. Koide, J. Isoya, S. Onoda, T. Ohshima, L. J. Rogers, F. Jelezko, P. Neumann, J. Wrachtrup, S. Koizumi, *physica status solidi (a)* **2015**, *212*, 2365–2384, https://onlinelibrary.wiley.com/doi/10.1002/pssa.201532449 (visited on 06/12/2022).

[22] L. V. H. Rodgers, L. B. Hughes, M. Xie, P. C. Maurer, S. Kolkowitz, A. C. Bleszynski Jayich, N. P. de Leon, *MRS Bulletin* **2021**, *46*, 623–633, https://link.springer.com/10.1557/s43577-021-00137-w (visited on 05/18/2022).

[23] S. B. Shirey, P. Cartigny, D. J. Frost, S. Keshav, F. Nestola, P. Nimis, D. G. Pearson, N. V. Sobolev, M. J. Walter, *Reviews in Mineralogy and Geochemistry* **2013**, *75*, 355–421, https://pubs.geoscienceworld.org/rimg/article/75/1/355-421/140964 (visited on 06/12/2022).

[24] J. Stiegler, T. Lang, M. Nygard-Ferguson, Y. von Kaenel, E. Blank, *Diamond and Related Materials* **1996**, *5*, 226–230, https://www.sciencedirect.com/science/article/pii/0925963595003495.

[25] J. Achard, V. Jacques, A. Tallaire, *Journal of Physics D: Applied Physics* **2020**, *53*, 313001, https://iopscience.iop.org/article/10.1088/1361-6463/ab81d1 (visited on 06/10/2022).

[26] Y. Borzdov, Y. Palyanov, I. Kupriyanov, V. Gusev, A. Khokhryakov, A. Sokol, A. Efremov, *Diamond and Related Materials* **2002**, *11*, 1863–1870, https://linkinghub.elsevier.com/retrieve/pii/S092596350200184X (visited on 05/11/2020).

[27] J. Raymakers, K. Haenen, W. Maes, *Journal of Materials Chemistry C* **2019**, *7*, 10134–10165, http://xlink.rsc.org/?DOI=C9TC03381E (visited on 11/05/2019).

[28] M. Schwander, K. Partes, *Diamond and Related Materials* **2011**, *20*, 1287–1301, https://www.sciencedirect.com/science/article/pii/S0925963511002913.

[29] J. Achard, A. Tallaire, V. Mille, M. Naamoun, O. Brinza, A. Boussadi, L. William, A. Gicquel, *physica status solidi (a)* **2014**, *211*, 2264–2267, https://onlinelibrary.wiley.com/doi/10.1002/pssa.201431181 (visited on 06/12/2022).

[30] D. B. Bucher, D. P. L. Aude Craik, M. P. Backlund, M. J. Turner, O. Ben Dor, D. R. Glenn, R. L. Walsworth, *Nature Protocols* **2019**, *14*, 2707–2747, http://www.nature.com/articles/s41596-019-0201-3 (visited on 03/18/2020).

[31] S. Pezzagna, B. Naydenov, F. Jelezko, J. Wrachtrup, J. Meijer, *New Journal of Physics* **2010**, *12*, 065017, https://iopscience.iop.org/article/10.1088/1367-2630/12/6/065017 (visited on 04/29/2020).

[32] A. J. Healey, A. Stacey, B. C. Johnson, D. A. Broadway, T. Teraji, D. A. Simpson, J.-P. Tetienne, L. C. L. Hollenberg, *Physical Review Materials* **2020**, *4*, 104605, https://link.aps.org/doi/10.1103/PhysRevMaterials.4.104605 (visited on 07/13/2022).

[33] J. M. Smith, S. A. Meynell, A. C. B. Jayich, J. Meijer, *Nanophotonics* **2019**, *8*, Publisher: De Gruyter Section: Nanophotonics, 1889–1906, https://www.degruyter.com/document/doi/10.1515/nanoph-2019-0196/html (visited on 04/05/2021).

[34] F. Fávaro de Oliveira, D. Antonov, Y. Wang, P. Neumann, S. A. Momenzadeh, T. Häußermann, A. Pasquarelli, A. Denisenko, J. Wrachtrup, *Nature Communications* **2017**, *8*, 15409, https://doi.org/10.1038/ncomms15409.

[35] J. F. Ziegler, M. Ziegler, J. Biersack, *19th International Conference on Ion Beam Analysis* **2010**, *268*, 1818–1823, https://www.sciencedirect.com/science/article/pii/S0168583X10001862.

[36] F. Ziem, M. Garsi, H. Fedder, J. Wrachtrup, *Scientific Reports* **2019**, *9*, Number: 1 Publisher: Nature Publishing Group, 12166, https://www.nature.com/articles/s41598-019-47084-w (visited on 09/30/2020).

[37] A. Healey, L. Hall, G. White, T. Teraji, M.-A. Sani, F. Separovic, J.-P. Tetienne, L. Hollenberg, *Physical Review Applied* **2021**, *15*, 054052, https://link.aps.org/doi/10.1103/PhysRevApplied.15.054052 (visited on 05/27/2021).

[38] T. Lühmann, R. John, R. Wunderlich, J. Meijer, S. Pezzagna, *Nature Communications* **2019**, *10*, 4956, http://www.nature.com/articles/s41467-019-12556-0 (visited on 08/11/2020).

[39] T. Lühmann, J. Meijer, S. Pezzagna, *physica status solidi (a)* **2021**, *218*, _eprint: https://onlinelibrary.wiley.com/doi/pdf/10.1002/pssa.202170021, 2170021, https://onlinelibrary.wiley.com/doi/abs/10.1002/pssa.202170021 (visited on 06/11/2021).

[40] E. L. Thomas, G. W. Nelson, S. Mandal, J. S. Foord, O. A. Williams, *Carbon* **2014**, *68*, 473–479, https://www.sciencedirect.com/science/article/pii/S0008622313010725.

[41] Z. Yuan, M. Fitzpatrick, L. V. H. Rodgers, S. Sangtawesin, S. Srinivasan, N. P. de Leon, *Phys. Rev. Research* **2020**, *2*, Publisher: American Physical Society, 033263, https://link.aps.org/doi/10.1103/PhysRevResearch.2.033263.

[42] S. J. DeVience, L. M. Pham, I. Lovchinsky, A. O. Sushkov, N. Bar-Gill, C. Belthangady, F. Casola, M. Corbett, H. Zhang, M. Lukin, H. Park, A. Yacoby, R. L. Walsworth, *Nature Nanotechnology* **2015**, *10*, Number: 2 Publisher: Nature Publishing Group, 129–134, https://www.nature.com/articles/nnano.2014.313 (visited on 01/05/2021).

[43] A. Krueger, D. Lang, *Advanced Functional Materials* **2012**, *22*, 890–906, http://doi.wiley.com/10.1002/adfm.201102670 (visited on 11/05/2019).

[44] M. Kaviani, P. Deák, B. Aradi, T. Frauenheim, J.-P. Chou, A. Gali, *Nano Letters* **2014**, *14*, 4772–4777, https://pubs.acs.org/doi/10.1021/nl501927y (visited on 06/13/2022).

[45] S. Sangtawesin, B. L. Dwyer, S. Srinivasan, J. J. Allred, L. V. H. Rodgers, K. De Greve, A. Stacey, N. Dontschuk, K. M. O'Donnell, D. Hu, D. A. Evans, C. Jaye, D. A. Fischer, M. L. Markham, D. J. Twitchen, H. Park, M. D. Lukin, N. P. de Leon, *Physical Review X* **2019**, *9*, 031052, https://link.aps.org/doi/10.1103/PhysRevX.9.031052 (visited on 11/05/2019).

[46] K. J. Brown, E. Chartier, E. M. Sweet, D. A. Hopper, L. C. Bassett, *Journal of Chemical Health and Safety* **2019**, *26*, 40–44, https://www.sciencedirect.com/science/article/pii/S187155321930043X.

[47] H. J. Mamin, M. Kim, M. H. Sherwood, C. T. Rettner, K. Ohno, D. D. Awschalom, D. Rugar, *Science* **2013**, *339*, 557–560, https://www.sciencemag.org/lookup/doi/10.1126/science.1231540 (visited on 12/19/2020).

[48] T. Staudacher, F. Shi, S. Pezzagna, J. Meijer, J. Du, C. A. Meriles, F. Reinhard, J. Wrachtrup, *Science* **2013**, *339*, 561–563, https://www.sciencemag.org/lookup/doi/10.1126/science.1231675 (visited on 03/18/2020).

[49] P. Kehayias, A. Jarmola, N. Mosavian, I. Fescenko, F. M. Benito, A. Laraoui, J. Smits, L. Bougas, D. Budker, A. Neumann, S. R. J. Brueck, V. M. Acosta, *Nature Communications* **2017**, *8*, Publisher: Springer Science and Business Media LLC, DOI 10.1038/s41467-017-00266-4, https://doi.org/10.1038/s41467-017-00266-4.

[50] C. A. Meriles, L. Jiang, G. Goldstein, J. S. Hodges, J. Maze, M. D. Lukin, P. Cappellaro, *The Journal of Chemical Physics* **2010**, *133*, _eprint: https://doi.org/10.1063/1.3483676, 124105, https://doi.org/10.1063/1.3483676.

[51] C. L. Degen, M. Poggio, H. J. Mamin, D. Rugar, *Physical Review Letters* **2007**, *99*, Publisher: American Physical Society, 250601, https://link.aps.org/doi/10.1103/PhysRevLett.99.250601.

[52] D. B. Bucher in *eMagRes*, _eprint: https://onlinelibrary.wiley.com/doi/pdf/10.1002/9780470034590.em John Wiley & Sons, Ltd, **2019**, pp. 363–370, https://onlinelibrary.wiley.com/doi/abs/10.1002/9780470034590.emrstm1619.

[53] S. Dutt, A. K. Gupta, K. R. Aadil, N. Bunekar, V. K. Mishra, R. Kumar, A. Gupta, A. Chaudhary, A. Kumar, M. Chawla, K. Gugulothu in *Metal Oxides for Biomedical and Biosensor Applications*, (Ed.: K. Mondal), Elsevier, **2022**, pp. 321–352, https://www.sciencedirect.com/science/article/pii/B9780128230336000119.

[54] A. S. Ivanova, *Kinetics and Catalysis* **2012**, *53*, 425–439, https://doi.org/10.1134/S0023158412040039.

[55] R. L. Puurunen, *Journal of Applied Physics* **2005**, *97*, Publisher: American Institute of Physics, 121301, https://doi.org/10.1063/1.1940727 (visited on 02/10/2021).

[56] M. Xie, X. Yu, L. V. H. Rodgers, D. Xu, I. Chi-Durán, A. Toros, N. Quack, N. P. de Leon, P. C. Maurer, *Proceedings of the National Academy of Sciences* **2022**, *119*, e2114186119, https://pnas.org/doi/full/10.1073/pnas.2114186119 (visited on 06/13/2022).

[57] A. A. Malygin, V. E. Drozd, A. A. Malkov, V. M. Smirnov, *Chemical Vapor Deposition* **2015**, *21*, 216–240, https://onlinelibrary.wiley.com/doi/abs/10.1002/cvde.201502013.

[58] A. Rahtu, T. Alaranta, M. Ritala, *Langmuir* **2001**, *17*, Publisher: American Chemical Society, 6506–6509.

[59] R. L. Puurunen, M. Lindblad, A. Root, A. O. I. Krause, *Phys. Chem. Chem. Phys.* **2001**, *3*, Publisher: The Royal Society of Chemistry, 1093–1102, http://dx.doi.org/10.1039/B0072490.

[60] W. Bigelow, D. Pickett, W. Zisman, *Journal of Colloid Science* **1946**, *1*, 513–538, https://www.sciencedirect.com/science/article/pii/0095852246900591.

[61] D. M. Spori, N. V. Venkataraman, S. G. P. Tosatti, F. Durmaz, N. D. Spencer, S. Zürcher, *Langmuir* **2007**, *23*, 8053–8060, https://pubs.acs.org/doi/10.1021/la700474v (visited on 11/10/2020).

[62] K. Fukuda, T. Hamamoto, T. Yokota, T. Sekitani, U. Zschieschang, H. Klauk, T. Someya, *Applied Physics Letters* **2009**, *95*, 203301, http://aip.scitation.org/doi/10.1063/1.3259816 (visited on 10/29/2020).

[63] H. Dietrich, T. Schmaltz, M. Halik, D. Zahn, *Physical Chemistry Chemical Physics* **2017**, *19*, 5137–5144, http://xlink.rsc.org/?DOI=C6CP08681K (visited on 11/22/2019).

[64] S. P. Pujari, L. Scheres, A. T. M. Marcelis, H. Zuilhof, *Angewandte Chemie International Edition* **2014**, *53*, 6322–6356, http://doi.wiley.com/10.1002/anie.201306709 (visited on 01/09/2021).

[65] H. Dietrich, D. Zahn, *The Journal of Physical Chemistry C* **2017**, *121*, 18012–18020, https://pubs.acs.org/doi/10.1021/acs.jpcc.7b05750 (visited on 11/10/2020).

[66] L. M. Pham, S. J. DeVience, F. Casola, I. Lovchinsky, A. O. Sushkov, E. Bersin, J. Lee, E. Urbach, P. Cappellaro, H. Park, A. Yacoby, M. Lukin, R. L. Walsworth, *Phys. Rev. B* **2016**, *93*, Publisher: American Physical Society, 045425, https://link.aps.org/doi/10.1103/PhysRevB.93.045425.

[67] D. Cohen, R. Nigmatullin, M. Eldar, A. Retzker, *Advanced Quantum Technologies* **2020**, 2000019, https://onlinelibrary.wiley.com/doi/abs/10.1002/qute.202000019 (visited on 06/26/2020).

[68] O. M. Yaghi, M. O'Keeffe, N. W. Ockwig, H. K. Chae, M. Eddaoudi, J. Kim, *Nature* **2003**, *423*, 705–714, https://doi.org/10.1038/nature01650.

[69] H. Wu, Y. S. Chua, V. Krungleviciute, M. Tyagi, P. Chen, T. Yildirim, W. Zhou, *Journal of the American Chemical Society* **2013**, *135*, 10525–10532, https://pubs.acs.org/doi/10.1021/ja404514r (visited on 07/08/2022).

[70] O. Shekhah, H. Wang, S. Kowarik, F. Schreiber, M. Paulus, M. Tolan, C. Sternemann, F. Evers, D. Zacher, R. A. Fischer, C. Wöll, *Journal of the American Chemical Society* **2007**, *129*, Publisher: American Chemical Society, 15118–15119, https://doi.org/10.1021/ja076210u.

[71] D. Zacher, R. Schmid, C. Wöll, R. A. Fischer, *Angewandte Chemie International Edition* **2011**, *50*, Publisher: John Wiley & Sons, Ltd, 176–199, https://doi.org/10.1002/anie.201002451 (visited on 07/21/2022).

[72] K. Geng, T. He, R. Liu, S. Dalapati, K. T. Tan, Z. Li, S. Tao, Y. Gong, Q. Jiang, D. Jiang, *Chemical Reviews* **2020**, *120*, Publisher: American Chemical Society, 8814–8933, https://doi.org/10.1021/acs.chemrev.9b00550.

[73] M. Agrawal, S. E. Boulfelfel, D. F. Sava Gallis, J. A. Greathouse, D. S. Sholl, *The Journal of Physical Chemistry Letters* **2019**, *10*, 7823–7830, https://pubs.acs.org/doi/10.1021/acs.jpclett.9b03119 (visited on 03/01/2022).

[74] W. Li, S. Mukerjee, B. Ren, R. Cao, R. A. Fischer, *Advanced Energy Materials* **2021**, 2003499, https://onlinelibrary.wiley.com/doi/10.1002/aenm.202003499 (visited on 04/29/2021).

[75] E. Sezgin, I. Levental, S. Mayor, C. Eggeling, *Nature reviews. Molecular cell biology* **2017**, *18*, Edition: 2017/03/30, 361–374, https://pubmed.ncbi.nlm.nih.gov/28356571.

[76] T. Skotland, K. Sandvig, A. Llorente, *Progress in Lipid Research* **2017**, *66*, 30–41, https://www.sciencedirect.com/science/article/pii/S0163782716300492.

[77] S. Welsch, B. Müller, H.-G. Kräusslich, *FEBS Letters* **2007**, *581*, 2089–2097, http://doi.wiley.com/10.1016/j.febslet.2007.03.060 (visited on 07/22/2022).

[78] E. T. Castellana, P. S. Cremer, *Surface Science Reports* **2006**, *61*, 429–444, https://linkinghub.elsevier.com/retrieve/pii/S0167572906000616 (visited on 07/22/2022).

[79] I. Reviakine, A. Brisson, *Langmuir* **2000**, *16*, 1806–1815, https://pubs.acs.org/doi/10.1021/la9903043 (visited on 07/22/2022).

[80] V. P. Zhdanov, C. A. Keller, K. Glasmästar, B. Kasemo, *The Journal of Chemical Physics* **2000**, *112*, Publisher: American Institute of Physics, 900–909, https://doi.org/10.1063/1.480617 (visited on 07/22/2022).

[81] K. H. Biswas, J. A. Jackman, J. H. Park, J. T. Groves, N.-J. Cho, *Langmuir* **2018**, *34*, Publisher: American Chemical Society, 1775–1782, https://doi.org/10.1021/acs.langmuir.7b03799.

[82] J. A. Jackman, M. C. Kim, V. P. Zhdanov, N.-J. Cho, *Physical Chemistry Chemical Physics* **2016**, *18*, Publisher: The Royal Society of Chemistry, 3065–3072, http://dx.doi.org/10.1039/C5CP06786C.

[83] J. A. Jackman, J.-H. Choi, V. P. Zhdanov, N.-J. Cho, *Langmuir* **2013**, *29*, Publisher: American Chemical Society, 11375–11384, https://doi.org/10.1021/la4017992.

[84] M. Sundh, S. Svedhem, D. S. Sutherland, *The Journal of Physical Chemistry B* **2011**, *115*, Publisher: American Chemical Society, 7838–7848, https://doi.org/10.1021/jp2025363.

[85] R. Tero, *Materials* **2012**, *5*, 2658–2680, http://www.mdpi.com/1996-1944/5/12/2658 (visited on 07/22/2022).

[86] G. A. Somorjai, Y. Li, *Proceedings of the National Academy of Sciences* **2011**, *108*, 917–924, http://www.pnas.org/cgi/doi/10.1073/pnas.1006669107 (visited on 06/01/2021).

[87] J. J. Velasco-Vélez, V. Pfeifer, M. Hävecker, R. Wang, A. Centeno, A. Zurutuza, G. Algara-Siller, E. Stotz, K. Skorupska, D. Teschner, P. Kube, P. Braeuninger-Weimer, S. Hofmann, R. Schlögl, A. Knop-Gericke, *Review of Scientific Instruments* **2016**, *87*, Publisher: American Institute of Physics, 053121, https://doi.org/10.1063/1.4951724 (visited on 02/15/2021).

[88] E. Bolli, S. Kaciulis, A. Mezzi, *Coatings* **2020**, *10*, DOI 10.3390/coatings10121182.

[89] M. Wang, L. Árnadóttir, Z. J. Xu, Z. Feng, *Nano-Micro Letters* **2019**, *11*, 47, https://doi.org/10.1007/s40820-019-0277-x.

[90] D. E. Rosenfeld, Z. Gengeliczki, B. J. Smith, T. D. P. Stack, M. D. Fayer, *Science* **2011**, *334*, 634–639, https://www.sciencemag.org/lookup/doi/10.1126/science.1211350 (visited on 01/15/2021).

[91] D. V. Talapin, M. Engel, P. V. Braun, *MRS Bulletin* **2020**, *45*, 799–806, https://www.cambridge.org/core/product/identifier/S0883769420002523/type/journal_article (visited on 11/09/2020).

[92] A. G. Rankin, J. Trébosc, F. Pourpoint, J.-P. Amoureux, O. Lafon, *Solid State Nuclear Magnetic Resonance* **2019**, *101*, 116–143, http://www.sciencedirect.com/science/article/pii/S092620401930030X.

[93] H. C. Hoffmann, M. Debowski, P. Müller, S. Paasch, I. Senkovska, S. Kaskel, E. Brunner, *Materials* **2012**, *5*, DOI 10.3390/ma5122537.

[94] O. Pecher, J. Carretero-González, K. J. Griffith, C. P. Grey, *Chemistry of Materials* **2017**, *29*, Publisher: American Chemical Society, 213–242, https://doi.org/10.1021/acs.chemmater.6b03183 (visited on 07/07/2020).

[95] C. Copéret, W.-C. Liao, C. P. Gordon, T.-C. Ong, *Journal of the American Chemical Society* **2017**, *139*, Publisher: American Chemical Society, 10588–10596, https://doi.org/10.1021/jacs.6b12981.

[96] M. Haake, A. Pines, J. A. Reimer, R. Seydoux, *Journal of the American Chemical Society* **1997**, *119*, 11711–11712, https://pubs.acs.org/doi/10.1021/ja9713587 (visited on 12/30/2020).

[97] G. Balasubramanian, I. Y. Chan, R. Kolesov, M. Al-Hmoud, J. Tisler, C. Shin, C. Kim, A. Wojcik, P. R. Hemmer, A. Krueger, T. Hanke, A. Leitenstorfer, R. Bratschitsch, F. Jelezko, J. Wrachtrup, *Nature* **2008**, *455*, Publisher: Springer Science and Business Media LLC, 648–651, https://doi.org/10.1038/nature07278.

[98] J. R. Maze, P. L. Stanwix, J. S. Hodges, S. Hong, J. M. Taylor, P. Cappellaro, L. Jiang, M. V. G. Dutt, E. Togan, A. S. Zibrov, A. Yacoby, R. L. Walsworth, M. D. Lukin, *Nature* **2008**, *455*, 644–647, https://doi.org/10.1038/nature07279.

[99] I. Lovchinsky, A. O. Sushkov, E. Urbach, N. P. de Leon, S. Choi, K. De Greve, R. Evans, R. Gertner, E. Bersin, C. Muller, L. McGuinness, F. Jelezko, R. L. Walsworth, H. Park, M. D. Lukin, *Science* **2016**, *351*, 836–841, https://www.sciencemag.org/lookup/doi/10.1126/science.aad8022 (visited on 12/16/2020).

[100] A. O. Sushkov, I. Lovchinsky, N. Chisholm, R. L. Walsworth, H. Park, M. D. Lukin, *Physical Review Letters* **2014**, *113*, 197601, https://link.aps.org/doi/10.1103/PhysRevLett.113.197601 (visited on 12/30/2020).

[101] I. Lovchinsky, J. D. Sanchez-Yamagishi, E. K. Urbach, S. Choi, S. Fang, T. I. Andersen, K. Watanabe, T. Taniguchi, A. Bylinskii, E. Kaxiras, P. Kim, H. Park, M. D. Lukin, *Science* **2017**, *355*, Publisher: American Association for the Advancement of Science Section: Report, 503–507, https://science-sciencemag-org.eaccess.ub.tum.de/content/355/6324/503 (visited on 04/09/2021).

[102] R. Zhao, P. Rupper, S. Gaan, *Coatings* **2017**, *7*, 133, http://www.mdpi.com/2079-6412/7/9/133 (visited on 11/05/2019).

[103] T. Staudacher, N. Raatz, S. Pezzagna, J. Meijer, F. Reinhard, C. A. Meriles, J. Wrachtrup, *Nature Communications* **2015**, *6*, 8527, http://www.nature.com/articles/ncomms9527 (visited on 11/29/2019).

[104] A. Laraoui, F. Dolde, C. Burk, F. Reinhard, J. Wrachtrup, C. A. Meriles, *Nature Communications* **2013**, *4*, 1651, http://www.nature.com/articles/ncomms2685 (visited on 03/18/2020).

[105] D. R. Glenn, D. B. Bucher, J. Lee, M. D. Lukin, H. Park, R. L. Walsworth, *Nature* **2018**, *555*, 351–354, http://www.nature.com/articles/nature25781 (visited on 03/18/2020).

[106] D. B. Bucher, D. R. Glenn, H. Park, M. D. Lukin, R. L. Walsworth, *Physical Review X* **2020**, *10*, Publisher: American Physical Society, 021053, https://link.aps.org/doi/10.1103/PhysRevX.10.021053 (visited on 08/02/2020).

[107] A. Henning, J. D. Bartl, A. Zeidler, S. Qian, O. Bienek, C.-M. Jiang, C. Paulus, B. Rieger, M. Stutzmann, I. D. Sharp, *Advanced Functional Materials* **2021**, *31*, 2101441, https://onlinelibrary.wiley.com/doi/10.1002/adfm.202101441 (visited on 08/19/2021).

[108] M. Gaborieau, R. Graf, S. Kahle, T. Pakula, H. W. Spiess, *Macromolecules* **2007**, *40*, Publisher: American Chemical Society, 6249–6256, https://doi.org/10.1021/ma0706531.

[109] L. Vugmeyster, D. Ostrovsky, *Progress in Nuclear Magnetic Resonance Spectroscopy* **2017**, *101*, 1–17, https://linkinghub.elsevier.com/retrieve/pii/S0079656516300632 (visited on 02/28/2021).

[110] D. Rugar, H. J. Mamin, M. H. Sherwood, M. Kim, C. T. Rettner, K. Ohno, D. D. Awschalom, *Nature Nanotechnology* **2015**, *10*, Number: 2 Publisher: Nature Publishing Group, 120–124, https://www.nature.com/articles/nnano.2014.288 (visited on 05/20/2021).

[111] C. Meltzer, H. Yu, W. Peukert, B. Braunschweig, *Physical Chemistry Chemical Physics* **2018**, *20*, 19382–19389, http://xlink.rsc.org/?DOI=C8CP02391C (visited on 01/28/2021).

[112] A. G. Koutsioubas, N. Spiliopoulos, D. L. Anastassopoulos, A. A. Vradis, G. D. Priftis, *Surface and Interface Analysis* **2009**, *41*, 897–903, http://doi.wiley.com/10.1002/sia.3116 (visited on 01/07/2021).

[113] H. Ishiwata, H. C. Watanabe, S. Hanashima, T. Iwasaki, M. Hatano, *Advanced Quantum Technologies* **2021**, 2000106, https://onlinelibrary.wiley.com/doi/10.1002/qute.202000106 (visited on 03/14/2021).

[114] A. A. Wood, E. Lilette, Y. Y. Fein, N. Tomek, L. P. McGuinness, L. C. L. Hollenberg, R. E. Scholten, A. M. Martin, *Science Advances* **2018**, *4*, eaar7691, http://advances.sciencemag.org/content/4/5/eaar7691.abstract.

[115] C. Osterkamp, M. Mangold, J. Lang, P. Balasubramanian, T. Teraji, B. Naydenov, F. Jelezko, *Scientific Reports* **2019**, *9*, Number: 1 Publisher: Nature Publishing Group, 5786, https://www.nature.com/articles/s41598-019-42314-7 (visited on 01/05/2021).

[116] S. Steinert, F. Ziem, L. T. Hall, A. Zappe, M. Schweikert, N. Götz, A. Aird, G. Balasubramanian, L. Hollenberg, J. Wrachtrup, *Nature Communications* **2013**, *4*, Number: 1 Publisher: Nature Publishing Group, 1607, https://www.nature.com/articles/ncomms2588 (visited on 07/27/2020).

[117] C. L. Degen, F. Reinhard, P. Cappellaro, *Rev. Mod. Phys.* **2017**, *89*, Publisher: American Physical Society, 035002, https://link.aps.org/doi/10.1103/RevModPhys.89.035002.

[118] I. Schwartz, J. Rosskopf, S. Schmitt, B. Tratzmiller, Q. Chen, L. P. McGuinness, F. Jelezko, M. B. Plenio, *Scientific Reports* **2019**, *9*, 6938, http://www.nature.com/articles/s41598-019-43404-2 (visited on 11/05/2019).

[119] S. Oviedo-Casado, A. Rotem, R. Nigmatullin, J. Prior, A. Retzker, *Scientific Reports* **2020**, *10*, 19691, http://www.nature.com/articles/s41598-020-76745-4 (visited on 04/09/2022).

[120] R. A. Shugayev, S. E. Crawford, J. P. Baltrus, N. A. Diemler, J. E. Ellis, K.-J. Kim, P. C. Cvetic, *Chemistry of Materials* **2021**, Publisher: American Chemical Society, DOI 10.1021/acs.chemmater.1c01386, https://doi.org/10.1021/acs.chemmater.1c01386 (visited on 08/16/2021).

[121] B. Chen, S. Xiang, G. Qian, *Accounts of Chemical Research* **2010**, *43*, Publisher: American Chemical Society, 1115–1124, https://doi.org/10.1021/ar100023y (visited on 02/28/2022).

[122] Y. G. Chung, J. Camp, M. Haranczyk, B. J. Sikora, W. Bury, V. Krungleviciute, T. Yildirim, O. K. Farha, D. S. Sholl, R. Q. Snurr, *Chemistry of Materials* **2014**, *26*, Publisher: American Chemical Society, 6185–6192, https://doi.org/10.1021/cm502594j.

[123] J. Winarta, B. Shan, S. M. Mcintyre, L. Ye, C. Wang, J. Liu, B. Mu, *Crystal Growth & Design* **2020**, *20*, Publisher: American Chemical Society, 1347–1362, https://doi.org/10.1021/acs.cgd.9b00955.

[124] A. L. Semrau, S. Wannapaiboon, S. P. Pujari, P. Vervoorts, B. Albada, H. Zuilhof, R. A. Fischer, *Crystal Growth & Design* **2019**, *19*, 1738–1747, https://pubs.acs.org/doi/10.1021/acs.cgd.8b01719 (visited on 03/16/2020).

[125] A. L. Semrau, R. A. Fischer, *Chemistry – A European Journal* **2021**, *27*, Publisher: John Wiley & Sons, Ltd, 8509–8516, https://doi.org/10.1002/chem.202005416 (visited on 09/03/2021).

[126] S. Wannapaiboon, K. Sumida, K. Dilchert, M. Tu, S. Kitagawa, S. Furukawa, R. A. Fischer, *Journal of Materials Chemistry A* **2017**, *5*, 13665–13673, http://xlink.rsc.org/?DOI=C7TA02848B (visited on 10/30/2019).

[127] K. S. Liu, A. Henning, M. W. Heindl, R. D. Allert, J. D. Bartl, I. D. Sharp, R. Rizzato, D. B. Bucher, *Proceedings of the National Academy of Sciences* **2022**, *119*, e2111607119, http://www.pnas.org/lookup/doi/10.1073/pnas.2111607119 (visited on 01/27/2022).

[128] E. Janitz, K. Herb, L. A. Völker, W. S. Huxter, C. L. Degen, J. M. Abendroth, Diamond surface engineering for molecular sensing with nitrogen-vacancy centers, **2022**, https://arxiv.org/abs/2207.07509.

[129] E. H. Otal, M. L. Kim, M. E. Calvo, L. Karvonen, I. O. Fabregas, C. A. Sierra, J. P. Hinestroza, *Chemical Communications* **2016**, *52*, Publisher: The Royal Society of Chemistry, 6665–6668, http://dx.doi.org/10.1039/C6CC02319C.

[130] G. E. Cmarik, M. Kim, S. M. Cohen, K. S. Walton, *Langmuir* **2012**, *28*, 15606–15613, https://pubs.acs.org/doi/10.1021/la3035352 (visited on 07/08/2022).

[131] Y. Jiao, Y. Liu, G. Zhu, J. T. Hungerford, S. Bhattacharyya, R. P. Lively, D. S. Sholl, K. S. Walton, *The Journal of Physical Chemistry C* **2017**, *121*, 23471–23479, https://pubs.acs.org/doi/10.1021/acs.jpcc.7b07772 (visited on 07/08/2022).

[132] J. H. Cavka, S. Jakobsen, U. Olsbye, N. Guillou, C. Lamberti, S. Bordiga, K. P. Lillerud, *Journal of the American Chemical Society* **2008**, *130*, 13850–13851, https://pubs.acs.org/doi/10.1021/ja8057953 (visited on 07/08/2022).

[133] C. Wang, D. Liu, W. Lin, *Journal of the American Chemical Society* **2013**, *135*, Publisher: American Chemical Society, 13222–13234, https://doi.org/10.1021/ja308229p.

[134] R. Rizzato, F. Bruckmaier, K. Liu, S. Glaser, D. Bucher, *Physical Review Applied* **2022**, *17*, Publisher: American Physical Society, 024067, https://link.aps.org/doi/10.1103/PhysRevApplied.17.024067.

[135] J. Lombard, *Biology direct* **2014**, *9*, Publisher: BioMed Central, 32–32, https://pubmed.ncbi.nlm.nih.gov/25522740.

[136] Y. Hosaka, K. Yasuda, R. Okamoto, S. Komura, *Physical Review E: Statistical Physics Plasmas Fluids and Related Interdisciplinary Topics* **2017**, *95*, Number of pages: 10 Publisher: American Physical Society, 052407, https://link.aps.org/doi/10.1103/PhysRevE.95.052407.

[137] M. Skocaj, B. Bakrac, I. Krizaj, P. Macek, G. Anderluh, K. Sepcic, *Current Medicinal Chemistry* **2013**, *20*, 491–501, http://www.eurekaselect.com/article/48649.

[138] E. Sezgin, I. Levental, M. Grzybek, G. Schwarzmann, V. Mueller, A. Honigmann, V. N. Belov, C. Eggeling, Ü. Coskun, K. Simons, P. Schwille, *Biochimica et Biophysica Acta (BBA) - Biomembranes* **2012**, *1818*, 1777–1784, https://www.sciencedirect.com/science/article/pii/S0005273612000879.

[139] Z. Leonenko, E. Finot, H. Ma, T. S. Dahms, D. Cramb, *Biophysical Journal* **2004**, *86*, 3783–3793, https://linkinghub.elsevier.com/retrieve/pii/S0006349504744185 (visited on 06/07/2022).

[140] J. A. Jackman, N.-J. Cho, *Langmuir* **2020**, *36*, Publisher: American Chemical Society, 1387–1400, https://doi.org/10.1021/acs.langmuir.9b03706.

[141] F. Shagieva, A. Zappe, D. Cohen, A. Denisenko, A. Retzker, J. Wrachtrup, Lateral diffusion of phospholipids in artificial cell membranes measured by single shallow NV centers, **2021**, https://arxiv.org/abs/2105.07712.

[142] H. A. Scheidt, D. Huster, K. Gawrisch, *Biophysical Journal* **2005**, *89*, 2504–2512, https://linkinghub.elsevier.com/retrieve/pii/S0006349505728915 (visited on 06/09/2022).

[143] J. Hjort Ipsen, G. Karlström, O. Mourtisen, H. Wennerström, M. Zuckermann, *Biochimica et Biophysica Acta (BBA) - Biomembranes* **1987**, *905*, 162–172, https://www.sciencedirect.com/science/article/pii/0005273687900204.

[144] S. Leekumjorn, A. K. Sum, *Biochimica et Biophysica Acta (BBA) - Biomembranes* **2007**, *1768*, 354–365, https://linkinghub.elsevier.com/retrieve/pii/S0005273606004196 (visited on 06/07/2022).

[145] J. F. Nagle, S. Tristram-Nagle, *Biochimica et Biophysica Acta (BBA) - Reviews on Biomembranes* **2000**, *1469*, 159–195, https://www.sciencedirect.com/science/article/pii/S0304415700000162.

[146] H. I. Petrache, S. W. Dodd, M. F. Brown, *Biophysical journal* **2000**, *79*, 3172–3192, https://pubmed.ncbi.nlm.nih.gov/11106622.

[147] N. Staudenmaier, A. Vijayakumar-Sreeja, S. Oviedo-Casado, G. Genov, D. Cohen, D. Dulog, T. Unden, N. Striegler, A. Marshall, J. Scheuer, C. Findler, J. Lang, I. Schwartz, P. Neumann, A. Retzker, F. Jelezko, *arXiv:2203.11161 [quant-ph]* **2022**, http://arxiv.org/abs/2203.11161 (visited on 04/11/2022).

[148] D. Cohen, R. Nigmatullin, O. Kenneth, F. Jelezko, M. Khodas, A. Retzker, *Scientific Reports* **2020**, *10*, 5298, http://www.nature.com/articles/s41598-020-61095-y (visited on 04/19/2022).

[149] C. Scomparin, S. Lecuyer, M. Ferreira, T. Charitat, B. Tinland, *The European Physical Journal E* **2009**, *28*, 211–220, http://link.springer.com/10.1140/epje/i2008-10407-3 (visited on 04/05/2022).

[150] P. Jönsson, M. P. Jonsson, J. O. Tegenfeldt, F. Höök, *Biophysical Journal* **2008**, *95*, 5334–5348, https://www.sciencedirect.com/science/article/pii/S0006349508789586.

[151] P. PYYKKÖ, *Molecular Physics* **2001**, *99*, Publisher: Taylor & Francis _eprint: https://doi.org/10.1080/002 1617–1629, https://doi.org/10.1080/00268970110069010.

[152] H. McConnell, A. Radhakrishnan, *Proceedings of the National Academy of Sciences* **2006**, *103*, 1184–1189, https://pnas.org/doi/full/10.1073/pnas.0510514103 (visited on 08/24/2022).

[153] H. Singh, J. Emberley, M. R. Morrow, *European Biophysics Journal* **2008**, *37*, 783–792, http://link.springer.com/10.1007/s00249-008-0270-7 (visited on 08/24/2022).

[154] B. B. Bonev, M. R. Morrow, **1998**, *76*, 8.

[155] G. Wu, V. Terskikh, A. Wong, *Magnetic Resonance in Chemistry* **2021**, *59*, 162–171, https://onlinelibrary.wiley.com/doi/10.1002/mrc.5097 (visited on 08/24/2022).

[156] J. Griffiths, *Analytical Chemistry* **2008**, *80*, 7194–7197, https://pubs.acs.org/doi/10.1021/ac801528u (visited on 11/19/2021).

[157] K. Li, J. Liu, C. R. M. Grovenor, K. L. Moore, **2020**, 20.

[158] J. Qian, A. Baskin, Z. Liu, D. Prendergast, E. J. Crumlin, *The Journal of Chemical Physics* **2020**, *153*, 044709, http://aip.scitation.org/doi/10.1063/5.0006242 (visited on 11/19/2021).

[159] S. Oswald in *Encyclopedia of Analytical Chemistry*, (Ed.: R. A. Meyers), John Wiley & Sons, Ltd, Chichester, UK, **2013**, a2517.pub2, https://onlinelibrary.wiley.com/doi/10.1002/9780470027318.a2517.pub2 (visited on 11/23/2021).

[160] H.-F. Wang, L. Velarde, W. Gan, L. Fu, *Annual Review of Physical Chemistry* **2015**, *66*, 189–216, https://www.annualreviews.org/doi/10.1146/annurev-physchem-040214-121322 (visited on 11/19/2021).

[161] C. Cushman, C. Dahlquist, P. Dietrich, S. Bahr, A. Thissen, O. Schaff, J. Banerjee, N. Smith, M. Linford, *Vacuum Technology & Coating* **2017**.

[162] D. Oing, M. Geller, L. Stahl, J. Kerski, A. Lorke, N. Wöhrl, *Scientific Reports* **2020**, *10*, 12533, http://www.nature.com/articles/s41598-020-69240-3 (visited on 11/23/2021).

[163] R. Mills, *The Journal of Physical Chemistry* **1973**, *77*, Publisher: American Chemical Society, 685–688, https://doi.org/10.1021/j100624a025.